Title
Force Measurement of Nanoscale Optical Nearfield Distribution

Author
Huang, Fei

Publication Date
2016

Peer reviewed|Thesis/dissertation

UNIVERSITY OF CALIFORNIA,

IRVINE

Force Measurement of Nanoscale Optical Nearfield Distribution

DISSERTATION

submitted in partial satisfaction of the requirements

for the degree of

DOCTOR OF PHILOSOPHY

in Electrical and Computer Engineering

by

Fei Huang

Dissertation Committee:
Professor H. Kumar Wickramasinghe, Chair
Associate Professor Eric Potma
Associate Professor Ozdal Boyraz

2016

DEDICATION

To

my family, teachers and friends

in recognition of their worth

TABLE OF CONTENTS

LIST OF FIGURES

ACKNOWLEDGMENTS

I would like to express the deepest appreciation to my committee chair, Professor H. Kumar Wickramasinghe, who at the very top level researcher in the world. I do really appreciate my advisor took me as his student regardless that I am from a totally different background. I do really appreciate these days that my advisor work with me until the late night. I would like to thank my advisor for the tremendous support for me. Without his guidance and persistent help this dissertation would not have been possible.

I would like to thank my committee members, Professor Eric Potma and Prof. Ozdal Boyraz, who serve in my PhD committee. Also, I would like to thank Prof. G. P. Li and Prof. Franco De Flaviis for their support during the candidacy examination.

I would like to thank my team members: Dr. Indrajith Rajapaksa, Dr. Ananth Tamma, Dr. Ganeshkumar Varadarajalu, Dr. Jonathan Burdett, Dr. Jinwei Zeng, Yinglei Tao, Elaheh Shekaramiz, and Zahra Mardy, Mohsen Rajaei, Mohammad Ali Almajhadi for their support. I would like to thank Prof. Filippo Capolino, Prof. Ara Apkarian for the helpful discussion. In addition, I would like to thank Dr. Dmitry A. Fishman, Dr. Junghoon Jahng, Dr. Jordan Brocious, Dr. Xiaowei Li, Dr. Sung Park, Dr. Derek Nowak, William Morrison, Dr. Nicholas Sharac, Caner Guclu, Dr. Jie Chen, and Dr. Feng Jiang for the discussion. I would also like to thank the staff from the UC Irvine Materials Research Institute (IMRI) for their support for the materials characterization and fabrication. I would like to thank the staff at the purchasing department for their support. Also I would like to thank the CaSTL, an NSF Center for Chemical Innovation for funding this work.

I would like to give enormous thank to my parents, my kids, my brother, especially my husband Yulin Chen without your endless support, I would not have this innovation work done.

CURRICULUM VITAE

Fei Huang

1998-2002	B.S. in Electrical Engineering, Nankai University, China
2002-2005	M.S.in Electrical Engineering**,** Institute of Acoustics, Chinese Academy of Sciences, China
2005- 2006	Research engineer, Ubiquitous Platform Laboratory Hitachi (China) Research & Development Corporation
2009-2016	Ph.D. in Electrical Engineering and Computer Science, University of California, Irvine

FIELD OF STUDY

High spatial resolution force measurement of nanoscale optical nearfield distribution

PUBLICATIONS

[1] **Huang, F.**, Tamma, V. A. & Wickramasinghe, H. K. Measurement of Laterally Induced Optical Forces at the Nanoscale, arXiv:1605.03163

[2] Tamma, V. A., **Huang, F.**, Nowak, D. & Wickramasinghe, H. K. Stimulated Raman spectroscopy and nanoscopy of molecules using near field photon induced forces without resonant electronic enhancement gain, *Appl. Phys. Lett.* **108**, 233107 (2016).

[3] **Huang, F.**, Tamma, V. A., Mardy, Z., Burdett, J. & Wickramasinghe, H. K. Imaging Nanoscale Electromagnetic Near-Field Distributions Using Optical Forces, *Sci. Rep.* **5**, 10610 (2015)

[4] Jahng, J., Brocious, J., Fishman, D. A., **Huang, F.**, Li, X., Tamma, V. A., Wickramasinghe, H. K. & Potma, E. O. Gradient and scattering forces in photoinduced force microscopy. *Phys. Rev. B*, **90**(15), 155417(2014).

[5] Jahng, J., Brocious, J., Fishman, D. A., Yampolsky, S., Nowak, D., **Huang, F.**, Apkarian, V. A., Wickramasinghe, H. K. & Potma, E. O. Ultrafast pump-probe force microscopy with nanoscale resolution. *Appl. Phys. Lett.*, **106**(8), 083113. (2015).

[6] **Huang, F.**, Zeng, X., Chen, J., Pan, L., Design and implementation of secure software update for STB system based on DVB data broadcasting. *Video Engineering*. z1, 109-112. (2005). (in Chinese)

[7] Pan, L., **Huang, F.**, Zeng, X. W., Chen, J., Wu, B. Method for upgrading software of digital terminal system in DVB system. *CN200510051444.9*

[8] Fujii, Y., **Huang, F.** Television program receiving equipment and method for receiving and broadcasting television program. *CN200610100157.*

ABSTRACT OF THE DISSERTATION

Force Measurement of Nanoscale Optical Nearfield Distribution

By

Fei Huang

Doctor of Philosophy in Electrical Engineering and Computer Science

University of California, Irvine, 2016

Professor Prof. H. Kumar Wickramasinghe, Chair

The objective of this dissertation is to develop a novel method to measure nanoscale optical field distribution using optical induce forces. We demonstrate the application of Atomic Force Microscopy (AFM) for detecting nearfield optical induced force including axial force and lateral force. We develop a method that detects laterally and axially induced optical forces by different flexure and torsional modes which can enable simultaneous multi-channel detection of nanoscale optical forces along different orientations.

We have mapped optical near-fields with nanometer resolution, limited only by the AFM probe geometry. By detecting the optical force between a gold coated AFM probe and its image dipole on a glass substrate, we profile the electric field distributions in axial force of tightly focused laser beams with different polarizations. The experimentally recorded focal force maps agree well with theoretical predictions based on the dipole-dipole interaction model. We experimentally estimate the aspect ratio of the apex of gold coated AFM probe using only optical forces. We also show that the optical force between a sharp

gold coated AFM probe and a spherical gold nanoparticle of radius 15 nm, is indicative of the electric field distribution between the two interacting particles.

We also show a controlled method to fabricate tips that have high enhancement factor, which is desirable for the linear and non-linear response of the molecule response.

Photon Induced Force Microscopy (PIFM) allows for background free, thermal noise limited mechanical imaging of optical phenomenon over wide range of wavelengths from visible to RF with detection sensitivity limited only by AFM performance. The use of an AFM cantilever as a multi-channel detector paves the way for simultaneous PiFM detection of molecular responses with different incident field polarizations.

Chapter 1 Introduction

Microscope has been used for a long time as a tools for all science research. When research topics focus on micrometer range, optical microscope have been used enormously and have enough resolution to get information of object since optical microscope can reach the micrometer resolution. Optical microscope has been wildly used in many fields include biology, chemistry, physics, material science etc. Different types of optical microscope have been implemented for different applications. Phase contrast has been wildly used for transparent sample, especially used in biology to look at cell, dark field microscope has been used in gemological and biology. One more commonly used type of optical microscope is the fluorescence microscope, which has special requirement for the sample, can only image the fluorophore. Confocal microscope is used to enhance the resolution optical microscope, which using pinhole to confine the excitation laser and the detection laser. Confocal also image the fluorophore, since confocal microscope has pin hole, it record 3d image without scanning probe microscope. With the far field detection, nowadays many method has been invented to have the super-resolution solution which gives high resolution using deferent excitation method or detection method such as photoactivated localization microscopy (PALM)[1] or stimulated emission depletion (STED) [2], but these methods not only need special fluorescent molecules, but also have an very complicate optical setup and signal processing of the detection, which give the limitation to the application of the methods.

As the development of science and technology, the requirement of image resolution has been increased. Scanning probe microscopy, transmission electron microscopy and scanning electron microscopy have the resolution down to nanometer range. These techniques have disadvantages compared to regular optical microscope. For scanning probe microscopy, topography of the surface has the effect of the tip convolution. For transmission electron microscopy, has the highest resolution sub nanometer but needs high vacuum and sample need to be thin enough and mount in a conductive substrate. Scanning electron microscopy also needs sample to be conductive to direct the electron and also need to be in the vacuum. Depend on the research requirement, we have to choose proper measurement method.

Microcopies are aim to get the morphology of the sample, we do want to develop a novel method to measure no only information of the morphology but also optical properties of the sample.

1.1 Atomic Force Microscopy

Atomic Force Microscopy (AFM), scanning probe microscopy, enables high resolution imaging of the physical[3], chemical [4], magnetic [5], and electrostatic [6] properties of materials at the nanoscale, the resolution of AFM is the radius of the AFM cantilever tip.

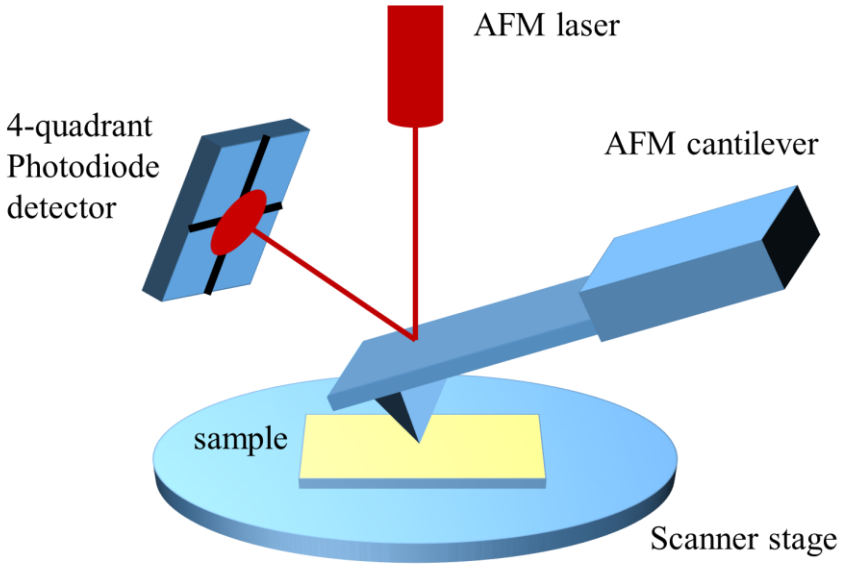

Figure 1 Block diagram of AFM with beam deflection detection

As shown in Figure 1, AFM has mainly 4 components, cantilever probe (force detector), xyz piezo stage (high resolution motion control of cantilever or stage), electronic control system and a cantilever motion detector. The surface information is obtained from high resolution control the gap of the cantilever probe and surface by detecting and controlling the interaction force between cantilever probe and surface. There are different motion detector of AFM, AFM cantilever use optical detector with laser beam deflect of the back of the cantilever, tuning fork use the electrical current detector. Also there are different modes that AFM can work with contact mode and tapping mode. To measure different surface property, there are KPFM, MFM, thermal AFM, force spectroscopy, etc.

As the development of science and technology, AFM has new applications instead of measuring the morphology of the surface. AFM has been combined with optics. Aperture-less nearfield microscopy has use the AFM cantilever probe to transform the nearfield optical signal to far field signal. Near-field Scanning Optical Microscopy (NSOM) has been used to

study light-matter interaction beyond the diffraction limit with important applications in many areas of nano-optics, materials science, chemistry and biology[7]. Aperture-less or scattering NSOM (*s*-NSOM)[8]techniques have been used to map the nanoscale electric [9–12] and magnetic[13–15] field distributions. Scattering NSOM has also been used to map the plasmonic modes in nanostructures and nano-antennas[16–19]. NSOM techniques involve the sampling of evanescent electromagnetic fields close to the sample surface due to light scattering by structured metallic probes brought close to the surface of the sample. Scattered evanescent fields are converted into propagating modes that are detected in the far-field. While many techniques have been proposed for reducing background noise, fundamentally, since NSOM techniques has the near field excitation but far field detection, NSOM techniques are limited by the sensitivity of the schemes used for far-field light collection and detection.

A setup similar to NSOM can measure the force signal which indicates nanoscale mid-infrared spectra by measuring mechanical forces generated by the molecule absorption expansion[20,21]. This technique uses contact-mode AFM to measure the sample expansion from the mid-IR laser absorption at the contact resonance of the cantilever that have the resolution of 20nm.

1.2 Photoinduced force detection

AFM based Photo Induced Force Microscopy (PIFM) scheme was introduced to detect and image molecular resonances at nanometer level[22,23] and produce nanoscale optical force maps[24,25]. In contrast, PIFM can detect and image nanoscale light-matter interactions without the need for any far-field light collection. PIFM detection is

fundamentally wavelength independent and can be applied to measure both linear[22,26,27]and non-linear responses [23,28,29]of materials. It extends the domain of AFM to include optically induced forces with applications in nano/atomic scale optical imaging and microscopy. In this paper, we use the tapping mode AFM working under ambient conditions to investigate and map the nanoscale electromagnetic field distributions with resolution limited only by the AFM probe geometry.

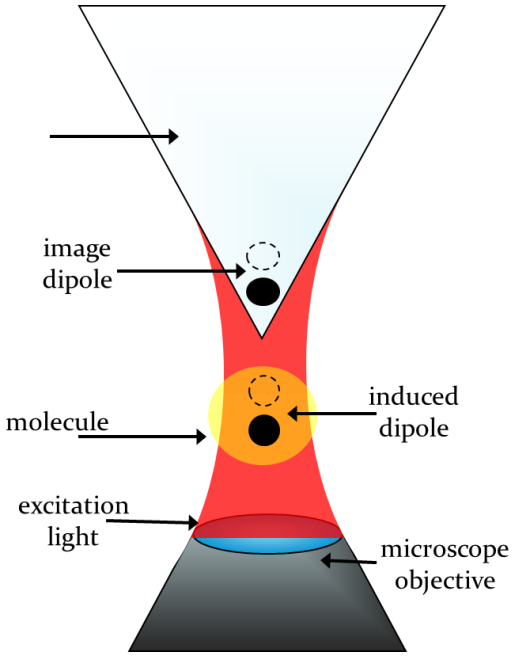

Figure 2 Diagram of optical induced dipole force

The optical induced force is the dipole dipole interaction force between an optical induced dipole on the metal coated tip and an optical induced dipole in the sample as shown in Figure 2. AFM cantilever is acting both as control of the tip sample distance and force detector. Measuring the nearfield optical induced force by the light matter interaction has the advantage of low background noise since no photon detector is needed.

Absorption of molecule has been measured[22,29] excited by tightly focus beam using transmission mode microscope, which has shown the optical induced force proportional to the optical absorption of molecule.

Side illumination has been used for the mid-IR by detecting the optical force between a gold coated AFM probe illuminated[27]. 7 nm spatial Resolution has been shown with different bond response to the IR light. This method is a very powerful characterization of IR sensitive material and will enable the fine control of the fabrication process down to nano scale.

Raman signal also have been measured[23,28] excited on resonance of the electronic state or without resonant electronic enhancement gain. The experiments have shown the high spatial resolution down to several nano meter far below the optical diffraction limit.

Propagating surface plasmon mode has been measured using the photoinduced force[30]. Total internal reflection illumination is used to generate propagating surface plasmon mode. Optical induced force acting on the tip by the electric component of the evanescent surface plasmon mode has been measured.

We have measured the optical induced force between a tightly focused laser beam and its image induced on a clean glass substrate, we are able to map the focal electric field distributions within the focal region. The experimentally obtained focal force distribution is in agreement with theoretical predictions from a simple dipole-dipole interaction model. Using only optical forces and by fitting to a dipole-dipole model, we experimentally estimate the aspect ratio of the apex of a gold coated AFM probe (in terms of the ratio of polarizabilities of the tip apex) modeled as a prolate spheroid, In addition, we map the

interaction forces between a gold sphere of radius 15 nm and a gold coated AFM probe illuminated by an incident focal field. The measured force distributions are in excellent agreement with numerical calculations validating our experimental results. The experimental results are found to be background free, limited only by the thermal noise and AFM performance. Optical forces due to both electric and magnetic dipole-dipole interactions can be measured using this technique.

Chapter 2 Axial optical force detection

To measure the optical induced force, cantilever based AFM is used as the force detector. With optical excitation, the total force experienced by the AFM probe tip can be written as $\vec{F}_{tot} = \vec{F}_{int} + \langle \vec{F}_{opt} \rangle$ $\vec{F}_{tot} = \vec{F}_{int} + \vec{F}_{opt}$, where, $\vec{F}_{int}$ $\vec{F}_{int}$ is the total tip-sample interaction forces consisting of all van der Waals forces, meniscus forces, chemical and Casimir forces, and $\langle \vec{F}_{opt} \rangle$ $\langle \vec{F}_{opt} \rangle$ is the time-averaged optical force on the AFM probe tip due to its interaction with the incident field and particle dipole. $\langle \vec{F}_{opt} \rangle$ is a vector has x,y,z three component. In this chapter, we discuss the detection of axial (z) component of the optical induced force which along the tip axis.

2.1 Eigen- modes of AFM

To control the tip sample distance and at the same time detect the optical induced force, multi resonance frequency property of the AFM cantilever is used. The mechanical resonance of AFM cantilever is acting as a resonance system to enhance the optical induced force signal. Locating the optical signal at the mechanical resonance gives enhancement of the signal which in term higher the system detection sensitivity.

As many literature have shown study of the flexure mode of the tapping mode AFM[31], there are several eigen-modes of the cantilever resonance[32]. The eigen-mode frequency can be written as

$$f_n = \frac{(k_n L)^2}{{c_c}^2}$$

where $c_c = L\sqrt{2\pi}^4\sqrt{\frac{\rho A}{EI}}$, E is the modulus of elasticity, ρ is the mass density, A=a*b is the cross section, and I is the area moment of inertia.

COMSOL solid mechanics simulation of Appnano Forta tips has been done to explore the mechanical properties. The Comsol model and mesh is shown in Figure 3.

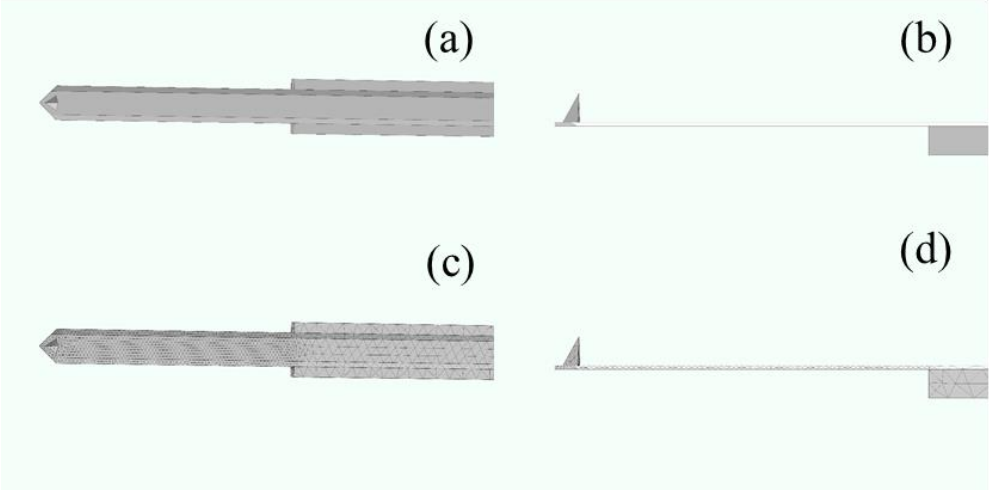

Figure 3 Comsol simulation model geometry for cantilever (a) front view (b)side view(c)mesh of the cantilever front view(d) mesh of the cantilever side view

We use the young's modulus 139 GPa for the isotropic silicon obtained from the vendor in the COMSOL simulation. The spec of the cantilever is that length is around 225um, width is 27um, thickness around 2.7 um. We use SEM measurement of the cantilever as the simulation geometry parameter.

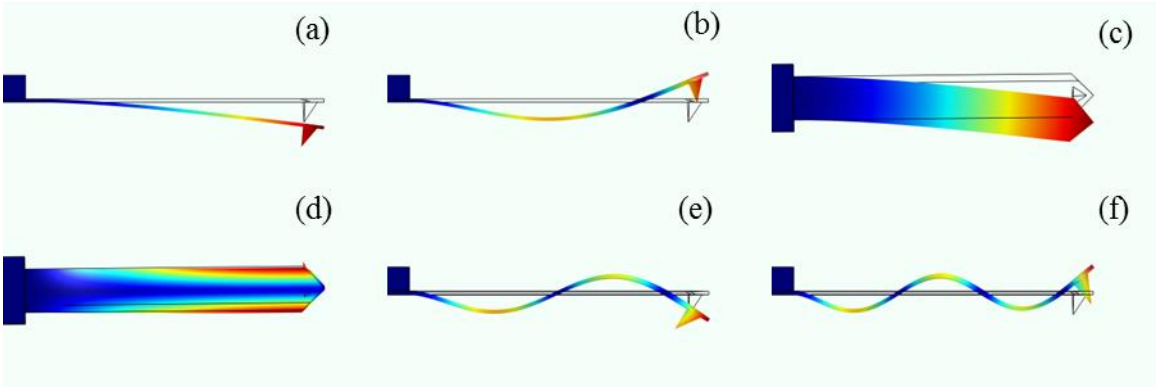

Figure 4 Simulation of eigen-mode of AFM cantilever using COMSOL Multiphysics (a) first flexural mode (b) second flexural mode (c) first lateral mode (d)) first torsional mode (e) third flexural mode (f) forth flexural mode

As shown in Figure 4, flexure modes can detect the axial force while torsional modes can detect lateral force.

To eliminate other long range force effects, we use the side band coupling scheme.

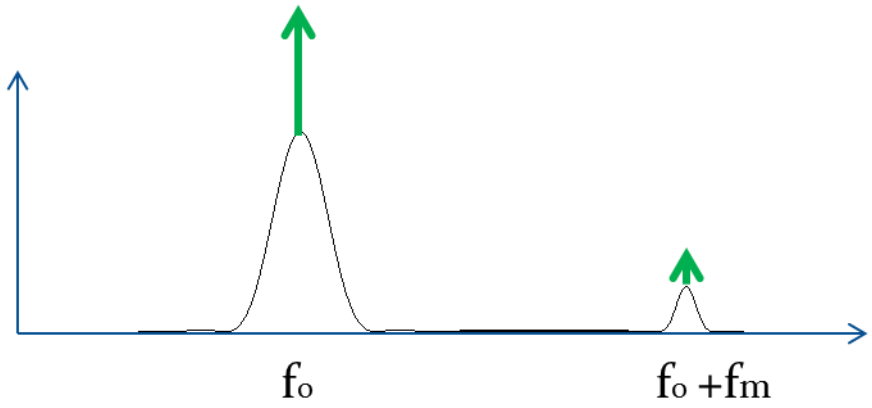

Figure 5 Side band modulation scheme

As shown in Figure 5, we modulate the laser at f_m which $f_m = f_1 - f_0$. This attractive gradient optical force modulates the AFM cantilever which vibrates at its first mechanical resonance

frequency f_0. This modulation will generate sidebands at f_0+f_m and f_0-f_m. We locate the sideband f_0+f_m on top of the second mechanical resonance frequency (f_1) of the AFM cantilever thereby utilizing the high Q of the second resonance of the AFM cantilever to enhance optical force signal.

2.2 Photo-induced force

As described in chapter1, the optical induced force is the dipole dipole interaction force between an optical induced dipole on the metal coated tip and an optical induced dipole in the sample. We can model the sample under measurement, as a sub-wavelength magneto-dielectric nanoparticle, which is a prolate spheroid with electric dipole moments $\vec{P}_p$ and magnetic dipole moments $\vec{M}_p$. We also model the end of the AFM tip as a sub-wavelength magneto-dielectric nanoparticle, which is a prolate spheroid with electric dipole moments $\vec{P}_t$ and magnetic dipole moments $\vec{M}_t$. We assume electromagnetic fields incident along the z direction are tightly focused at the interface between the background medium (isotropic relative permittivity ε_b and permeability μ_b) and the substrate (with isotropic relative permittivity ε_s and permeability μ_s, as shown schematically in Figure 6 (a).

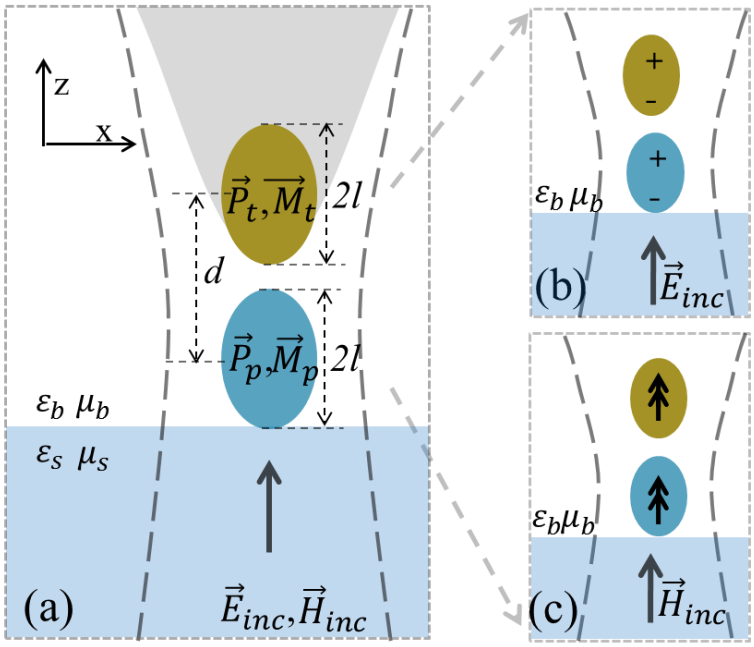

Figure 6 (a) Schematic of the tip-sample interaction under illumination by tightly focused laser beam (b) electric dipole-dipole interactions (c) magnetic dipole-dipole interactions

$\langle \vec{F}_{opt} \rangle$ $\langle \vec{F}_{opt} \rangle$ is the time-averaged optical force on the AFM probe tip due to its interaction with the incident field and particle dipole. $\langle \vec{F}_{opt} \rangle$ due to the presence of both electric and magnetic dipoles, $\langle \vec{F}_{opt} \rangle$ can be written as the sum, $\langle \vec{F}_{opt} \rangle = \langle \vec{F}_e \rangle + \langle \vec{F}_m \rangle + \langle \vec{F}_{e-m} \rangle$,where, $\langle \vec{F}_e \rangle = \frac{1}{2} \Re\{\vec{P}_t (\nabla \otimes \vec{E}_{t,loc})\}$ $\langle \vec{F}_e \rangle = \frac{1}{2} \Re\{\vec{P}_t (\nabla \cdot \vec{E}_{t,loc})\}$ is the time-averaged force experienced due to the electric dipole with assumption of spatially non-varying moment $\vec{P}_t$ $\vec{P}_t$, $\langle \vec{F}_m \rangle = \frac{1}{2} \Re\{\vec{M}_t (\nabla \cdot \vec{B}_{t,loc},)\}$ is the time-averaged force experienced due magnetic dipole with assumption of spatially non-varying moment $\vec{M}_t$ $\vec{M}_t$, $\langle \vec{F}_{e-m} \rangle = -\frac{1}{2} \Re\left\{ \frac{2k^4}{3} \sqrt{\frac{\mu_b}{\varepsilon_b}} (\vec{P}_t \times \vec{M}_t) \right\}$ $\langle \vec{F}_{e-m} \rangle = -\frac{1}{2} \Re\left\{ \frac{2k^4}{3} \sqrt{\frac{\mu_b}{\varepsilon_b}} (\vec{P}_t \times \vec{M}_t) \right\}$ is the interaction force due to coupling between the electric

and magnetic dipoles and $\boldsymbol{k}$ is the propagation constant of the incident wave. Here, $\vec{E}_{t,loc}$ $\vec{E}_{t,loc}$ and $\vec{B}_{t,loc}$ $\vec{B}_{t,loc}$ are the local electric and magnetic fields experienced by the AFM probe tip respectively and are given by the sum of the incident field and the fields scattered by the particle and the substrate.

Proper choice of $\vec{P}_t$ $\vec{P}_t$ and $\vec{M}_t$ $\vec{M}_t$ could allow for the detection of optical electric and/or magnetic fields using forces.

Electrical field distribution was first chosen to be measured, so no optical magnetic response at optical frequency sample is used, the magnetic dipole force is neglected. Metal coated tip supporting large values of $\vec{P}_t$ $\vec{P}_t$ is used to measure the electric dipole-dipole interaction forces schematically shown in Figure 6(b) The gold coated AFM probe is modeled as an ellipsoidal dielectric nanoparticle. The total time average electric force is

$$\left\langle \vec{F}_e \right\rangle = \frac{1}{2}\Re\left\{\vec{P}_t\left(\nabla \otimes \vec{E}_{t,loc}\right)^*\right\} \tag{2-1}$$

where, $\vec{E}_{t,loc}$ is the total electric field experienced by the gold coated AFM probe and is given by the sum of the incident field and the fields scattered by the particle dipole. Equation (2-1) can also be written as

$$\left\langle \vec{F}_e \right\rangle = \frac{1}{4}\alpha'\nabla\left|\vec{E}_{t,loc}\right|^2 + \frac{k}{2n}\alpha''\Re\left(\vec{E}_{t,loc}\times\vec{B}^*_{t,loc}\right) + \frac{1}{2}\alpha''\Im\left(\left(\vec{E}^*_{t,loc}\bullet\nabla\right)\vec{E}_{t,loc}\right) \tag{2-2}$$

where, the electric polarizability of the dielectric nanoparticle $\alpha = \alpha' + i\alpha''$ with real and imaginary parts, α' and α'' , respectively. In equation (2-2), we associate the first term with the electric dipole-dipole interaction force, the second term with the scattering force, and the third term with a curl force associated to the non-uniform distribution of the spin density of the electric field. We note that the scattering force along the *z*-direction is much

smaller than the gradient force. Also since the scattering force is substantially constant in the vicinity of the focal spot and the typical vibration amplitude of the AFM cantilever is only 40 nm, we are not able to detect this force in our experiments. Furthermore, the curl force was zero due to the uniform distribution of the spin density of the electric field in the focal plane.

Experiments were performed using a tapping mode AFM and therefore only $\langle F_{opt,z} \rangle$ is the only component of the total force that is detected by the AFM cantilever. $\langle F_{opt,z} \rangle$ can be expanded in terms of the fields as

$$\langle F_{opt,z} \rangle = \Re\left(P_{tip,x} \frac{\partial E_{tip,z}}{\partial x} + P_{tip,y} \frac{\partial E_{tip,z}}{\partial y} + P_{tip,z} \frac{\partial E_{tip,z}}{\partial z} \right) \quad (2\text{-}3)$$

where, $p_{tip,x}$, $p_{tip,y}$ and $p_{tip,z}$ are the components of the electric dipole moment along the *x*, *y* and *z* axis respectively and $E_{tip,z}$ is *z* components of the total electric field on the AFM probe tip.

We model the interacting region of the tip as a prolate spheroid with $l > l'$, where, *2l* is the length of the major axis (along the *z*-axis) and *2l'* is the length of the minor axes . We note that $P_{tip,x} = P_{tip,y}$ assuming symmetry of the AFM tip.

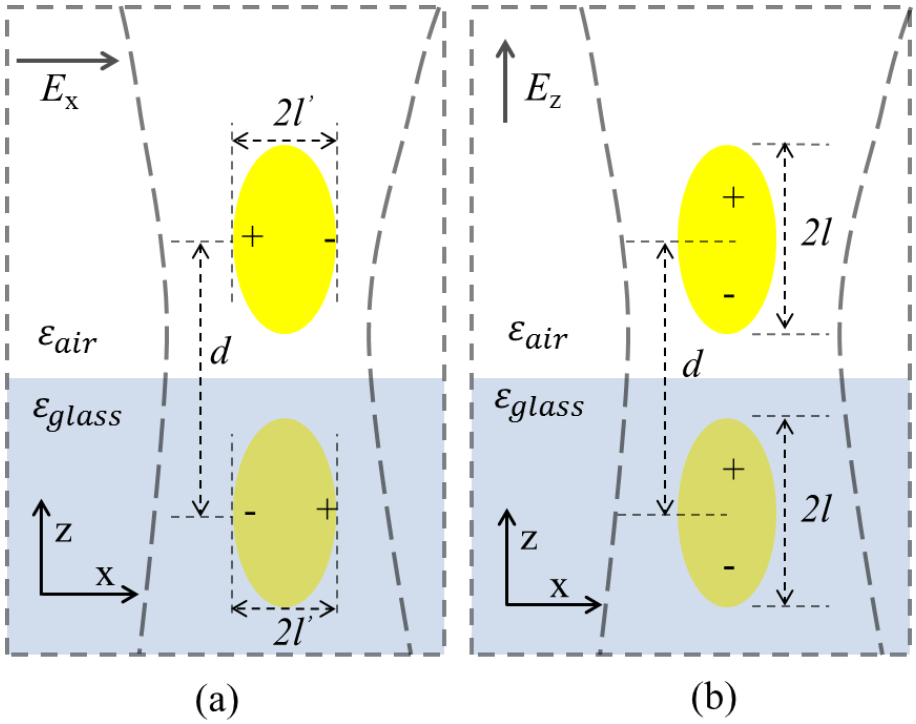

Figure 7 Tip sample interaction due to electric field modeled as the dipole-dipole interaction along (a) x direction, (b) z direction

The configurations of the dipole-dipole interaction model for E_z and E_x incident fields of the tip dipole and the image dipole are shown in. Assuming $l,l' << \lambda$ and using the electrostatic approximation, we obtain

$$\Re\left\{p_{tip,x}\frac{\partial E_{tip,z}}{\partial x}\right\} \approx \frac{24\pi\varepsilon_0 d\alpha'_{tip,x}\alpha'_{img,x}}{(d^2+l'^2)^{5/2}}\left|E_{focal,x}\right|^2 \tag{2-4}$$

$$\Re\left\{p_{tip,y}\frac{\partial E_{tip,z}}{\partial y}\right\} \approx \frac{24\pi\varepsilon_0 d\alpha'_{tip,y}\alpha'_{img,y}}{(d^2+l'^2)^{5/2}}\left|E_{focal,y}\right|^2 \tag{2-5}$$

$$\Re\left\{p_{tip,z}\frac{\partial E_{tip,z}}{\partial z}\right\} \approx \frac{8\pi\varepsilon_0\alpha'_{tip,z}\alpha'_{img,z}(3d^2+l^2)}{(d^2-l^2)^3}\left|E_{focal,z}\right|^2 \tag{2-6}$$

where, $\alpha'_{tip,x}$, $\alpha'_{tip,y}$ and $\alpha'_{tip,z}$ are the real part of electric polarizabilities of the prolate spheroid along the *x, y* and *z* axis and $\alpha'_{img,x}$, $\alpha'_{img,y}$ and $\alpha'_{img,z}$ are the real part of electric polarizabilities of the image dipole along the *x* , *y* and *z* axis. We note that the image dipole polarizabilities are proportional to the polarizabilities of the tip by the scaling factor $(\varepsilon_{sub}-\varepsilon_{air})/(\varepsilon_{sub}+\varepsilon_{air})$. In deriving (2-4),(2-5),(2-6), we have neglected terms with fast spatial decay rates of d^{-7} as our experimental setup is unable to detect signals with such rapid decay. Finally, the total detectable optical image force experienced by the tip is given by the sum of (2-4),(2-5),(2-6)

$$\vec{F}_{opt}=\frac{24\pi\varepsilon_0 d\alpha'_{tip,x}\alpha'_{img,x}}{\left(d^2+l'^2\right)^{5/2}}\left|E_{focal,x}\right|^2+\frac{24\pi\varepsilon_0 d\alpha'_{tip,y}\alpha'_{img,y}}{\left(d^2+l'^2\right)^{5/2}}\left|E_{focal,y}\right|^2 +\frac{8\pi\varepsilon_0\alpha'_{tip,z}\alpha'_{img,z}(3d^2+l^2)}{\left(d^2-l'^2\right)^3}\left|E_{focal,z}\right|^2 \qquad (2\text{-}7)$$

2.3 Focal field distribution calculation

From equation (2-7), we can see the optical induced force is proportional to the electrical field. Scan over a defined optical field distribution on a flat surface will give the optical force resolution and rule out the topography induced artifact. The tightly focused laser beam focal distribution is chosen since it is the smallest feature that can easily generate without any structure on surface.

Field distribution[33]has been calculate using angular spectrum representation in homogenous media. The angular spectrum representation of an optical field at arbitrary Z is

$$E(x,y,z) = \iint_{-\infty}^{\infty} \hat{E}(k_x,k_y;0)e^{i[k_x x+k_y y\pm k_z z]}dk_x dk_y \qquad (2\text{-}8)$$

Where k_x, k_y is the corresponding spatial frequencies.

Field distribution of focus a far-field onto the image plane

$$E(x,y,z) = \frac{ire^{-ikr}}{2\pi} \iint_{(k_x^2+k_y^2\le k^2)} E_\infty(k_x,k_y)e^{i[k_x x+k_y y\pm k_z z]}\frac{1}{k_z}dk_x dk_y \qquad (2\text{-}9)$$

To calculate the focal field distribution, we need to model the lens, we use two assumptions[33]. (1) sine condition (2)the intensity law, the energy carry along a ray is constant

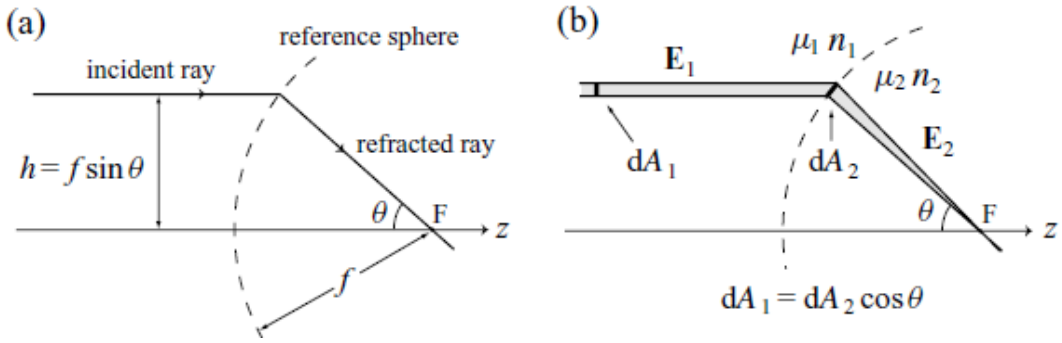

Figure 8 (a)sine condition(b) intensity law

Sine condition means $h = fsin\theta$ where f is the focal length of the objective.

Intensity law, the energy carry along a ray is constant, which can be interpret as

$|E_2| = |E_1|\sqrt{\frac{n_1}{n_2}}\sqrt{\frac{\mu_2}{\mu_1}}\sqrt{cos\theta}$,

Where E_2 is the electrical field after refraction, E_1 is the electrical field before refraction, n_1 , μ_1 is refraction index and permeability of media one, n_2 , μ_2 is refraction index and permeability of media two.

The focal field distribution is calculated using paraxial approximation[33].

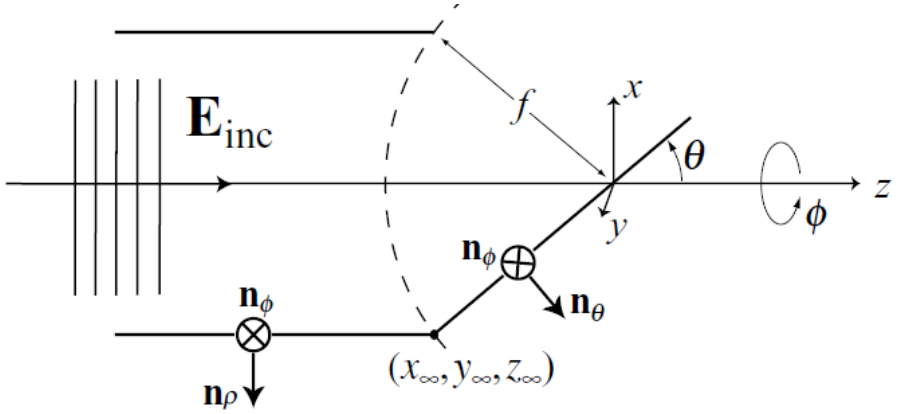

Figure 9 Definition of coordinates and lens geometry

To illustrate the incident ray focus effect by the lens, we discribe the coordinate change of the system as follows:

$$n_\rho = cos\phi n_x + sin\phi n_y \tag{2-10}$$

$$n_\phi = -sin\phi n_x + cos\phi n_y \tag{2-11}$$

$$n_\theta = cos\theta cos\phi n_x + cos\theta sin\phi n_y - sin\theta n_z \tag{2-12}$$

After changing coordinate, the far field electrical field can be expressed as:

$$E_\infty(\theta,\phi) = t^s(\theta)\left[E_{inc}(\theta,\phi) * \begin{pmatrix} -sin\phi \\ cos\phi \\ 0 \end{pmatrix}\right]\begin{pmatrix} -sin\phi \\ cos\phi \\ 0 \end{pmatrix}\sqrt{\frac{n_1}{n_2}}\sqrt{cos\theta} + t^p(\theta)\left[E_{inc}(\theta,\phi) * \begin{pmatrix} cos\phi \\ sin\phi \\ 0 \end{pmatrix}\right]\begin{pmatrix} cos\phi cos\theta \\ sin\phi cos\theta \\ -sin\theta \end{pmatrix}\sqrt{\frac{n_1}{n_2}}\sqrt{cos\theta} \quad (2\text{-}13)$$

Changing the coordinate and using the relationship of k and k_x, k_y, angular spectrum representation of the focal field[33] is

$$E(\rho,\varphi,z) = \frac{ikfe^{-ikr}}{2\pi}\int_0^{\theta_{max}}\int_0^{2\pi} E_\infty(\theta,\phi)e^{ik_z cos\theta}e^{ik_\rho sin\theta\cos(\phi-\varphi)}sin\theta d\phi d\theta \quad (2\text{-}14)$$

Where θ_{max} is dependent on NA of the objective, since $NA = nsin\theta_{max}$.

In our experiment setup, the focal distribution at the glass surface which has the glass air interface. To calculate the field distribution[33], we need to consider the interface effect. As shown in Figure 10, laser beam has focused on the glass air interface at z=0, using a NA=1.45 oil objective with focal length *f*.

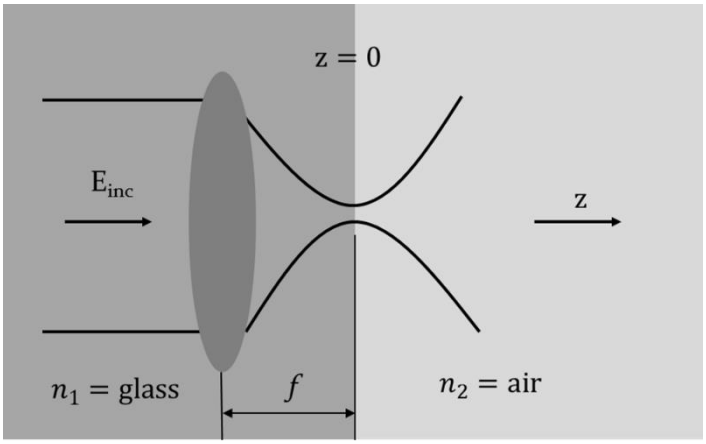

Figure 10 Focusing of a laser beam at z = 0 air glass interface

Assuming the incident field E_{inc} is polarized along the x axis and overfilled the back-aperture of the objective

$$\boldsymbol{E}_{inc} = E_{inc}\boldsymbol{n}_x \tag{2-15}$$

The paraxial beam approximation generate a focal field to illuminate the interface denote as E_f. Here assuming the polarization of the incident field is *x* direction. The far field [33]can be expressed as

$$E_\infty = E_{inc}(k_x, k_y)\begin{bmatrix} k_y^2 + k_x^2 k_{z_1}/k_1 \\ -k_x k_y + k_x k_y k_{z_1}/k_1 \\ 0 - (k_x^2 + k_y^2)k_x/k_1 \end{bmatrix}\frac{\sqrt{k_{z_1}/k_1}}{k_x^2 + k_y^2} \tag{2-16}$$

Where k_x, k_y is the spatial frequencies.

$$\mathrm{E}_f(x, y, z) = \frac{ife^{-ik_1 f}}{2\pi}\iint\limits_{k_x,k_y} E_\infty(k_x, k_y)e^{i[k_x x + k_y y \pm k_{z_1} z]}\frac{1}{k_{z_1}}dk_x dk_y \tag{2-17}$$

Far field electrical field of the transmitted field can be calculated using Fresnel transmission coefficients[33], as in equation (2-18)

$$\mathrm{E}_t^\infty = E_{inc}(k_x, k_y)e^{i(k_{z_1} - k_{z_2})z_0}\begin{bmatrix} t^s k_y^2 + t^p k_x^2 k_{z_1}/k_1 \\ -t^s k_x k_y + t^p\, k_x k_y k_{z_1}/k_1 \\ 0 - t^p(k_x^2 + k_y^2)k_x/k_1 \end{bmatrix}\frac{k_{z_2}}{k_{z_1}}\frac{\sqrt{k_{z_1}/k_1}}{k_x^2 + k_y^2} \tag{2-18}$$

The focal field distribution using angular spectrum representation can be calculated

$$\mathrm{E}_t(x, y, z) = \frac{ife^{-ik_1 f}}{2\pi}\iint\limits_{k_x,k_y} E_t^\infty(k_x, k_y)e^{i[k_x x + k_y y \pm k_{z_2} z]}\frac{1}{k_{z_2}}dk_x dk_y \tag{2-19}$$

From equation (2-19) we can calculate the focal field distribution.

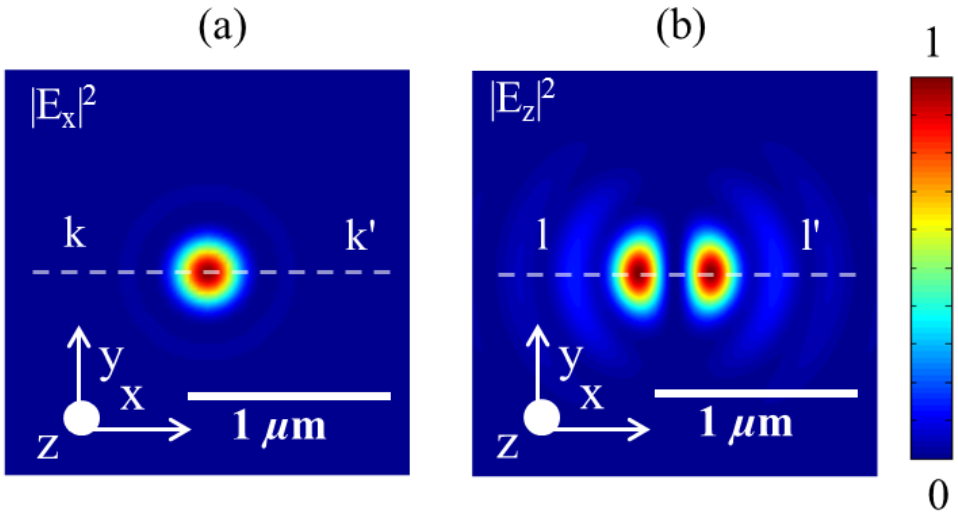

Figure 11 Spatial intensity distributions of focal field on glass with NA=1.45 at 640 nm of (a) $E_{focal,x}$ (b) $E_{focal,z}$

Matlab code is in appendix A. Spatial intensity distributions on glass at 640 nm calculation result is shown in Figure 11.

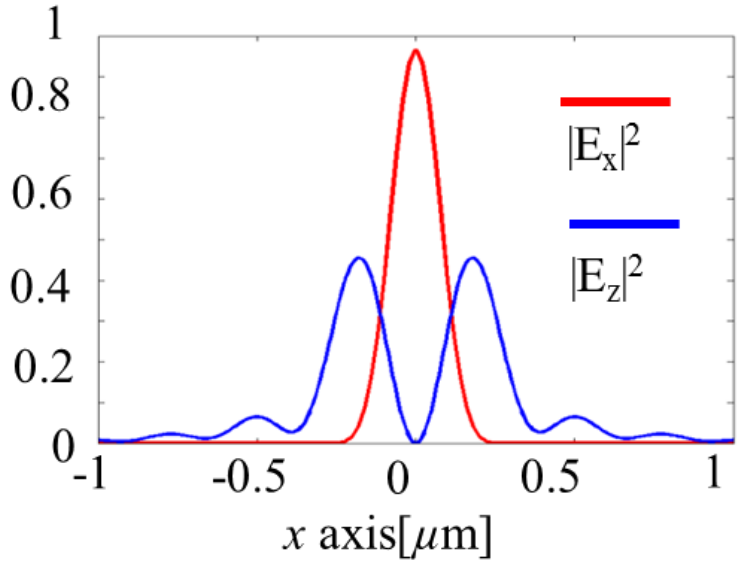

Figure 12 Comparison of line traces of $E_{focal,x}$ (along k-k') and $E_{focal,z}$ (along l-l') in Figure 11

After evaluation of (2-19), the focal field distribution for linearly polarized input light $\vec{E}_{inc}$ is known to contain components along both the transverse (x axis) and axial (z axis) Figure 12 plots the line traces of the numerically computed focal field intensity distributions for the transverse (line trace *k*-*k*' from Figure 11) and longitudinal (line trace *l*-*l*' from Figure 11) polarizations.

For the radial and azimuthal input polarized beam, since the incident laser beam has the cylindrical symmetry in polarization, the focal field distribution has been calculated[34] by using the cylindrical symmetry polarization property.

The incident beam is assume to be a Bessel-Gauss beam

$$I_0(\theta) = exp\left[-\beta_0^2\left(\frac{sin\theta}{sin\alpha}\right)^2\right]J_1\left(2\beta_0\frac{sin\theta}{sin\alpha}\right) \tag{2-20}$$

Where β_0 is the pupil radius and the beam waist, we use $\beta_0 = 3/2,\ \alpha = sin^{-1}(NA/n)$ in the experiment NA=1.45 oil objective is used, index of refraction of oil and glass is n=1.518, k = $2\pi/\lambda$, A is the incident electrical field amplitude, assuming A=1,

Since Bessel function has the property

$$\int_0^{2\pi} \cos(n\phi)\, e^{ik\rho_p sin\theta cos\theta} d\phi = 2\pi i^n J_n(k\rho_p sin\theta) \tag{2-21}$$

Use the same angular spectrum representation, the focal spot of radially polarized beam field distribution can be calculated as:

$$E_\rho(\rho, z) = A\int_0^a cos^{1/2}\theta sin(2\theta) I_0(\theta) J_1(k\rho sin\theta) e^{ikzcos\theta} d\theta \tag{2-22}$$

$$E_z(\rho,z) = 2iA\int_0^a cos^{1/2}\theta sin^2\theta I_0(\theta)J_0(k\rho sin\theta)e^{ikzcos\theta}d\theta \qquad (2\text{-}23)$$

From equation (2-22), (2-23), the electrical field distribution of the focal spot with radially input polarized beam can be evaluated.

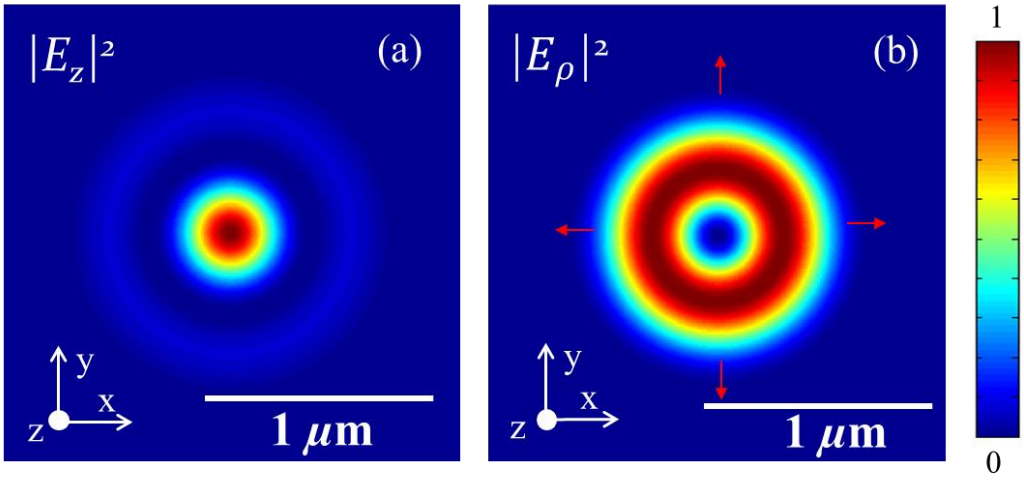

Figure 13 Spatial intensity distributions of focal field on glass with NA=1.45 at 640 nm of (a) E_z (b) E_ρ

As shown in Figure 13(a), in the center of the focal spot electrical field is purely longitudinal field, and in Figure 13(b), around the center which is a ring structure has transverse E_ρ component.

Use the same angular spectrum representation, the focal spot of azimuthal polarized beam field distribution can be calculated as:

$$E_\phi(\rho,z) = 2A\int_0^a cos^{1/2}\theta sin\theta I_0(\theta)J_1(k\rho sin\theta)e^{ikzcos\theta}d\theta \qquad (2\text{-}24)$$

From the equation (2-24), the focal spot of azimuthal polarized beam field distribution is evaluated on

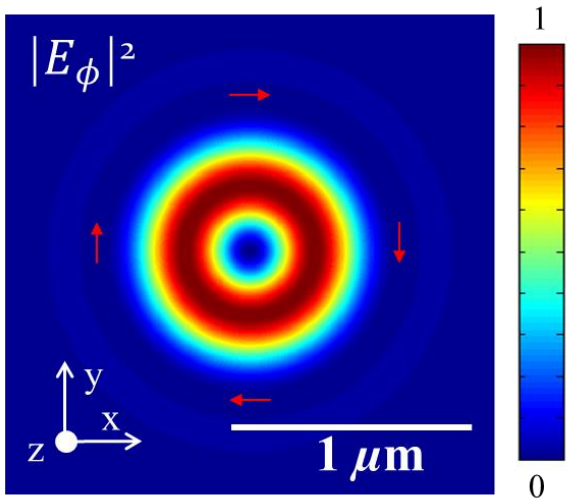

Figure 14 Spatial intensity distributions of focal field on glass with NA=1.45 at 640 nm of E_ϕ

As shown in Figure 14, the focal spot of azimuthal polarized beam field distribution has transverse E_ϕ component.

There are many research has been done to measure the electrical field distribution of the tightly focus beam[35,36]. By using a nano cone [34] or single nano particle[35] as a probe, the electrical field distribution of the tightly focus beam focal distribution can be experimentally measured.

2.4 Photon-induced force detection experimental setup

To detect the optical induced force, AFM is used as the force detector. There different modes of AFM and different modes of AFM detect different direction of force.

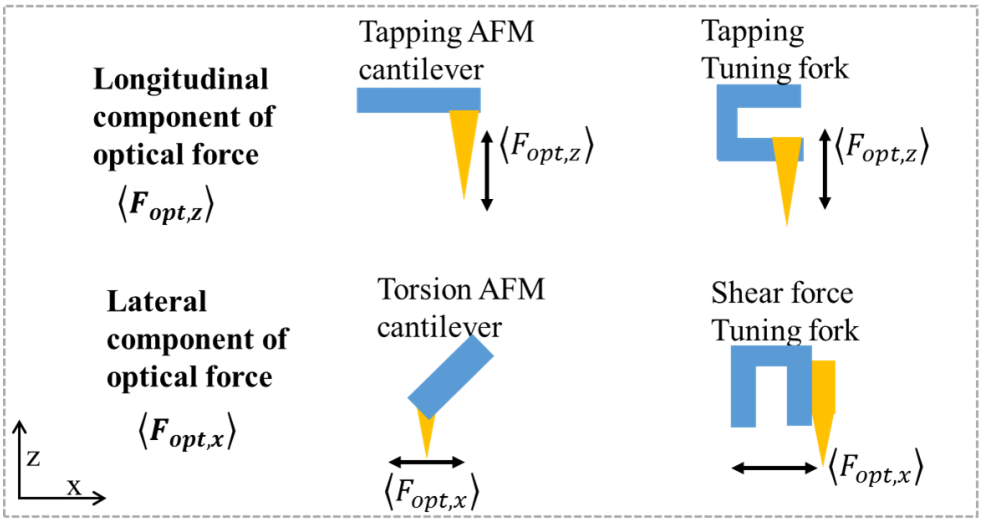

Figure 15 Different AFM working modes include tapping mode AFM, tuning fork AFM working in shear force, tuning fork AFM working in tapping mode detect force in x, or z direction

As shown in Figure 15, the AFM probe can be controlled using either tapping mode, shear-force feedback or tuning fork tapping mode. tapping mode AFM which detects force in z direction, tuning fork AFM working in shear force mode detects force in x direction, and tuning fork AFM working in tapping mode detects force in z direction.

To detect the optical induced force and control the tip sample gap, multi resonance frequency property of the AFM cantilever is used. The experimental results recorded the topography information using the first mechanical resonance of cantilever and the optical force signal from the second mechanical resonance of cantilever[22,23,29,37].

We can control the AFM probe over a surface to detect different components of the total force $\left\langle \vec{F}_{opt} \right\rangle = \left\langle F_{opt,x} \right\rangle \hat{x} + \left\langle F_{opt,y} \right\rangle \hat{y} + \left\langle F_{opt,z} \right\rangle \hat{z}$ experienced by the AFM tip. The experiment results were performed only using a tapping mode AFM (with AFM probe tapping along z

direction) and $\langle F_{opt,z} \rangle$ is the only component of the total force that is detected by the AFM cantilever. AFM in shear force feedback mode could be used to detect the *x*-component of the total time averaged optical force, $\langle F_{opt,x} \rangle$.

To detect the optical force, an AFM, optical and electronics elements have been used to build up the experiment setup.

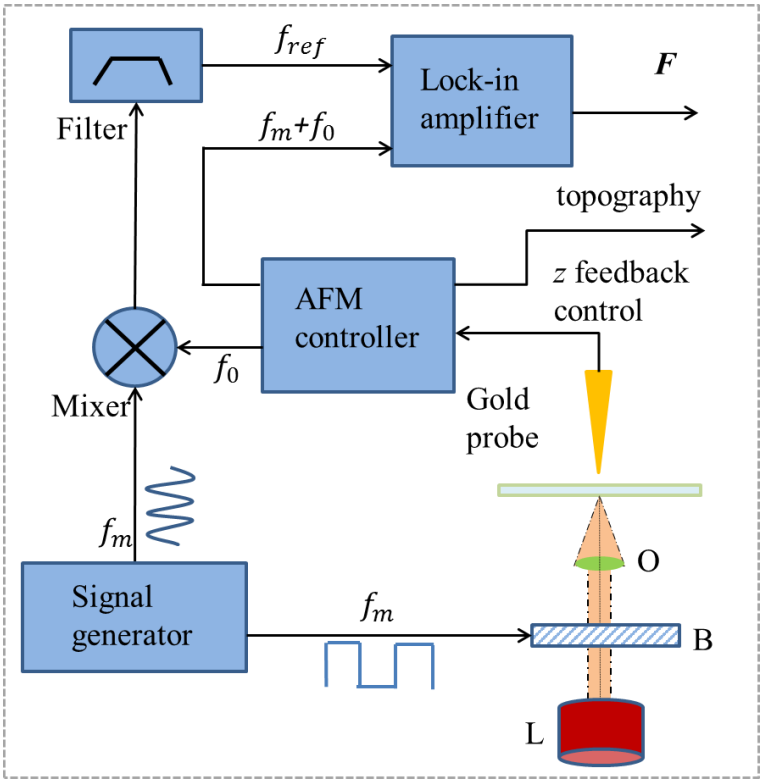

Figure 16 Schematic of Photo Induced Force Microscopy (PIFM)

The schematic of the experimental setup is shown in Figure 16. The experimental setup was built around a commercial AFM (Veeco Caliber) operating in the tapping mode. A Bragg cell modulator was used to modulate the desired wavelength laser which generate the optical field under measurement at the modulation frequency f_m. The laser focused on the

sample by using an oil immersion objective (PlanApo 100x) with NA = 1.45 on an inverted microscope (Olympus IX71) in transmission mode. The incident optical field was generated a tightly focused laser beam which induces a dipole at the end of the AFM probe. The attractive gradient optical force (***F***) between the induced dipole on the tip and its image dipole in the substrate is also modulated at frequency f_m. This attractive gradient optical force (***F***) modulates the AFM cantilever vibrates at its first mechanical resonance frequency f_0 will generate sidebands at f_0+f_m and f_0-f_m. We locate the sideband f_0+f_m on top of the second mechanical resonance frequency (f_1) of the AFM cantilever thereby utilizing the high Q of the second resonance of the AFM cantilever to enhance optical force signal. A lock-in amplifier was used to detect the optical force signal at the second mechanical resonance frequency. An electronic reference is derived by mixing the modulating frequency f_m with the cantilever drive signal at the first resonance frequency f_0 in a double balanced mixer followed by a bandpass filter centered at f0+fm. In our experiments, since we chose the AppNano Forta **k** = 1.6 N/m, $f_0 \sim 65$ kHz, $f_1 \sim 425$ kHz, so $f_m \sim 360$ kHz and the sideband frequency $f_0+f_m \sim 425$ kHz.

2.5 Photo-induced electric dipole force measurement

To measure the optical induced force, we first chose to measure the optical induced force map of the tightly focus beam on the glass substrate. We chose only measure the optical induced image dipole force since this will eliminate the topography effect, also eliminate the local thermal expansion effect. The tightly focus beam focal distribution also have distinct property of the polarization, which will affect the optical induced force map due to the tip.

2.5.1 Force measurement of focal distribution of tightly focused laser beam

By measuring the interaction between a gold coated AFM probe and its image dipole induced in glass substrate, the optical force distribution at the focus of a tightly focused laser beam is obtained. The input laser beam (incident on the microscope objective) was polarized along the x-axis and the back aperture was over filled to ensure a tight focal spot. The average power of the laser beam was 90 μW. The tapping amplitude of the AFM cantilever was 40 nm. The focal spot was raster scanned to simultaneously obtain distributions of topography and optical force.

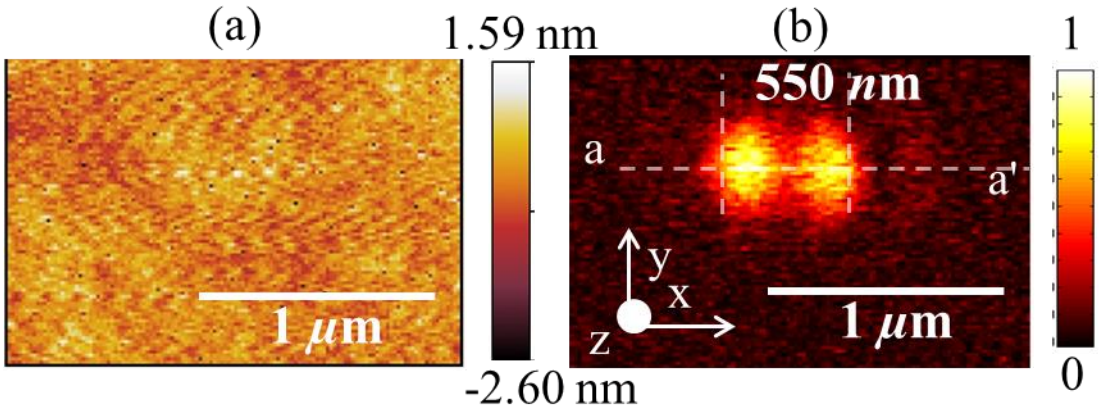

Figure 17 Spatial distributions of (a) topography and (b) normalized optical force measured experimentally on a clean glass microscope cover slide at 640 nm with light polarized along *x*-axis

Figure 17(a) and (b) show the topography and optical force distributions respectively recorded at a wavelength of 640nm. The measured optical force distribution plotted in Figure 17 (b) clearly exhibits two distinct peaks and the focal spot size of 550 nm at 640 nm

wavelength in Figure 17 (b). To explain what we have been measured, the optical force was numerically evaluated using the electrostatic approximation,

$$\vec{F}_{opt} = \frac{24\pi\varepsilon_0 d\alpha'_{tip,x}\alpha'_{img,x}}{\left(d^2+l'^2\right)^{5/2}}\left|E_{focal,x}\right|^2 + \frac{24\pi\varepsilon_0 d\alpha'_{tip,y}\alpha'_{img,y}}{\left(d^2+l'^2\right)^{5/2}}\left|E_{focal,y}\right|^2 + \frac{8\pi\varepsilon_0\alpha'_{tip,z}\alpha'_{img,z}(3d^2+l^2)}{\left(d^2-l'^2\right)^3}\left|E_{focal,z}\right|^2 \quad (2\text{-}25)$$

where, $\vec{F}_{opt,z}$, is the *z* component of the total time averaged force in the electrostatic limit, *2l* is the length of the major axis (along the *z*-axis) and *2l'* is the length of the minor axes, $\alpha'_{tip,x}\,\alpha'_{tip,x}$, $\alpha'_{tip,y}\,\alpha'_{tip,y}$ and $\alpha'_{tip,z}\,\alpha'_{tip,z}$ are the real part of electric polarizabilities of the prolate spheroid along the *x*, *y* and *z* axis [38] and $\alpha'_{img,x}\,\alpha'_{img,x}$, $\alpha'_{img,y}\,\alpha'_{img,y}$ and $\alpha'_{img,z}\,\alpha'_{img,z}$ are the real part of electric polarizabilities of the image dipole along the *x* , *y* and *z* axis. We note that the image dipole polarizabilities are proportional to the polarizabilities of the tip by the scaling factor $(\varepsilon_{sub}-\varepsilon_{air})/(\varepsilon_{sub}+\varepsilon_{air})$[39]. From equation (2-25), we note that the image force is a sum of three separate contributions from the interaction of the i^{th}-component of the field with the tip, where *i* = *x*, *y*, *z* and this property could be used to decompose the polarization dependence of the optical field under measurement. We calculated the electric field distribution at the focus of a tightly focused laser beam has explain in the previous section. For the linear input polarization $\vec{E}_{inc}\,\vec{E}_{inc}$, Due to the presence of both the *x* and *z* field components in the focal field distribution, $< F_{opt,z} >$ contains force terms due to both the *x* and *z* oriented electric dipoles interacting with the fields. Here, we ignore the *y* component of the focal field distribution as it is much smaller when compared to the *x* and *z* components.

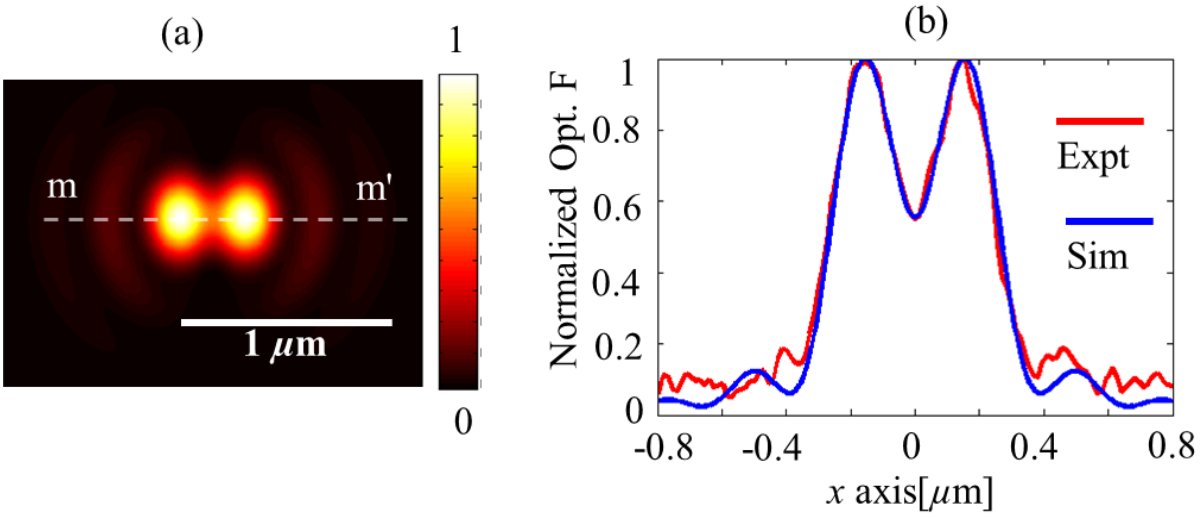

Figure 18 (a) Numerical calculations of normalized optical force obtained by evaluating (1) (b) Comparison of line traces of normalized optical force obtained experimentally (line a-a' in Fig.2 (b)) and calculations (line m-m' in (c))

To compare with the experimental results plotted in Figure 18 (b), equation (1) was numerically evaluated at 640 nm. The results plotted in Figure 18(a) agreed well with the experimentally measured data plotted in Figure 17 (b). Furthermore, a line trace extracted from Figure 17 (b) (along line a-a') was compared with the trace extracted from Figure 18 (a) (along line b-b') in Figure 18 (b).

To further verify our experimental findings, we mapped the focal field distribution at 660 nm for different polarizations of the input (incident on microscope objective) laser beam using the same gold coated AFM probe for all scans. The average power of the laser beam was 90μW.

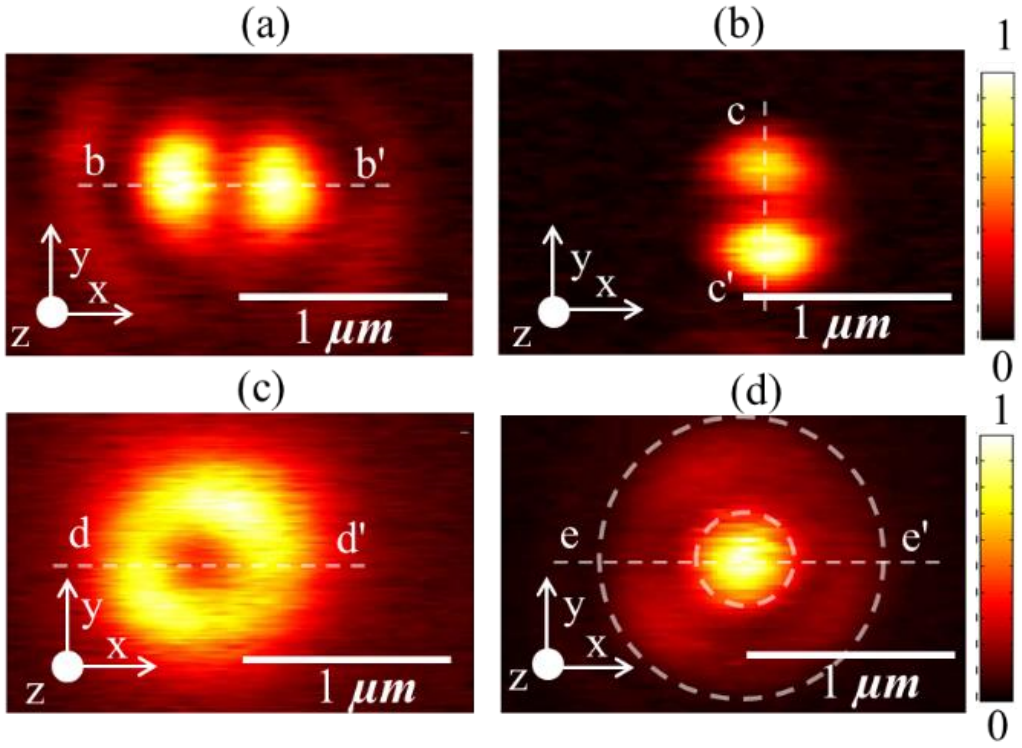

Figure 19 Spatial distributions of normalized optical induced force of tightly focused beam at 640nm (a) with polarization along x axis (b) with polarization rotated in-plane by 90° when compared to (a) (c) with azimuthal polarization (d) with radial polarization

As shown in Figure 19(a) to (d), spatial distributions of normalized optical force plotted were obtained for input light polarized along x axis, y axis (rotated using a half wave plate), azimuthal polarization and radial polarization (obtained using ARCoptix radial polarizer), respectively.

Since the normalized optical force distributions plotted in Figure 19 were all performed using the same gold coated AFM probe and at the same wavelength, we expect the experimental data can be explained using equation (2-25) for the same value of the ratio $\alpha'_{tip,z}/\alpha'_{tip,x}$. The line traces extracted from Figure 19 (a) (along line b-b') and Figure 19 (d)

(along line e-e') were compared with an equivalent line traces obtained from numerical calculations in Figure 20(a) and (b), respectively.

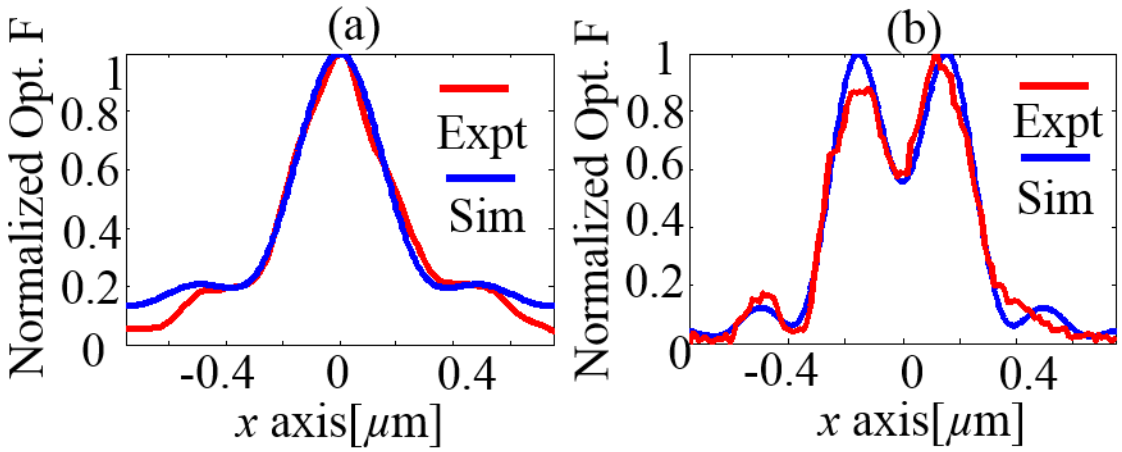

Figure 20 (a) Comparison of line traces of normalized optical force obtained experimentally from curve b-b' in Figure 19(a) and numerical calculations (b) Comparison of line traces of normalized optical force obtained experimentally from curve e-e' in Figure 19 (d) and numerical calculations

In both cases, we find the experimentally measured optical force data agrees well with the numerical calculations while maintaining the same value of the ratio $\alpha'_{tip,z}/\alpha'_{tip,x}$ ~16.42 thereby validating the technique proposed in this work. We note that the focal field distribution of a tightly focused laser beam with input radial polarization consists of two distinct regions with orthogonal polarizations. The central peak is a purely longitudinally polarized (E_z) field and the circular ring surrounding the central ring is a purely transverse polarized (E_ρ) field [40]. In addition, as shown in Figure 19 (c) (along line d-d'), the Full Width Half Maximum (FWHM) of the dip in the normalized optical force distribution is 337 nm and agrees well with both numerical calculations and previously published data[40]. For the

normalized optical force distribution for input radial polarization shown in Figure 19 (d) (along line e-e'), the FWHM of the focal spot is 356 nm and agrees well with both numerical calculations and previously published data [40].

2.5.2 Force measurement dependent variables

From previous session, the experimentally measured optical force data agreed well with the numerical calculations. The force map of the tightly focused beam demonstrates that measurements of optical forces due to the focal field distributions can be used to estimate the ratio $\alpha'_{tip,z} / \alpha'_{tip,x}$. Measurements of optical forces also gain insight into the physical structure of the sharp tip end interacting with the optical field. Experiments were repeated for different gold coated AFM probes to understand the tip effect of the optical induced force. Four different tips has been used to measure the force map of the tightly focus beam using system as Figure 16. The centerlines of the focal spot along x axis with input wavelength 680nm have been plotted.

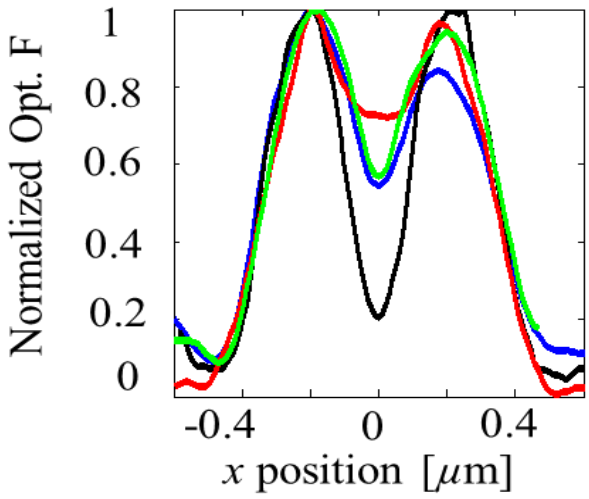

Figure 21 Normalized optical force measured experimentally with different gold coated AFM probes.

As shown in Figure 21, the experiment results indicate a large variability in the repeatability of structural parameters of gold coated AFM probes produced by our gold coating technique. The result also clearly shows the optical induced force measurement is very sensitive to the very end of the tip. Small sputter condition change will affect the z polarization enhancement.

The tip shape and the interaction region of the tip sample distance are very important factors of the resolution of the optical induced force. A series of experiment has been done. We first use the fresh Au coated tip raster scan the tightly focus laser beam using the same experiment setup Figure 16, which will show the original tip property, locate the position of z polarization(the black cross), record an amplitude and optical induced force distance curve, which means the AFM is hard contact with the substrate. After hard contact, raster scan the same tightly focus beam, which will show the tip property of changed tip end.

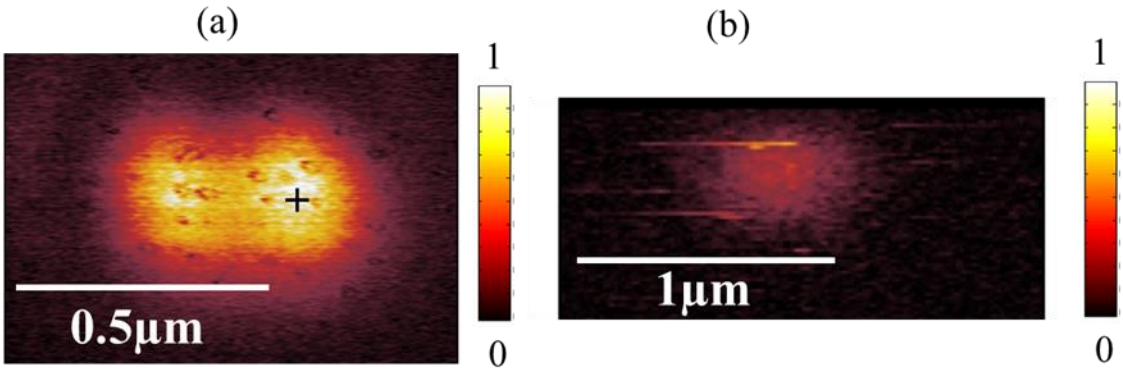

Figure 22 Spatial distributions of normalized optical force measured on glass at 680 nm with polarization along *x*-axis (a)before tip hard contact substrate (b) after tip hard contact substrate

From Figure 22(a), the new coated tip has along z (tip axis) enhancement than the x axis. From Figure 22(b), after AFM tip hard contact to the substrate, force map of the electric field distribution of the tightly focus beam clearly shows the tip z enhancement is lower which means the tip end has changed due to the hard contact.

The amplitude force distance will give us many information about the photon-induced force experiment. As equation (2-25), with the z polarization light excitation, optical induced force has d^{-4} dependence which indicate the optical induced force is very sensitive to the tip sample distance.

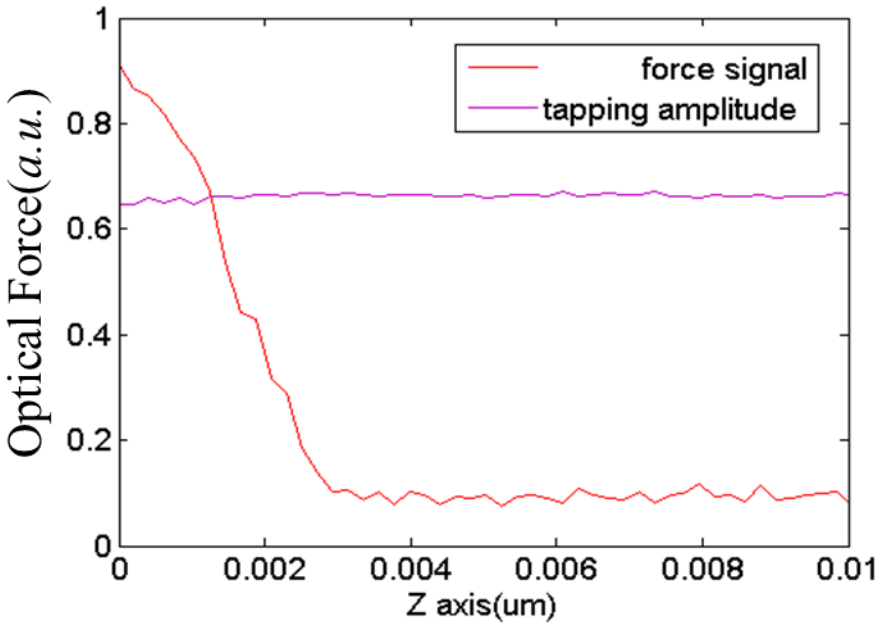

Figure 23 Amplitude VS optical induced force distance curve

From Figure 23, we experimentally measure the amplitude VS optical induced force curve. We can infer from the curve that at 40nm free space taping amplitude, when the tip come near the surface, the optical force increase dramatically. This curve also indicates when we measure the optical induced force, the control condition of the vibration of the tip.

The power level of the excitation laser is also an important factor, as in equation (2-25) the optical induced force is linear with the power level. A series of scans has been done to experimentally measure the optical force with different laser power level excitation. We use the experimental setup shown in Figure 16 with wavelength 680 scan over the tightly focus on the glass substrate. The optical induced force map is shown in Figure 24, the extracted peak value of the z polarization and the power level input is shown in Figure 25.

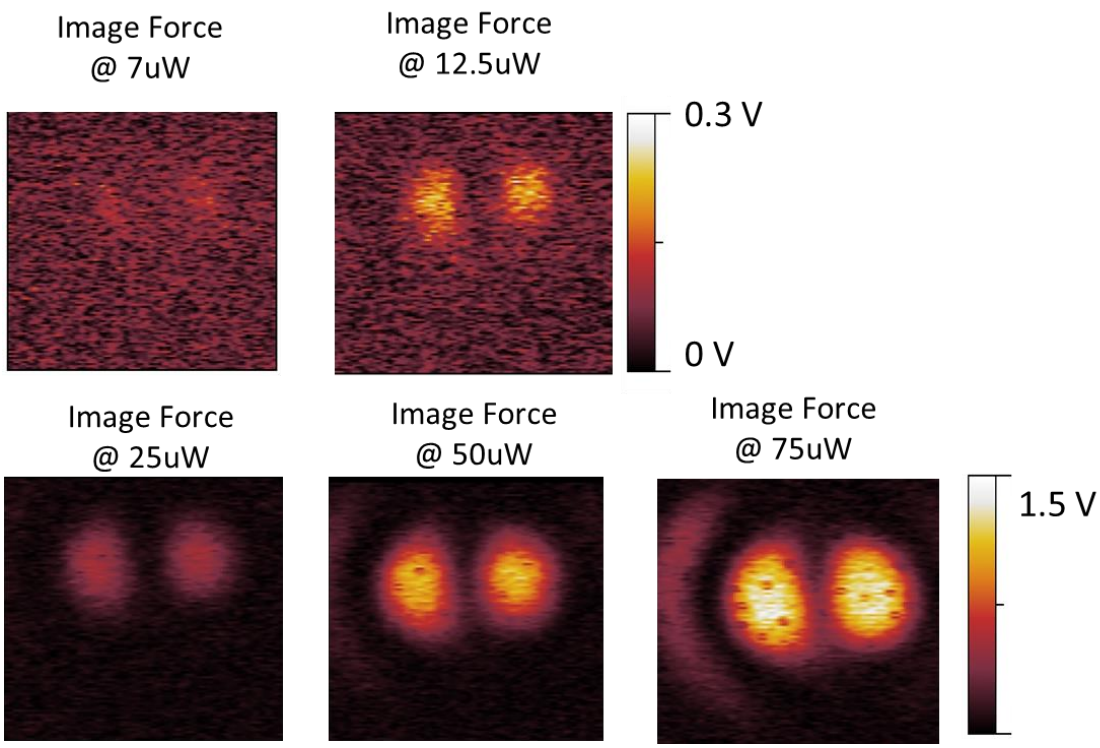

Figure 24 Spatial distributions of normalized optical force measured on glass at 680 nm with polarization along *x*-axis with different power input

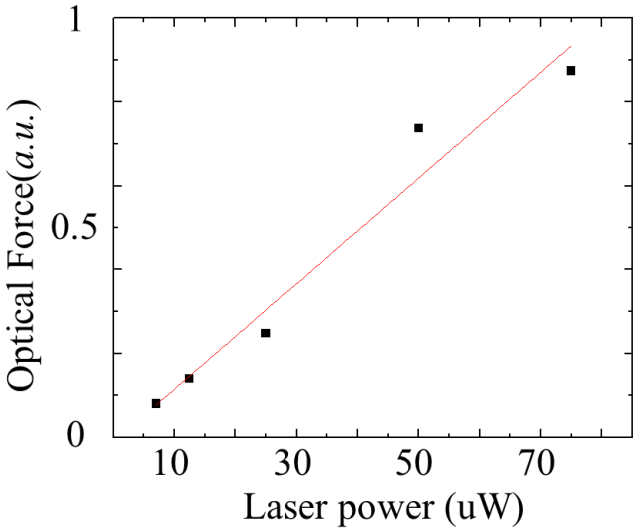

Figure 25 Optical induced force VS laser input power density

From Figure 24 and Figure 25, the optical induced force is linear with respect to the laser input power level within the small power level input region, which agrees well with the theoretical prediction.

2.5.3 Force measurement on thin film

To verify that optical force measurements are indeed measuring optically induced forces and not opto-thermal effects, we performed experiments with different samples that have distinctly different thermal diffusion lengths and obtained the normalized optical force distributions.

Since we want to use the same experiment setup which is transmission mode, using the bottom illumination, an ultra-flat surface with light transmission was chosen to be the sample to compare with only glass substrate. 10 nm Au film is chosen since the skin depth of Au is around 30nm, 10 nm Au film will allow most of the light intensity go through.

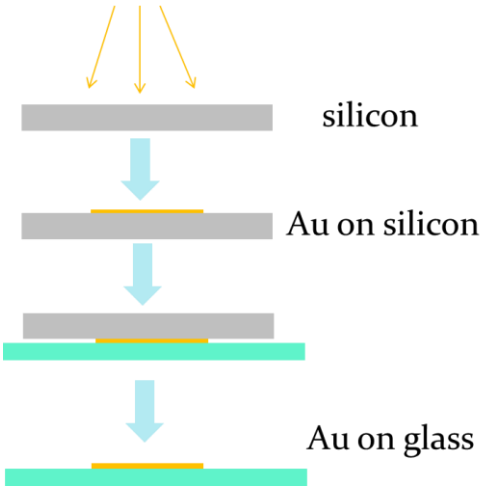

Figure 26 Fabrication steps of template striped gold on glass

To make sure the surface is ultra-flat, template striped gold is used. The fabrication process is described in Figure 26. A piece of solvent clean silicon is sputter coated (south bay technology) with 10 nm of Au with no rotation angle. Clean glass cover slip is glued to the Au using optical clear UV curable epoxy (Thorlabs NOA 61). After applied UV exposed 20 min, the silicon is taken off using razor blade. Ultraflat gold surface with roughness of 0.15 nm – 0.35 nm on the glass cover slide has been made.

The template striped gold on 0.16mm glass cover slip is putting in the setup Figure 16 to measure the optical induced force. The optical induced force between a gold coated AFM probe and its image dipole induced in 10nm template striped gold substrate exited by the tightly focused laser beam is measured.

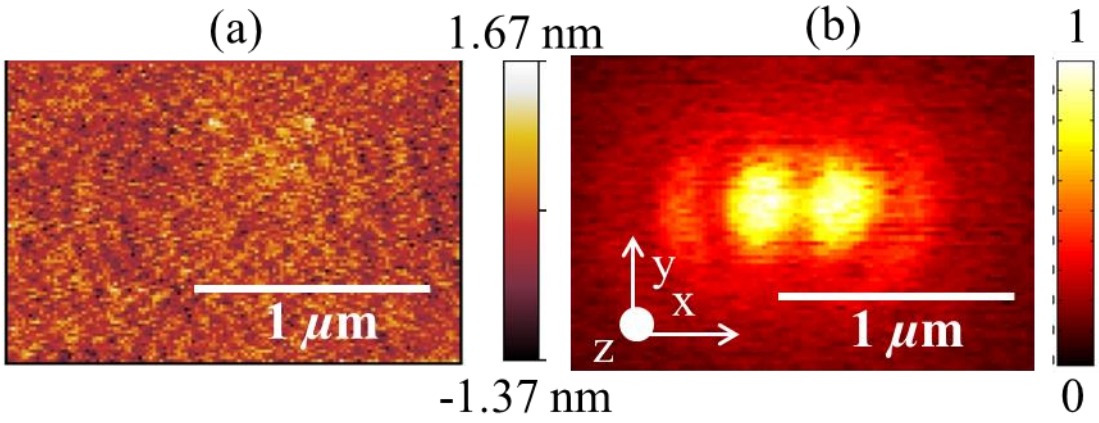

Figure 27 (a) Topography of template stripped gold surface (b) Normalized optical force measured on template stripped gold surface at 685 nm with light polarized along x-axis.

The optical force distribution at the focus of a tightly focused laser beam at a wavelength of 685nm is shown in Figure 27. The input laser beam (incident on the microscope objective) was polarized along the *x*-axis and the back aperture was over filled

to ensure a tight focal spot. The average power of the laser beam was 90 μW. The tapping amplitude of the AFM cantilever was 40 nm. The focal spot was raster scanned to simultaneously obtain distributions of topography and optical force.

The calculation of thermal diffusion length is $L_g = \sqrt{D/(\pi f_m)}$ [41], where D is the thermal diffusivity of glass and f_m is the optical chopping frequency. The thermal diffusion length of glass is 661 nm at our chopping frequency, whereas our optical force measurement shows a spot size of only 550 nm as shown in Figure 17(b). For a 10 nm thick template stripped gold film on glass, the thermal diffusion length is estimated to be ~7.7 μm [41] at our chopping frequency. However, the measured optical force distribution of the tightly focused laser beam on the template stripped gold surface, shown in Figure 27 (b), has essentially the same distribution as that of Figure 17(b) – a spot size of 550 nm, much smaller than the thermal diffusion length. The comparison with different substrates clearly indicating the measurement is optically induced forces and not due to opto-thermal effects.

From equation (2-25), optical induced force is sensitive to the local electrical field distribution on the surface. A rough surface which will give random change of local polarization is a good sample to measure. As we have shown previously, the templated strip gold surface has been tested for the purpose of the opto-thermal effects of different substrates that have distinctly different thermal diffusion lengths. To do a good comparison, we still use the 10nm Au thin film which is thermally evaporate on a clean 0.16mm glass

surface. Using the same experiment setup shown as in Figure 16, the tightly focus laser spot has been raster scanned to measure the local field distribution.

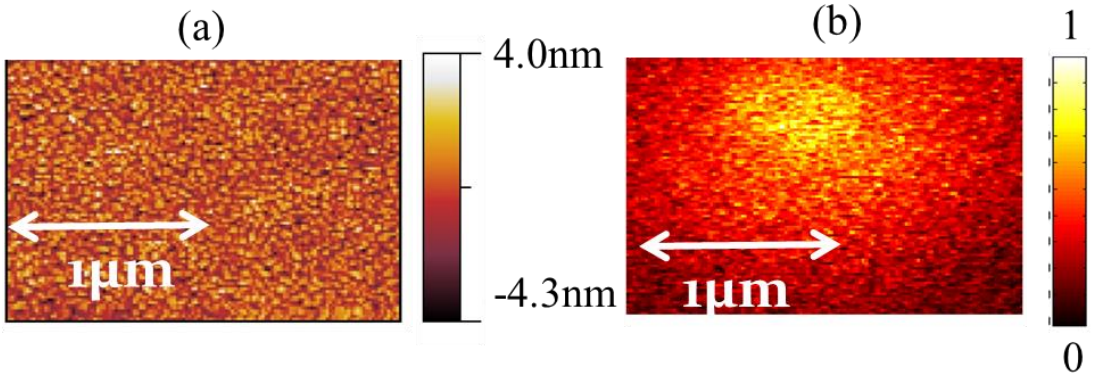

Figure 28 (a) Topography of thermal evaporated gold surface (b) Normalized optical force measured on thermal evaporated gold surface at 685 nm with light polarized along x-axis.

The simultaneously obtained topography and normalized optical force map is shown in Figure 28.The reason that we have obtain only a bright spot is that the polarization of the focus beam has been scrambled by the rough surface. From the boundary condition, $E_{z_1}\varepsilon_1 = E_{z_2}\varepsilon_2$, where Z is normal to the surface direction, E_x along the surface should be continuous.

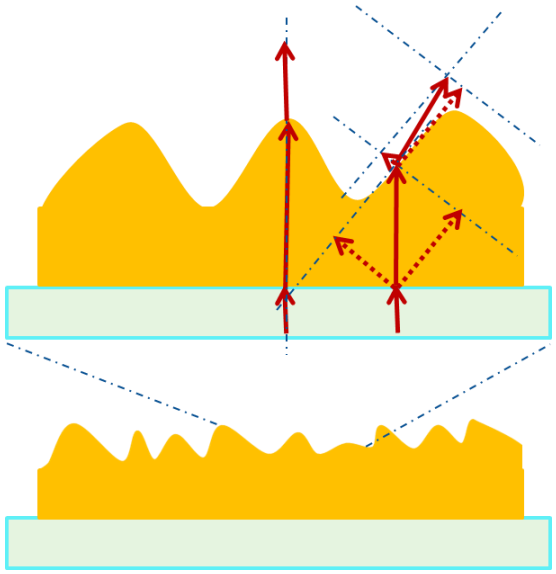

Figure 29 Roughness of the surface change the local optical field direction

As shown in Figure 29, the small feature of the surface change the local optical field direction, causing the force map of the spot has the spatial distribution as Figure 28 (b).

2.5.4 Force measurement of Au nano-particle

Local electrical field distribution of nano particle has been well studied theoretically. Measuring the electrical field distribution mainly has been done using scattering nearfield microscope. Local optical electrical field distribution has been widely used in single molecule detection, surface-enhanced Raman scattering, tip-enhanced Raman scattering. Here we propose a new way of mapping the local electrical field distribution.

We measure the optical force map of the optical induced local field distribution at nanometer resolution of the nano particle between a gold coated AFM probe and single gold nanoparticles of radius 15 nm (nano partz, A11-30- Carboxylic Acid-DI-25).

1 mL Gold nanoparticle of radius 15 nm from commercial aqueous nanoparticle in DI water were centrifuged at 13,000 rpm for 20 minutes to remove surfactants. By rinsing 0.16 mm thick glass cover slides in acetone, methanol and isopropanol consecutively, glass substrate were cleaned. 10 μl of the resulting nanoparticle solution with particle concentration 2×10^{11} /ml was drop cast onto a clean glass surface, gently blow dry to make mono disperse nano particle on glass.

The nanoparticles were placed in the focal spot of a tightly focused laser beam and the input light was radially polarized at a wavelength of 660 nm. The average power of the laser beam was 90 μW. The measured optical force distribution of the focal spot (before introduction of the nanoparticles) is plotted in Figure 30(b). The mono disperse nanoparticles were raster scanned using a gold coated AFM probe to simultaneously obtain topography and normalized optical force plotted as shown in Figure 30(c) and (d), respectively.

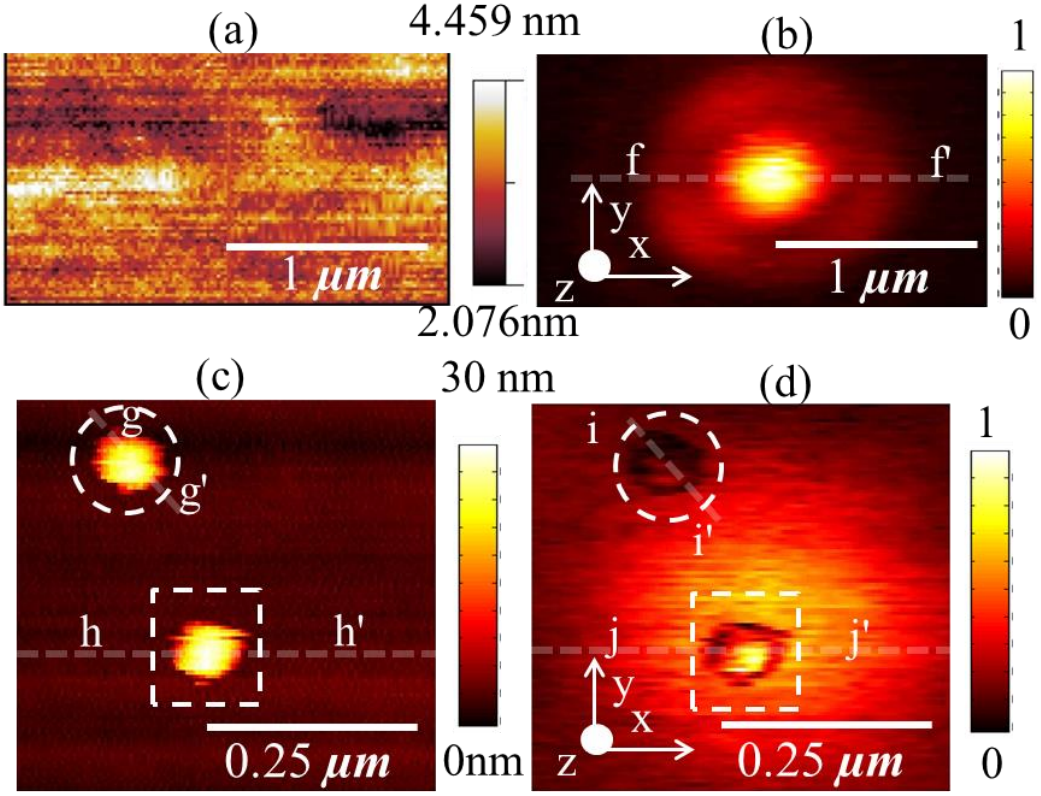

Figure 30 Spatial distributions of (a) topography and (b) normalized optical image force measured experimentally on clean glass slide at 660 nm with radially polarized input light (c) topography and (d) normalized optical image force measured experimentally on two gold nanoparticles of radius 15 nm on a cleaned glass surface at 660 nm with radially polarized input light.

Since the incident laser beam is radially polarized, as described previously, the focal distribution has two components, the central spot with purely longitudinal fields, and the circular ring with purely transverse fields. In Figure 30(d), we present the optical force distributions of two gold nanoparticles of radius 15 nm. The first nanoparticle was positioned to be within the central spot with purely longitudinal fields (bounded by the

dashed box) and the second nanoparticle was located within the circular ring with purely transverse fields (bounded by a dashed circle).

To further study the observed results, we performed numerical calculations using a commercial finite element solver COMSOL Multiphysics. The apex of the gold coated AFM probe was modeled as an ellipsoid composed of gold and the theoretical AFM topography was traced over the gold nanoparticle as shown schematically in Figure 32(c).

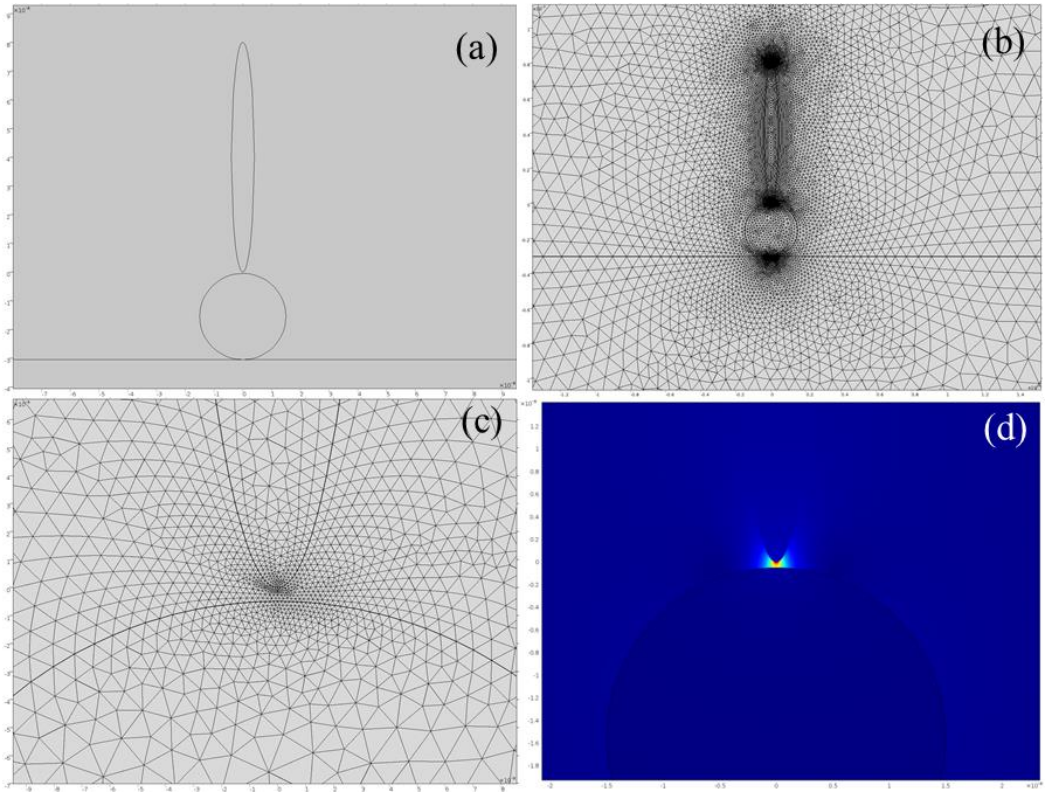

Figure 31 Model used in numerical calculations with elliptical gold tip scanning over the spherical gold nanoparticle (a) Comsol geometry(b)meshing of Comsol(c)zoomin mesh of the AFM tip (d) electrical field distribution with wavelength 660 nm

The force experienced by the elliptical gold nanoparticle as it traversed the theoretical curve around the gold nanoparticle was calculated by evaluating the Maxwell stress tensor using the electric fields obtained from COMSOL simulations.

The Maxwell stress tensor component can be written as

$$T_{ij} = \varepsilon_0 \varepsilon_m E_i E_j^* + \mu_0 \mu_m H_i H_j^* - \frac{1}{2}\delta_{ij}(\varepsilon_0 \varepsilon_m |E|^2 + \mu_0 \mu_m |H|^2) \quad (2\text{-}26)$$

Where, $E_i$is the electric field, H_i is the magnetic field, $\varepsilon_m$is the relative electric permittivity, and μ_m is the relative magnetic permeability. In our simulation, the AFM tip is modeled as an ellipsoid composed of gold.

The force experience on the ellipsoid composed of gold is

$$\langle F_i \rangle = \frac{1}{2} Re\left(\int_c T_{ij}.n_j dS\right) \quad (2\text{-}27)$$

The gold coated tip modeled as an ellipsoid has l = 40 nm, l'=4 nm. The optical constants of metals used to obtain results were obtained from previous publication[42].

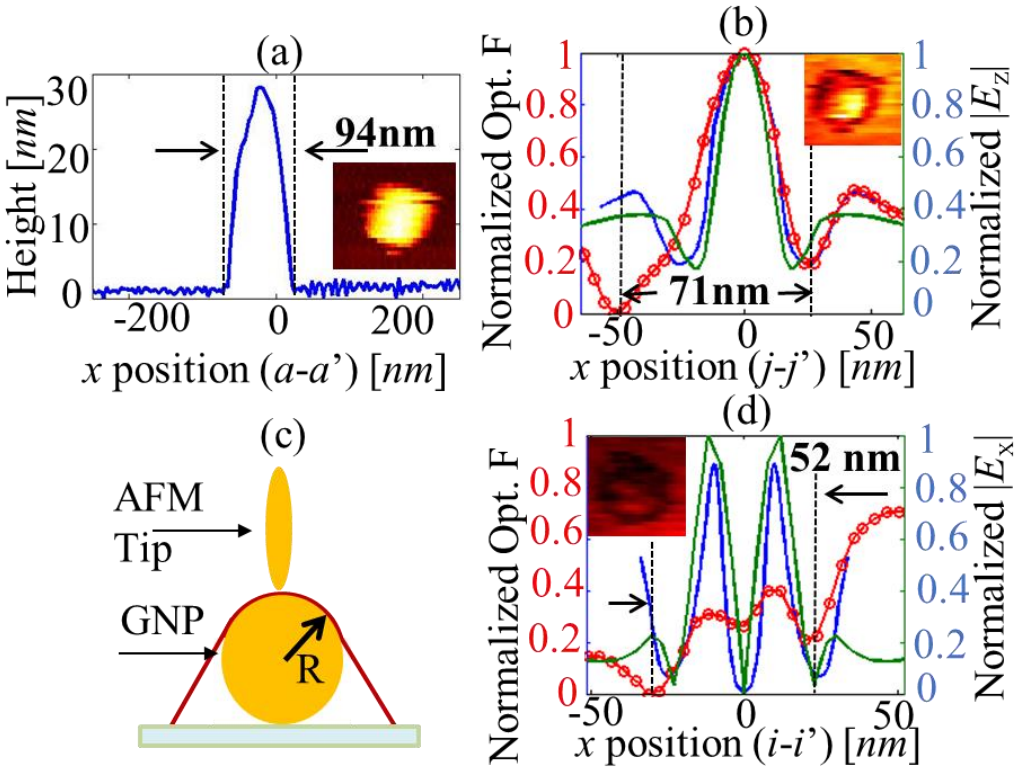

Figure 32 (a) line scan of topography indicating feature size of 94 nm (b) line scan of normalized optical force (from experiment in red color) with spherical gold nanoparticle in the longitudinal incident field compared with the line scans of normalized optical force (in blue color) and normalized |Ez|2 of only nanoparticle (in green color) from numerical calculations (c) Model used in numerical calculations with elliptical gold nanoparticle scanning over the spherical gold nanoparticle and following the theoretical AFM topography curve (d) line scan of normalized optical force (from experiment in red color) with spherical gold nanoparticle in the transverse incident field and compared with the line scans of normalized optical force (in blue color) and normalized |Eρ|2 of only nanoparticle (in green color) from numerical calculations.

The normalized optical force distribution between a gold coated AFM probe and gold nanoparticles optical forces of radius 15 nm is shown in Figure 30 (d). Line traces of the topography and normalized were extracted from Figure 30 (c) (along line h-h') and Figure 30 (d) (along line j-j' and i-i') and plotted in Figure 32 (a), (b) (in red color) and (c) (in red color), respectively. The inset in Figure 32 (b) and Figure 32 (c) show zoomed-in plots of optical force distributions on the corresponding nanoparticles.

The feature width in the line trace of topography plotted in Figure 32 (a) is 94 nm and the broadening is attributed to the convolution of the sample with the probe apex geometry. The width of the measured optical force due to the nanoparticle located in the longitudinal ($|E_z|$) field and extracted from the normalized optical force plotted in Figure 32(b) was found to be considerably smaller at 71 nm, or ~λ/9.29 at a wavelength of 660 nm.

To further study the observed results, we performed numerical calculations using a commercial finite element solver COMSOL Multiphysics. The apex of the gold coated AFM probe was modeled as an ellipsoid composed of gold and the theoretical AFM topography was traced over the gold nanoparticle as shown schematically in Figure 32(c). The force experienced by tip as it followed the theoretical curve around the gold nanoparticle was calculated by evaluating the Maxwell stress tensor using the electric fields obtained from COMSOL simulations.

Line traces of calculated optical forces for both the longitudinal ($|E_z|$) and transverse ($|E_\rho|$) fields using the same theoretical topography curve are also plotted in and Figure 32(d), respectively (both in blue color) and compared with experimental data. Also, calculations of the EM fields around a single gold nanoparticle of radius 15 nm on glass substrate for the

same incident field conditions used to simulate optical force results in Figure 32(b) and (d) were performed using COMSOL. The values of the $|E_z|^2$ and $|E_\rho|^2$ components along the theoretical AFM topographical curve were extracted, normalized and plotted along with the normalized force in Figure 32(b) and (d), respectively (on secondary y axes, in green color). The results of these simple simulations are generally in reasonable agreement with experiment and predict the right trends. The slightly broadened experimental data can be explained by considering scanning convolution of the shape of the AFM probe.

The optical force is in agreement with the calculated field distributions for the bare nanoparticle suggesting that PIFM can measure optical field distributions. However, it is a typical phenomenon of scanning probe measurement, the optical force maps should be expected to be the interaction of the nano particle and the tip, which the electrical field of the nano particle is perturbed by tip apex. Similar to *s*-NSOM, the degree of interaction between tip and sample will determine the perturbation in the measured fields[43]. For the case of strong tip-sample coupling, the normalized optical force maps the interaction forces between the gold coated AFM probe and the sample, indicates the gap mode dominated electric field distribution between the sample and gold coated AFM probe. Such experiments could be very useful to understand the hotspots between closely coupled nanoparticles.

From our experiment, we have shown the strong optical induced force between a gold coated silicon tip and the gold nano particle, which shown the gap mode dominate the electric field distribution. To change the perturbation of the electrical field distribution, different AFM probe materials could be used to obtain optical force using our experimental setup. From our experiments, the peak value of optical force, measured at the second

mechanical resonance of the cantilever, between a gold coated AFM probe and the gold nanoparticle is 18.5 times higher than the thermal noise of the cantilever in 8 Hz bandwidth.

To understand how much is the optical induced force change relative to the tip material, Comsol simulation has been done. Coated AFM probes with different material is modeled as a solid ellipsoid with the coating material. The optical force between an AFM tip and the gold nanoparticle of radius 15 nm was numerically evaluated using COMSOL for different coating materials.

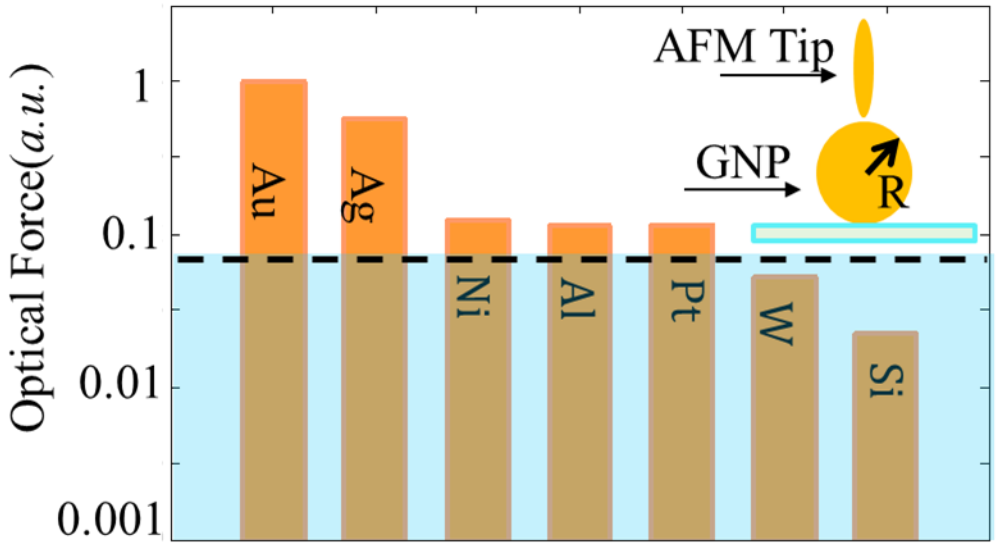

Figure 33 COMSOL simulation of Normalized optical induced force between AFM tips of different permittivity and a 30 nm Au particle with incident light at 660nm in the |Ez| incident field

The geometry used in the calculation is shown Figure 33 inset. Plots of the optical force calculated for ellipsoids composed of different materials normalized by the optical force calculated for an ellipsoid of gold.

The dashed line indicates the thermal noise measured at the second mechanical resonance of the cantilever. The thermal noise is the limit of measurement for our experimental setup. From Figure 33, for the current setup, we can only use gold or silver tips to obtain measureable optical forces. Other metals such as nickel, platinum and aluminum produce optical forces which are only 2 times above the thermal noise.

To demonstrate theoretically that we can use our technique to map modal distributions, we used COMSOL simulations to calculate the optical force on an ellipsoidal AFM tip scanning a 500 nm gold nano rod driven by an optical field at 580 nm polarized ang its x- axis shown as in

Figure 34.

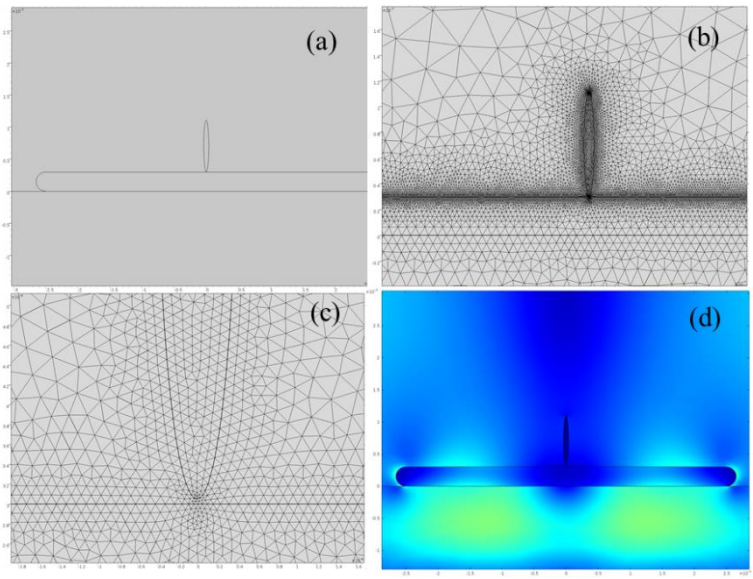

Figure 34 Model used in numerical calculations with elliptical gold nanoparticle scanning over the 500nm gold nanorod. (a) Comsol geometry(b)meshing of Comsol(c)zoomin mesh of the AFM tip (d) electrical field distribution with wavelength 580 nm

The calculated optical force map for an AFM tip scanning over the nano rod is plotted in Figure 35, which clearly reveals the Fabry-Perot modes of the nano rod.

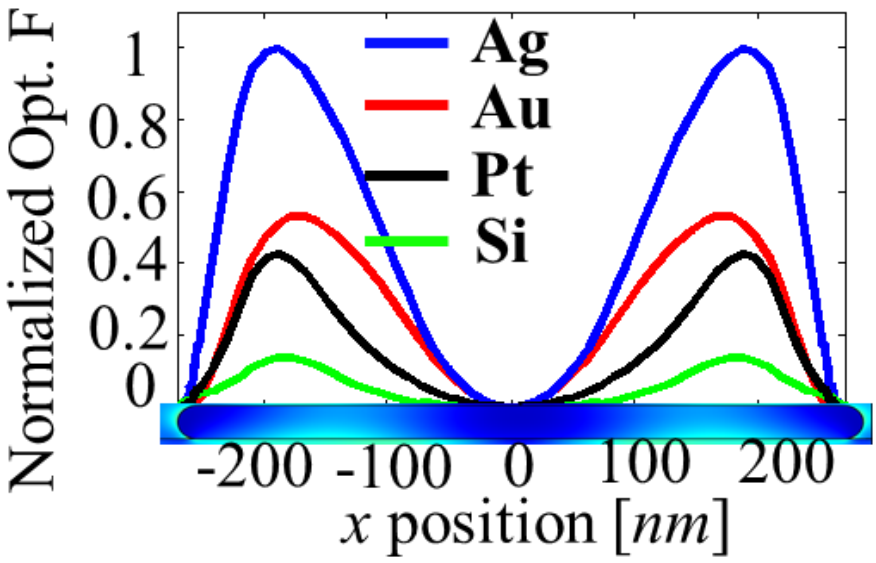

Figure 35 Line scan of normalized optical force of different tip permittivity at 580 nm wavelength on 500nm gold nano rod in the Ex incident field calculated by Comsol

2.6 System improvement

Since our measurement method is a near-field excitation and near-field detection other than near-field excitation and far-field detection in other tip-enhanced near-field optical microscopy techniques, as the interaction region is nanometer range, PIFM gives high spatial resolution. Also the detection channel is the force base detection method, the background noise will be simply the thermal excitation of the second flexure eigen mode of the AFM cantilever, which is

$$N^2 = 4\,KTBQ_2/\omega_2 k_2 \qquad (2\text{-}28)$$

where K is Boltzmann constant, T is the temperature at the measurement, B is the system bandwidth(related to the measurement time constant), $Q_2$is the quality factor of the cantilever second flexure eigen mode, ω_2 is the second flexure eigen mode resonance angular frequency. Under the condition the experiment has been done. K= 1.38 × 10^{-23} m^2 kg s^{-2} K^{-1}, T = 300K, B = 100 Hz, Q_2 = 400, k_2= 39 N/m andω_2 = 2 *π* 380 kHz, N=2.43x10^{-4} nm.

From equation (2-28), it is obvious that lowering the temperature from 300 K to 3 K, thermal noise floor will decrease by an order, using higher frequency cantilever. By moving the experiment to a rough vacuum, the Q of the cantilever can increase 100 times. The minimum detectable force can be greatly reduced.

To enhance the detection efficiency of the optical induced force, we can reduce the vibration amplitude of the tip to 1-2 nm, bringing the tip much closer (within 1-2 nm) to the sample.

2.7 Possibility to measure Photon-induced magnetic force

From previous sections, we have already shown that we can measure the electrical dipole dipole force. As described in equation $\left\langle \vec{F}_{opt} \right\rangle = \left\langle \vec{F}_e \right\rangle + \left\langle \vec{F}_m \right\rangle + \left\langle \vec{F}_{e-m} \right\rangle$, we can measure the optical induced magnetic force in the same setup under the condition there are optical magnetic field incident and magnetic field sensitive tip and magnetic field sensitive sample. As we know, the azimuthal beam focal distribution has the in plane electrical field

distribution within the ring structure, and has a high magnetic field at the center of the focal spot[44]. To generate an azimuthal polarized beam, we use ARCoptix radial polarizer[45]. The radial polarizer used the property of twisted nematic liquid crystal cell with proper alignment.

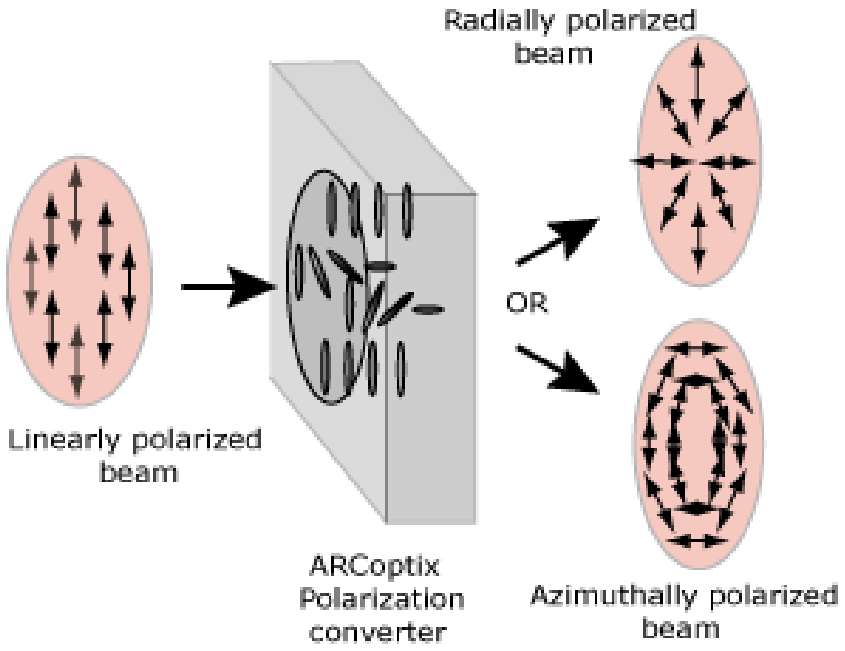

Figure 36 Cartoon of Radial polarizer work schematic

Radially polarized beam or azimuthally polarized beam can be generated using liquid crystal cell as shown in Figure 36.

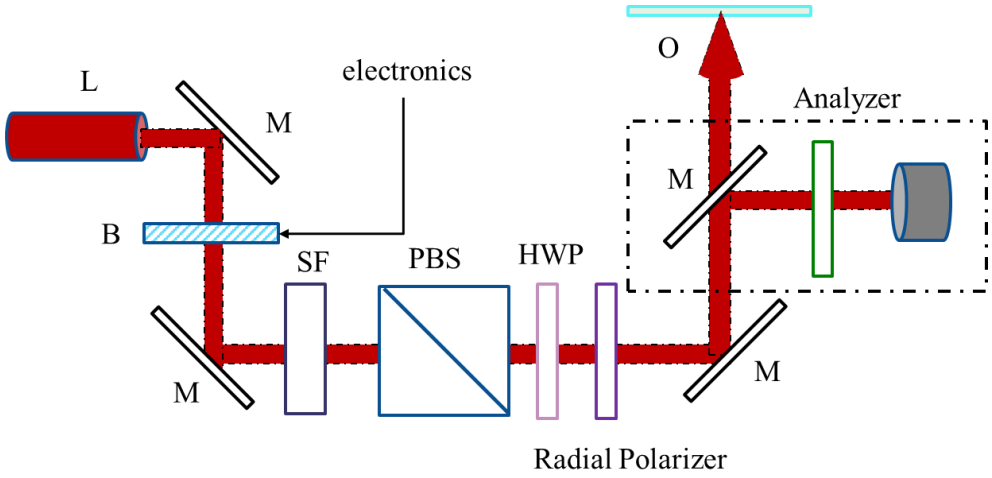

Figure 37 Optical setup of the experiment

As shown in Figure 37, a camera view of the beam with an analyzer is achieved to test the alignment of the radial polarizer. In Figure 37, the dash square shows where we put the analyzer and the camera.

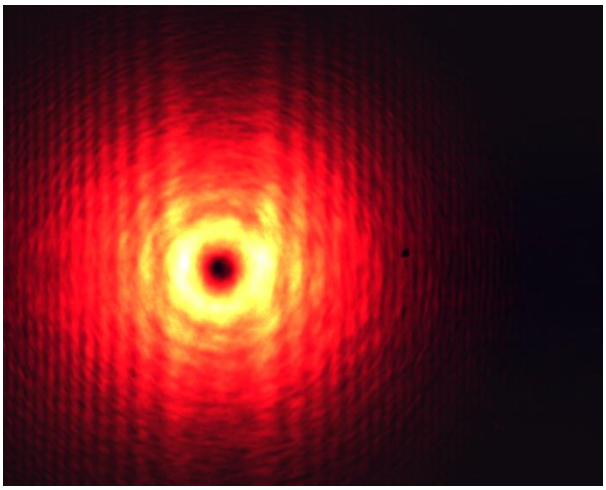

Figure 38 Camera view of the azimuthally polarized beam without focusing

Figure 38 is the camera view without an analyzer. As shown in Figure 38, the intensity profile is a good Laguerre-Gaussian mode without the analyzer. To further test the alignment

of the radial polarizer, putting in the analyzer and rotate the analyzer with angle 0, 22.5, 45, 67.5, 90, 112.5, 135, 157.5 degree.

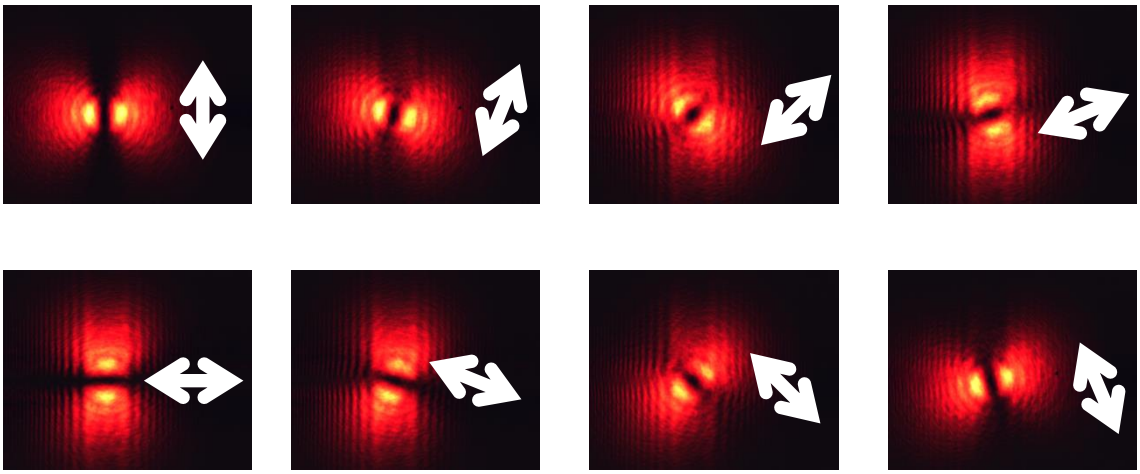

Figure 39 Camera view of input laser with analyzer before azimuthally polarized beam, which analyzer has the rotation of 0, 22.5, 45, 67.5, 90, 112.5, 135, 157.5 degree respectively

With the analyzer, only one direction of the polarization of the light can go through. The azimuthal beam only has the E_ϕ component which intensity has the ring structure, the polarization that orthogonal to the analyzer will be totally block, and generate a symmetric two side pattern. The pattern will rotate as the analyzer rotate. The experiment result is shown in Figure 39, which agreed with theory prediction.

We use the same experiment setup as described previously to measure the electrical field distribution and indirectly, we can calculate the magnetic field distribution.

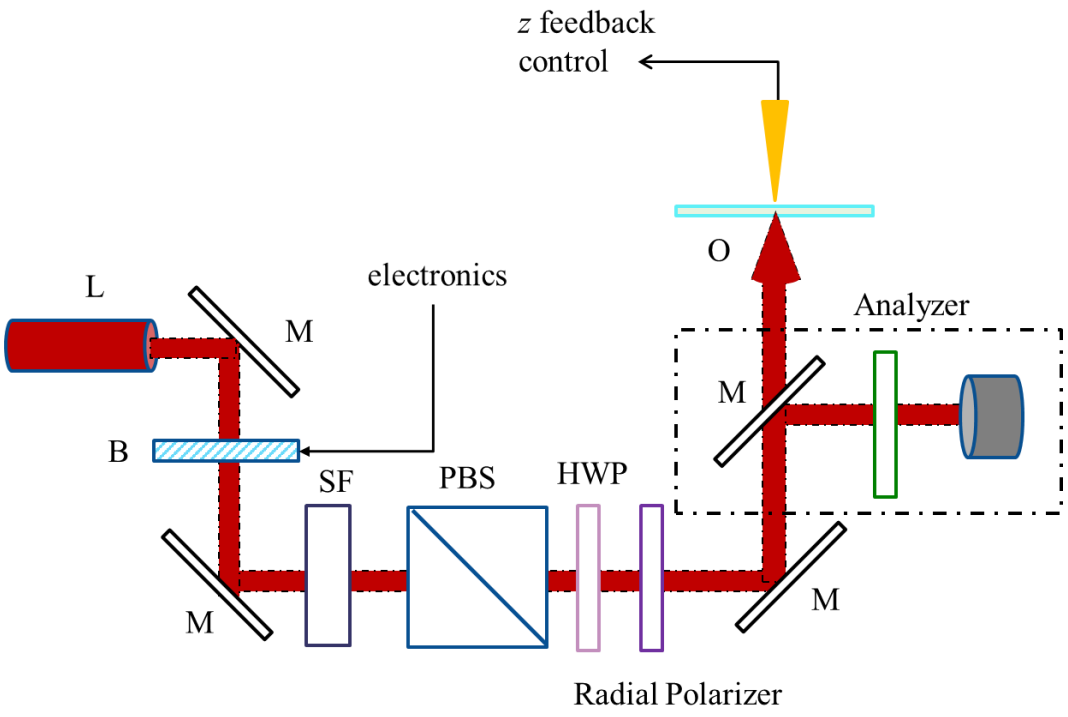

Figure 40 Optical induced force measurement setup

A diode laser of 685 nm was modulated using a Bragg cell modulator at the modulation frequency f_m. To produce a clean Gaussian beam, a spatial filter is used. A polarizing beam splitter (PBS) is used to output the purely linear polarizing beam. Following the PBS is a broadband half wave plate, which change the polarization of linear polarized beam to the correct polarization to align the radial polarizer. The azimuthal polarized beam is tightly focused on the sample using NA=1.45 Olympus 100x oil immersion objective. Experiment setup as Figure 40.

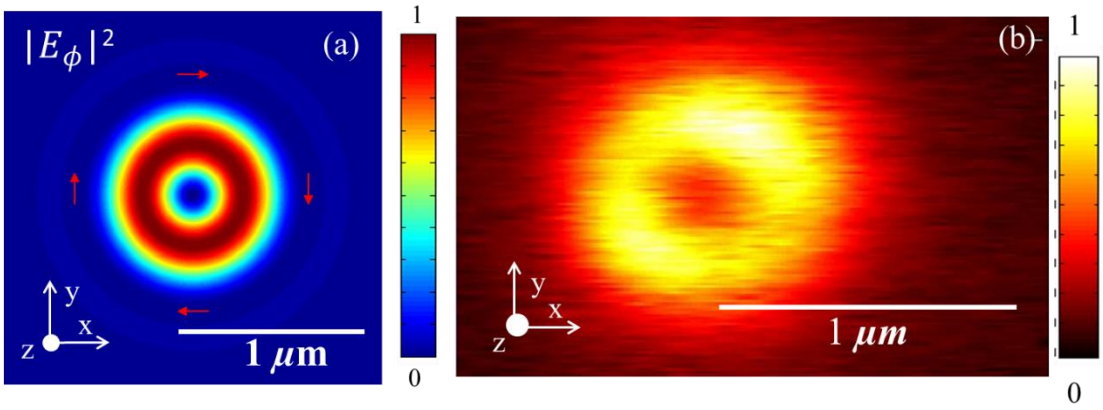

Figure 41 Spatial intensity distributions on glass at 685 nm of E_ϕ (a) Calculation (b) experimental measured force map

The spatial distribution normalized optical force of tightly focused azimuthally polarized light and simulation are shown Figure 41, using this measurement, we can indirectly calculate the magnetic field.

Due to the weak nature of magnetism in materials at optical frequencies, magnetic dipole-dipole interaction forces could be detected by measuring the interaction forces between nanostructures supporting artificial magnetism. In particular, it is well known that nano-spheres composed of dense dielectric materials support the magnetic Mie resonance[38]. In addition, metal nanoparticle clusters with specific geometric arrangements have been used to demonstrate magnetic activity at optical frequencies[46,47]. Therefore, we can measure forces between two magnetic dipoles oscillating at optical frequencies by measuring the interaction forces between two nanostructures supporting artificial magnetism[48]. For example, optical forces between two magnetic dipoles such as two interacting silicon nano-spheres one placed on a substrate and the other attached to the end of an AFM probe could be measured.

2.8 Conclusion

We experimentally demonstrated the application of Atomic Force Microscopy (AFM) based Photo Induced Force Microscopy (PIFM) to map optical near-fields. The spatial resolution is limited only by the AFM probe geometry. We mapped the spatial electric field distributions of tightly focused laser beams with linear, radial and azimuthal polarizations by measuring the optical force between a gold coated AFM probe and its image dipole on a glass substrate. We derived a dipole-dipole theory to model the optical induced force and showed that the experimentally measured data agreed well with our theoretical predictions. We propose that PIFM can be used to characterize optical properties of Nano probes. Finally, we mapped the nanoscale optical interaction force between a gold coated AFM probe and a spherical gold nanoparticle of radius 15 nm. PIFM allows for background free, thermal noise limited mechanical imaging of optical phenomenon over a wide wavelength range from visible to RF with detection sensitivity limited only by AFM performance.

Chapter 3 Lateral optical force detection method

As described in chapter 2, time average optical induced force $\langle \vec{F}_{opt} \rangle$ is a vector has x,y,z three component. In this chapter, we discuss the detection of x component of the optical induced force which perpendicular to the tip axis using torsion mode of cantilever. This method enhance the capability of lateral force AFM to detect lateral optical forces at the nanoscale. We demonstrate the use of PIFM to measure the lateral optical force between a gold coated AFM probe and a nano-aperture in a gold film both illuminated by a focused optical field.

3.1 Introduction

Optical induced lateral force has been used as optical trapping force, optical tweezers. Optical trapping force[49] has been applied to manipulation of viruses and bacteria[50], also it can manipulate neutral particles[51]. The calibration of the optical trapping force is to overcome a known force[52]. Lateral force AFM is a technique that is primarily used to differentiate nanoscale surface properties[53,54]. In lateral force AFM, the frictional forces between the tip and sample creates a torsion of the cantilever which in turn is a function of the surface properties, and leads to chemical force microscopy[55,56].

To measure the lateral component (along *x*-axis) of the total optical force, we used the first torsional resonance of the AFM cantilever as the optical force detector frequency. Tip sample distance is controlled by the first flexural resonance of the tip, which means topography was obtained using the first flexural resonance of the AFM tip. The second flexural resonance was used to detect the longitudinal (*z*-direction) component of the optical force. However, as shown schematically in Figure 15, both the AFM cantilever torsional resonance and tuning fork AFM in shear force mode could be used to detect the *x*-component $\left\langle F_{opt,x} \right\rangle$ of the total time averaged optical force. Also, by simultaneously recording data from both the flexural and torsional modes, the different optical force components can be measured at the same time.

3.2 Resonance mode of FIB AFM tip

Since the measured optical force signal $\boldsymbol{F_x}$ is proportional to the AFM cantilever deflection at a given frequency, the measured optical force is expressed in terms of the cantilever spring constant and quality factor $\boldsymbol{Q}$ for a particular mode as $\boldsymbol{F_i} = \langle F_{opt,i} \rangle Q_m / k_m$, where, *i* = *x*, *z* and *m* corresponds to the second flexural mode for *i* = *z* and to the first torsional mode for *i* = *x*. The measured optical force signal is amplified by the quality factor of the particular mode being detected. In order to increase the detected signal, we need to

reduce the stiffness of the cantilever and increase its Q. The spring constant of the torsional mode is typically very large[57,58]. To improve the lateral sensitivity of the cantilever, the torsional spring constant $k_x$need to be reduced.

To reduce k_x of the cantilever, the hinge size that is 12um along the cantilever length, 10um along the cantilever width, 1/3 of the cantilever thickness has been FIB milled out of the cantilever. Resonance frequencies of the AFM cantilever eigen-modes before FIB milling and after FIB milling at different position of the cantilever are studied by using the structural mechanics module of the commercial finite-element code COMSOL Multiphysics simulation. We use the commercial bare silicon AFM cantilever probes (AppNano Forta) to detect the optical force, since it has good $k_z$to track the surface and measure the Z direction optical induced force. The Comsol simulation has been done using the geometry of AppNano Forta tips, silicon material property is obtained from the AFM vendor.

The first flexural, second flexural, first lateral mode, third flexural, first torsional, forth flexural modes frequencies is shown in Figure 42.

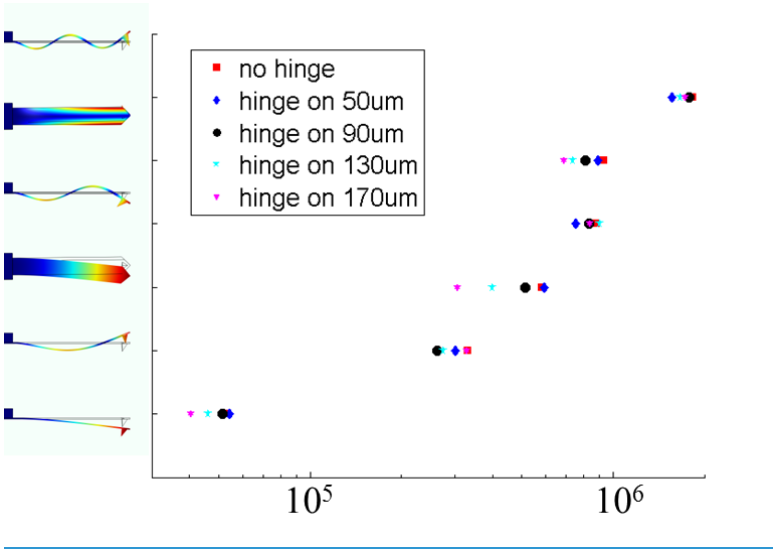

Figure 42 Simulation of resonance frequencies analysis of AFM cantilever without FIB milling and with FIB milling hinge at position 50um, 90um, 130um, 170um using COMSOL Multiphysics

Figure 42 clear shows the FIB milling change the resonance frequency of the cantilever significantly. The first flexural, second flexural, first torsional modes with FIB hinge at 50um, 170um is shown in Figure 43.

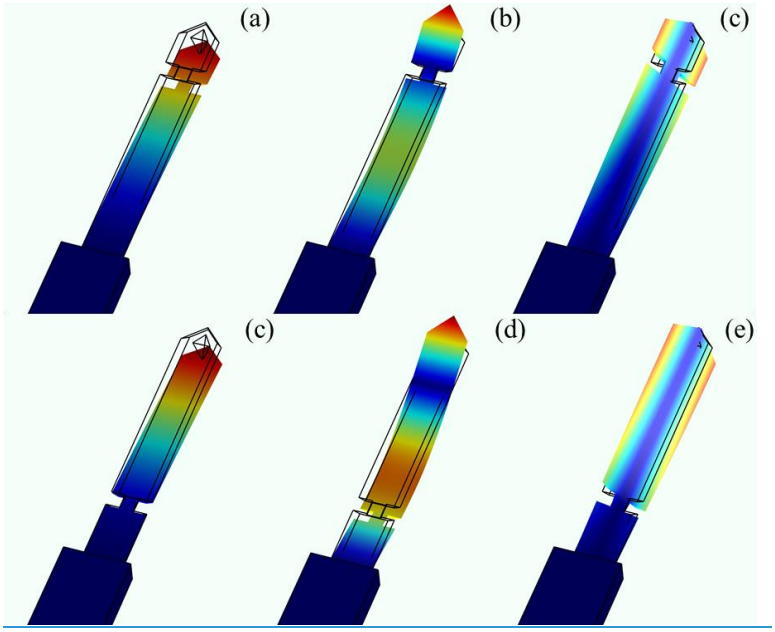

Figure 43 Simulation of eigen-mode of AFM cantilever with FIB hinge at 50um using COMSOL Multiphysics (a) first flexural mode (b) second flexural mode (c) first torsional mode (d)(e)(f) Simulation of eigen-mode of AFM cantilever with FIB milling hinge at 170um (d) first flexural mode (e) second flexural mode (f) first torsional mode

Figure 43 clear shows the FIB milling change the eigen-mode of the cantilever significantly.

To verify the FIB milling hinge effect of the cantilever at different position of the cantilever, simulations and experimental measurement of eigen-modes of the first flexural, second flexural and first torsional cantilever before and after FIB milling have been done. Three positions of the hinge of cantilever at 60um, 130um, 180um have been experimentally

measured and compared with simulation. SEMs of AFM cantilever with FIB milling hinges at 60um, 130 um, 180 um away from the tip.

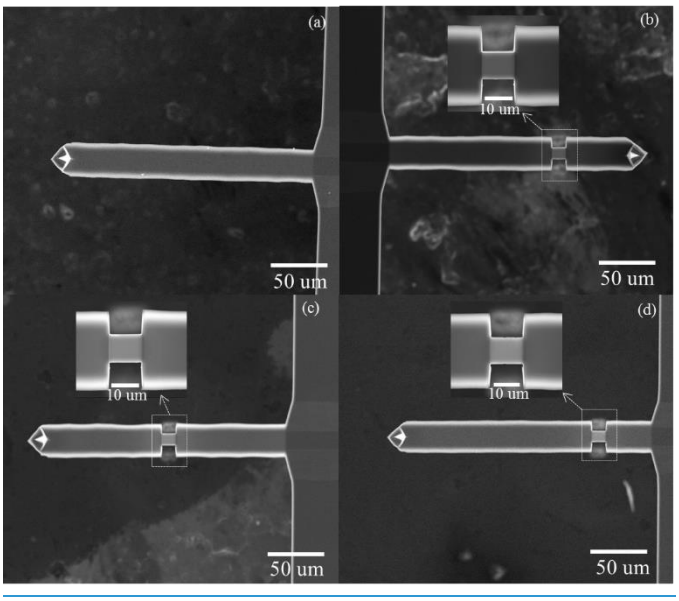

Figure 44 SEM of commercial bare silicon AFM cantilever (b) SEM of AFM cantilever with FIB milling hinges at 60um away from the tip (c) SEM of AFM cantilever with FIB milling hinges at 130 um away from the tip (d) SEM of AFM cantilever with FIB milling hinges at 180 um away from the tip. Insets are the zoomed-in SEM of the hinge.

Comsol structural mechanics simulation of the eigen frequency of the cantilever shows good agreement with the measurement. We can see the resonance frequency before FIB milling and after FIB milling, and the simulation error is within 3%.

As explain previously, we chose to cut the hinge at 180 um away from the tip which reduce the frequency of the torsional mode mostly. The SEM of the AFM cantilever before FIB milling and after FIB milling is shown.

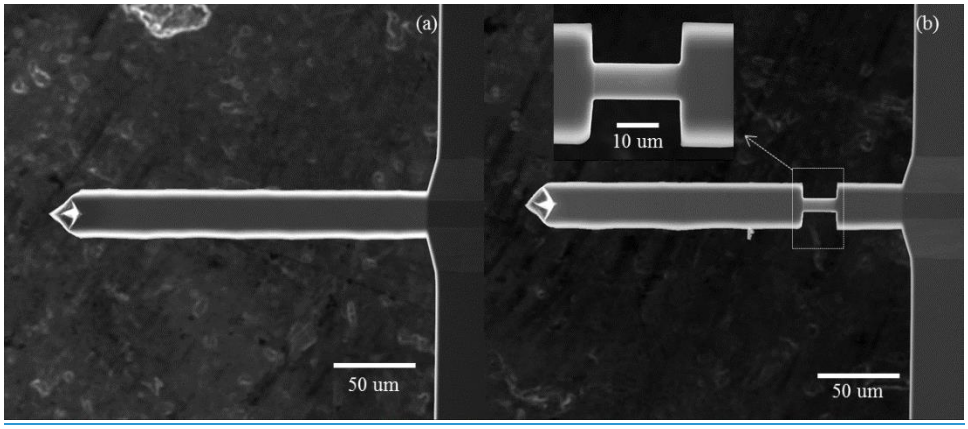

Figure 45 (a) Scanning electron micrograph of AFM cantilever without hinge and (b) scanning electron micrograph of cantilever with hinge with inset showing zoomed-in scanning electron micrograph of the hinge.

3.3 Experimental setup

To detect the optical force, an AFM, optical and electronics elements have been used to build up the experiment setup.

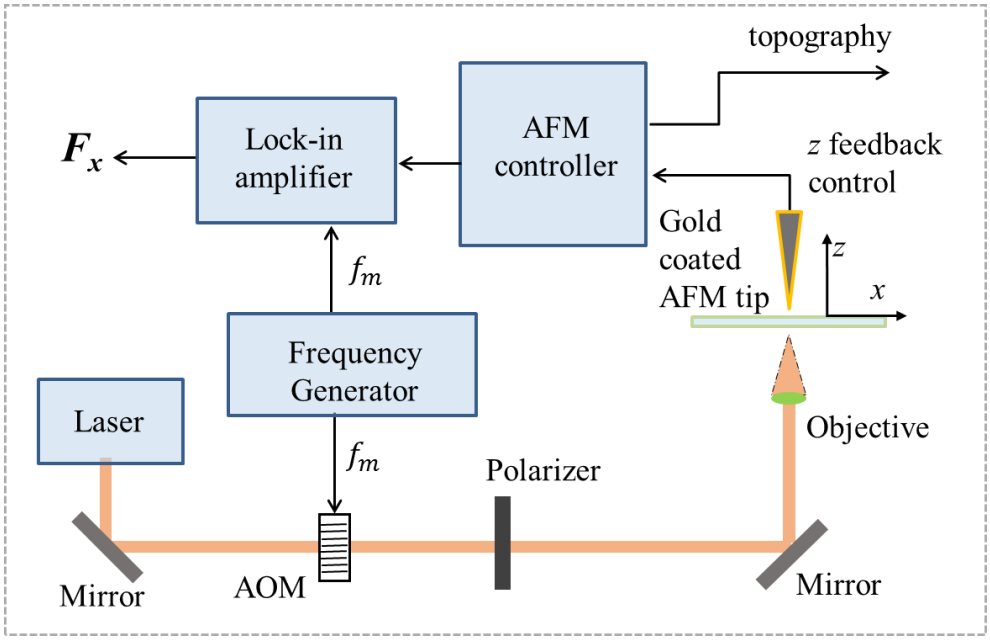

Figure 46 Schematic of experiment setup used to measure the lateral optical force $\boldsymbol{F_x}$

The experiment is built around a commercial AFM operating in the attractive mode and is detailed in Figure 46. The optical beam under measurement is modulated by an Acousto-Optic Modulators (AOM). The modulation frequency f_m was chosen depending on whether the lateral or longitudinal component of the total optical force was under measurement. To measure the lateral component (along *x*-axis) of the total optical force, the optical beam was modulated at the frequency of the first torsional resonance ($f_{0,Tor}$) of the AFM cantilever. To measure the longitudinal (along *z*-axis) component of the total optical force, the optical beam was modulated at the frequency of the second flexure mode ($f_{1,Flex}$) of the AFM cantilever. For the lateral optical force detection, the modulated light was then focused on the sample fabricated on a 0.16 mm thick cleaned glass cover slip using an 20x

`Olympus UPlanSApo with *NA* = 0.75. The modulated optical focal field results in a corresponding modulation of the optical force induced between the AFM probe tip and the sample. The detected optical force is recovered by using a lock-in amplifier with a reference at the modulation frequency. To detect axial optical force, 4-quadrant signal, top-bottom is fed into lock-in amplifier as the signal channel. To detect lateral optical force, 4-quadrant signal, left-right signal is fed into lock-in amplifier as the signal channel. The gold coated AFM cantilever probes were prepared by sputter coating (South Bay technology) commercial bare Silicon AFM cantilever probes (AppNano Forta) with 25 nm gold on a 2 nm chromium adhesion layer.

3.4 Lateral optical force measurement

Two different AFM cantilevers from the same wafer were used to obtain the results presented here. Tip. 1 was used to produce the results in Figure 47 while Tip 2 was used to obtain results in Figure 48. Both the tips had similar values for the resonance frequencies of the first flexural, second flexural and first torsional eigen-modes. Before FIB milling, the measured resonance frequencies of the first flexural, second flexural and first torsional eigen-modes for both tips were =around 58 kHz, 380 kHz and 850 kHz, respectively. After

FIB milling, the measured resonance frequencies of the first flexural, second flexural and first torsional eigen-modes for both tips were around 33 kHz, 187 kHz and 568 kHz, respectively.

To know the FIB processed tip property, the same experiment setup has been used. We measured the longitudinal (along *z*-axis) component of optical force between a gold coated AFM probe and its image dipole on a glass substrate. The longitudinal optical force map of tightly focus laser beams with linear and radial polarizations are shown in Fig 3. The optical beam was modulated at the frequency of the second flexure mode ($f_{1,\mathrm{Flex}}$) of the AFM cantilever. The modulated light was focused on a 0.16 mm thick cleaned glass cover slip using an oil immersion objective (Olympus PlanApo 100x) with NA = 1.45.

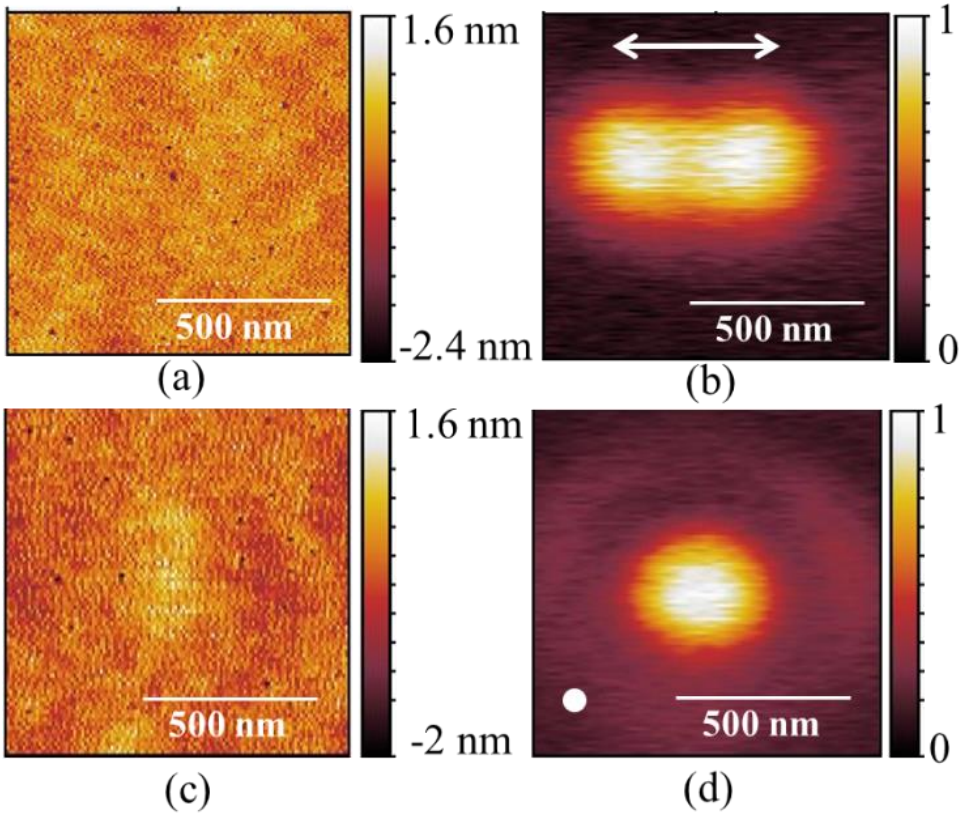

Figure 47 Spatial distributions of (a) topography and (b) normalized longitudinal component of optical image force measured experimentally on clean glass slide at 640 nm with linearly polarized beam, (c) topography and (d) normalized longitudinal component of optical image force measured experimentally on clean glass slide at 640 nm with radially polarized beam

We mapped the optical force distribution between a gold coated AFM probe and single nano-aperture diameter 300 nm, in a 90 nm thick gold film deposited on a 0.16 mm thick clean glass coverslip. The gold film was sputter coated (South Bay technology) on the coverslip with a 2 nm chromium adhesion layer. Nano-apertures of diameter 300 nm were

then prepared by FIB milling the gold film down to the glass ensuring no residual gold was left within the the nano-aperture. The nano-apertures were placed in the focal spot of a focused laser beam with a wavelength of 640 nm. The average power of the laser beam was 300 μW. We mapped the optical force between a gold coated AFM probe and a single nano-aperture of diameter 300 nm for a linearly polarized (along x-direction) laser beam focused on the nano-aperture. Since the laser beam has been focused with 20x Olympus UPlanSApo, the focal spot is purely linear polarization electric fields in the focal plane. The simultaneously recorded topography, normalized lateral optical force and lateral optical force phase are plotted in Figure 48(a) (b) and (c), respectively.

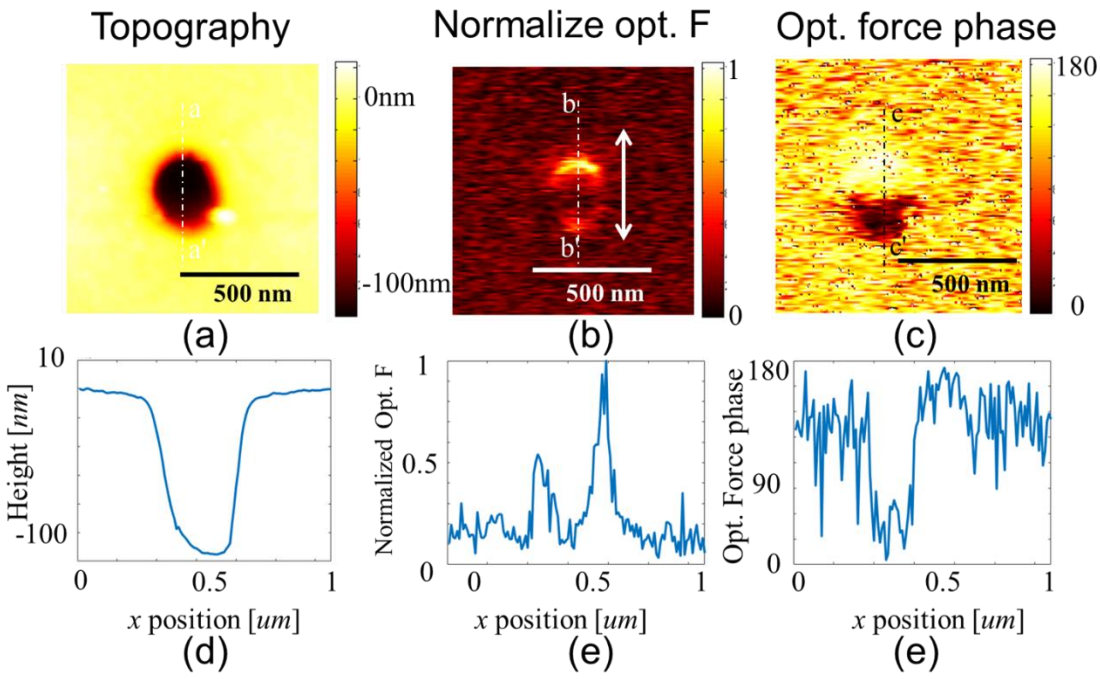

Figure 48 Spatial distributions of (a) topography and (b) normalized lateral optical image force measured experimentally at 640 nm with linearly polarized input light (c) lateral optical image force phase measured simultaneously with lateral optical force.(d) (e)(f) line traces of line a-a', line b-b', of line c-c'.

To understand the spatial distribution of normalized optical force plotted in Figure 48(b) we computed the electric field distribution around a single nano-aperture of diameter 300 nm in a 90 nm thick gold film with two linearly polarized plane wave at angle 20 degree input using the Lumerical FDTD solutions. The edges of the nano-apertures were filleted with a radius of curvature 5 nm. The optical constants of gold and silicon used in all calculations in the work were obtained from the published reference[42]. A cross-section of

spatial distribution of the normalized lateral (*x*-directed) electric field component around a single nano-aperture is plotted.

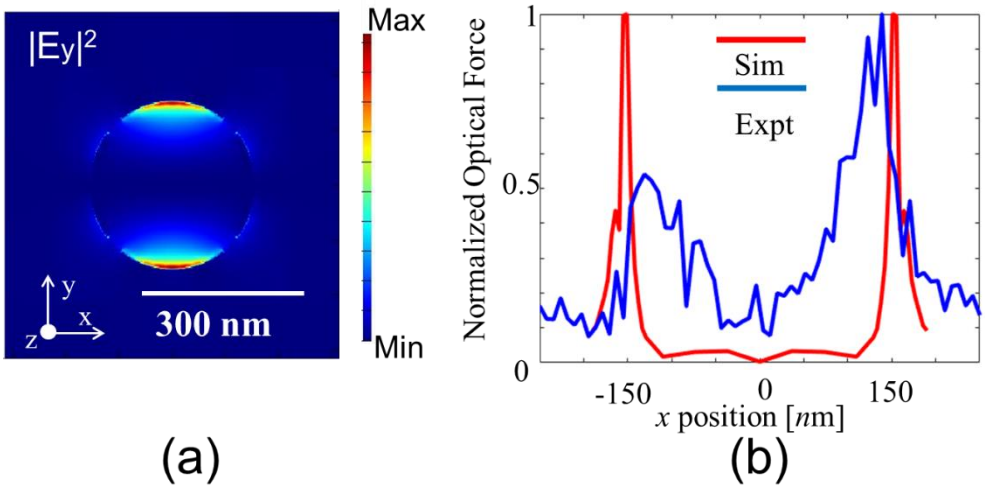

Figure 49 Numerical calculations of normalized lateral (y-direction) electric fields around a single nano-aperture of diameter 300 nm in 90 nm thick gold film. (b) Comparison of line traces of normalized optical force obtained experimentally (line a-a' in Figure 48(b))

As shown Figure 49(a), we observe a strong field enhancement near the edges of the nano-aperture indicating that the edges will have the strongest interaction with the apex of the gold coated AFM tip due to lateral optical force. We performed further Lumerical FDTD simulations of gold coated tip modeled as an 40nm Au sphere interacting with the nano-aperture and compared the line trace of lateral optical force obtained experimentally with the simulations in Figure 49(b). The results of the simulations are in general agreement with experiment. The slightly broadened experimental data can be explained by considering the

shape of the AFM probe. From Figure 48 , the lateral optical phase image clearly show the direction of lateral optical force change 180 degrees, agrees well with theoretical prediction. Further optimization of the AFM cantilever to enhance the sensitivity of the torsional mode will help improve the signal to noise ratio.

3.5 Simultaneous detection of lateral and longitudinal optical forces

This technique can be extended for simultaneous detection of lateral and longitudinal optical forces. To achieve this, the AFM cantilever will be used as a multi-channel nanoscale force detector with each detection channel corresponding to a different eigen-mode of the cantilever.

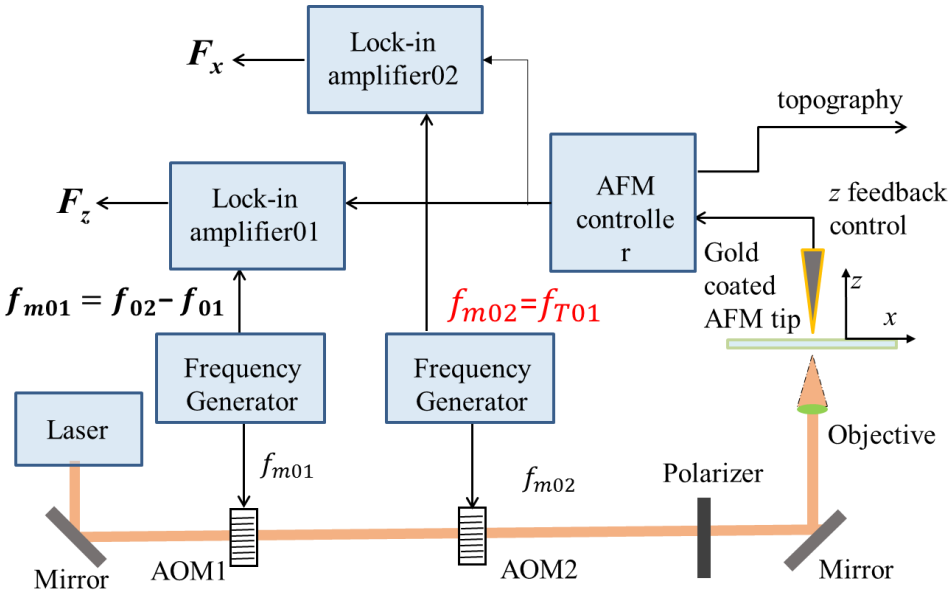

Figure 50 Schematic of experiment setup simultaneous detection of lateral and longitudinal optical force

As shown in Figure 50, by modulating the incident laser beam at two frequencies f_{m01} (second flexure resonance) and f_{m02} (first torsional resonance) using two acousto-optic modulators, the cantilever will respond to these modulated fields at its respective resonant frequencies (second flexure and first torsional) leading to simultaneous detection of both longitudinal and lateral optical forces. By using the AFM cantilever as a multi-channel detector to measure optical forces along different directions simultaneously, this technique can be generalized to measure the tensorial components of molecular resonances. We note that the technique is completely general and can be implemented using both cantilever and tuning fork based AFM's.

3.6 Conclusion

In this chapter, we have demonstrated the detection of lateral optical forces using the PIFM technique. We used the torsional eigen modes of a cantilever to measure the lateral optical force distribution between a gold coated AFM probe and a nano-aperture of 300 nm diameter in a gold film of thickness 90 nm. The resonance frequency of the torsional eigen-mode of the AFM cantilever was optimized by engineering the cantilever shape using a focused ion beam. The measured lateral optical force distribution agreed well with our simulations.

Chapter 4 Tip fabrication process

AFM tips played an important role on the AFM commercialization. After silicon tip fabrication process can be commercially implemented, and wafers of AFM tips are available, AFM have been fast industrialization. Now there are a lot of different type of AFM available in the market, different tip material, different tip coating material, different tip shape, etc. We can choose the tips that fits application. AFM different application usually require different AFM tips. Such as KPFM need a conductive layer on the AFM tips. MFM need magnetic material coated tips, usually CO coated, so the AFM tips can have magnetic responds.

To detect optical induced force, the metal coated tip that has the important effect on the force level. In this chapter, we will show the tip fabrication that for the optical induced force and simulation of different coating material effect on the force signal. Also, we will show a new fabrication method to have stable optical properties, a control method to attach nano particle to the end of the tip.

4.1 Introduction

For all the tip involved experiment, tips always play an important role on the experimental result. For the regular AFM experiment, the tip radius determine the lateral resolution. For the magnetic force microscopy, magnetic field generated by the magnetic tip will change the sample's magnetization, which is a nonlinear tip sample interaction[59]. The

magnetic tip and sample interaction gives a difficulty to interpret the image. The magnetic moment of the AFM tip generate the magnetic field, the ideal tip is attach a small single domain ferromagnetic particle at the end of nonmagnetic cantilever, it is very hard to fabricate. For tip enhanced raman experiments, the tip is the key component. In tip enhanced raman experiment, the tip enhanced raman signal depends on the fourth power of the electric field enhancement factor[60], the end of the tip interact with the sample gives the electric field enhancement factor. AFM tip is a key component of our measurement setup. Since AFM tips are so important for the experiment, a lot of effort have been put into tip fabrication, and different methods have been developed.

Among the tip involved experiment, many instruments use a wire as the tip such scanning tunneling microscopy (STM), tuning fork. The solid material wires are usually sharpen using the method of electrochemical etching[61]. This method of preparing gold, silver tips is claim to have precise control of the end of the tip and have reliable reproducibility.

When cantilever based AFM is used in the tip involved experiment, the metal coated cantilevers are usually used to get the field enhancement factor. Silver or gold is thermally evaporated to the commercial silicon tip. This method need to have a precise control of the evaporation rate [62].

To have the AFM tips have sharper plasmon resonance, effort has been done to grow a nano particle at the end of the tip on silicon dioxide. The thickness of the silicon dioxide can tune the resonance wavelength[63]. The commercial silicon tips are put in furnace with desirable time to oxidize the silicon to achieve the design thickness of the silicon dioxide.

Metal has been thermally evaporated to the end of the tip to grow a nano particle at the end of the tip[64]. This method require precise control of the furnace and the evaporator parameter.

Chemically grown the particle also can be done[65]. TiO2-coated cantilever is immersed in the aqueous solution of tetrachloroauric acid (HAuCl4), ultraviolet light is confined only to illuminate the end of the tip, gold deposited onto the surface of the TiO2 film. This method needs a tightly control of the illumination area, cannot have nano meter precision.

Attaching the nano particle at the end of the fiber by glue have been developed[66]. Fiber tip is immersed in polyethylenimine solution then using AFM to attach the particle to the end of fiber tip.

Dielectrophoresis (DEP) forces is used to attract nano particle to the cantilever[67]. An AFM probes is dipped in desired particle solution. Applied non-uniform electric field, DEP force will attract the particle to the probe. This method is difficult to control to have only one isolated particle at the end of the AFM probe.

Nanoparticle can be chemically attach to the end of the AFM tip[68]. Since the cantilever is silicon, the chemical will be one branch is reactive with silicon, one branch is reactive with gold to attach the gold nano particle to the end of the tip. This method also need to have more chemistry to only make the end of the tip to react with gold to get one isolate particle at the end of the tip.

4.2 Gold Coated tip

As for our AFM bandwidth limitation, we choose commercial bare Silicon AFM cantilever probes (AppNano Forta $\mathbf{k}$ = 1.6 N/m, $f_0 \sim 65$ kHz) for our experiment. This type of

Silicon tip tracts the regular surface (glass, template strip gold, au nano particle) well, not easily overshoot into the surface as the AFM approach to the surface. Also the second flexure mode frequency in the detectable range of the electronics of the AFM. To get the electromagnetic enhancement of the optical field intensity, we use the gold coated commercial bare Silicon AFM cantilever probes since it is easy fabricate compared to other tip fabrication method. The AFM cantilever probes were sputter coated (South Bay technology) with 2 nm chromium adhesion layer, then 25 nm gold. To have more uniform film of the tip, AFM tips are sputtered with rotation around AFM tip end.

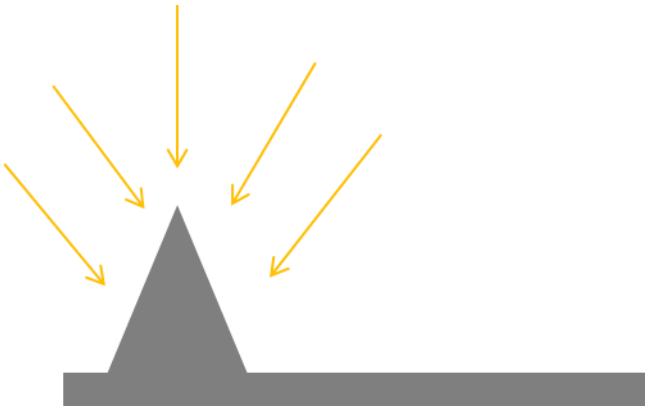

Figure 51 Cartoon of sputter coat AFM tip

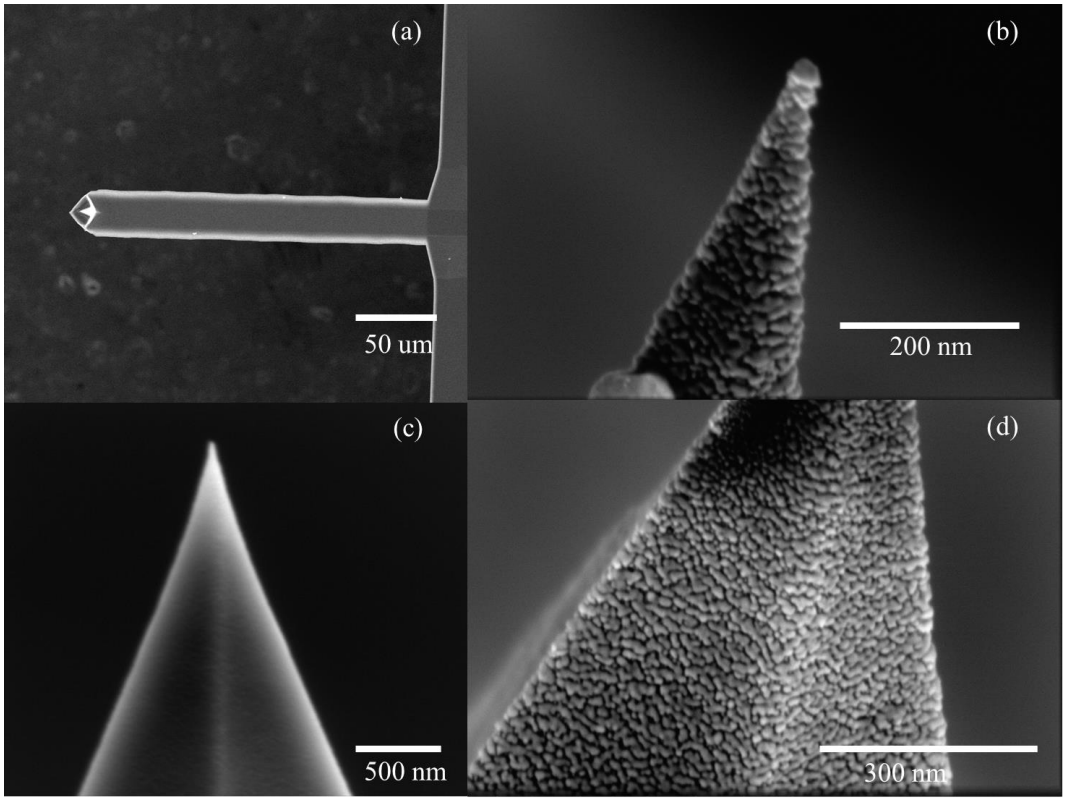

Figure 52 SEM of commercial bare silicon AFM cantilever (b) Zoomed-in SEM of AFM tip (c) SEM of AFM tip side view (d) Zoomed-in SEM of AFM tip side wall

As shown in Figure 52, there are small gold grain continued covered on the silicon tip. The end of the tip has a small gold grain which affect electric field enhancement at the gap of the AFM tip and the substrate. Different sputtering gun condition gives different electric field enhancement factor, since the small gold grain at the end of the tip change, as described in chapter 2.

4.3 Au nano particle attached tip

Since the small gold grain at the end of the tip depends mainly on the sputter condition, the AFM tip performances have large variation. New fabrication method to have stable optical properties need to be investigate. To have more control on the tip end shape, and improve the force signal, we attach a gold nano particle at the end of the commercial tip. We use the effect that gold-gold can form metallic bonds by applying pressure[69] to attach au particle to the silicon tip.

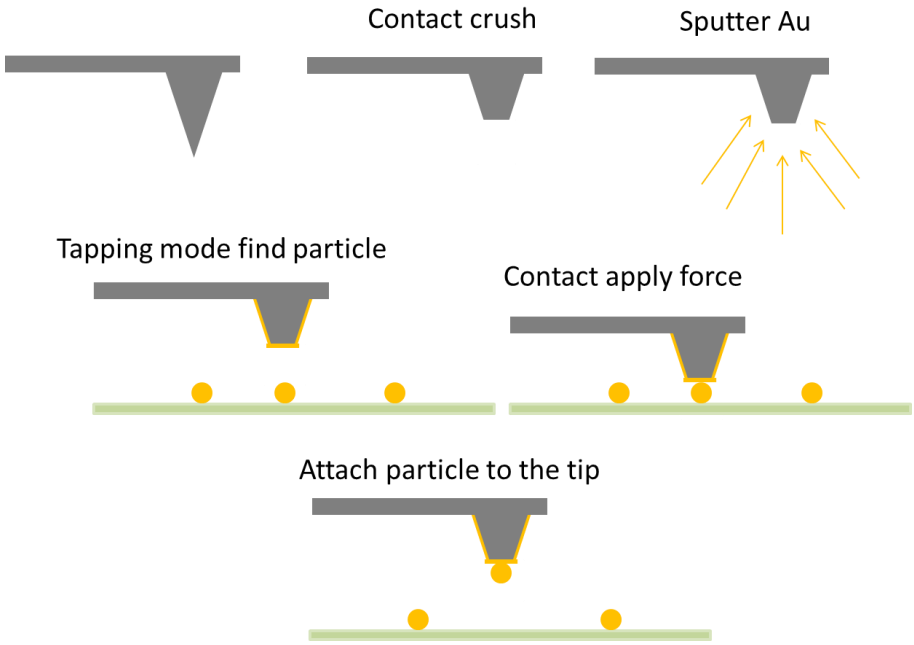

Figure 53 Fabrication steps for attach Au particle to the tip

As shown in Figure 53, there are several steps to attach the au particle to the silicon tip. First, we use the contact mode AFM to apply pressure to AFM tips toward the clean glass cover slip to make the flat area on the AFM tips. This method is control method since the pressure is precise controlled by the AFM feedback system, which control the flat size of the

end of the tip. Since it is only contact engage without any scanning, it is less contaminate the tip compared to grinding the tip on the substrate. Since we want to attach 30nm diameter au particle, the flat size is around 30nm, 3nN has been applied to the end of the tip. Second, the flattened tip is put into the chamber and have 10 nm thickness au and 2nm Cr coated on the tip. Mono dispersed 30nm au particle on glass has been made, the AFM scan with a silicon tip is shown in

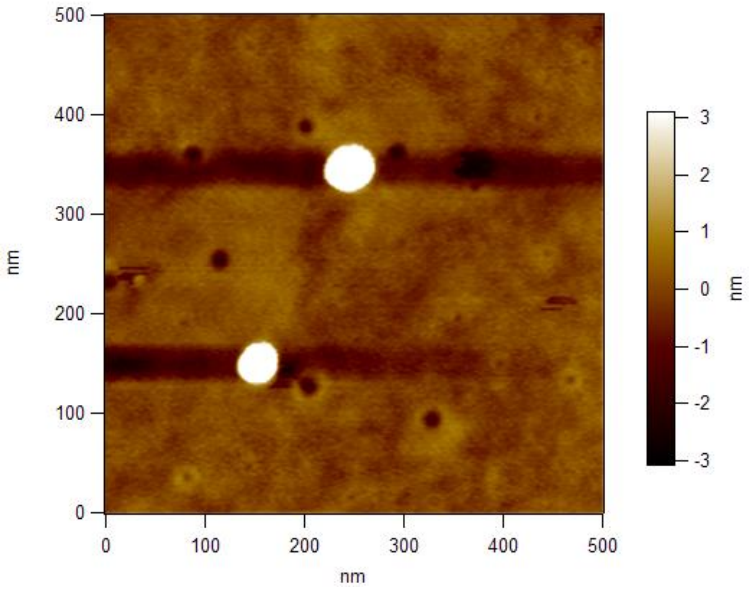

Figure 54 AFM scan of mono disperse 30nm Au particle

The flattened tip scans over a mono dispersed 30nm au particle on glass using tapping mode to locate the particle position. Thirdly, we change the mode to contact mode to apply pressure to the particle. Since the au particle is dropcast on the glass surface with blow dry, au particle can be moved. If the particle have been applied large pressure force, the particle would be moved. If the particle have been applied small pressure force, the particle would not be attached to the end of the tip. For the tip that we use in the experiment (AppNano Forta **k** = 1 N/m), 2-3nN is reliable attach the au particle to the end of the tip. The successful

rate is more than 80%. The Au particle attached to the end of the tip is stable more than a week when store in the atmosphere.

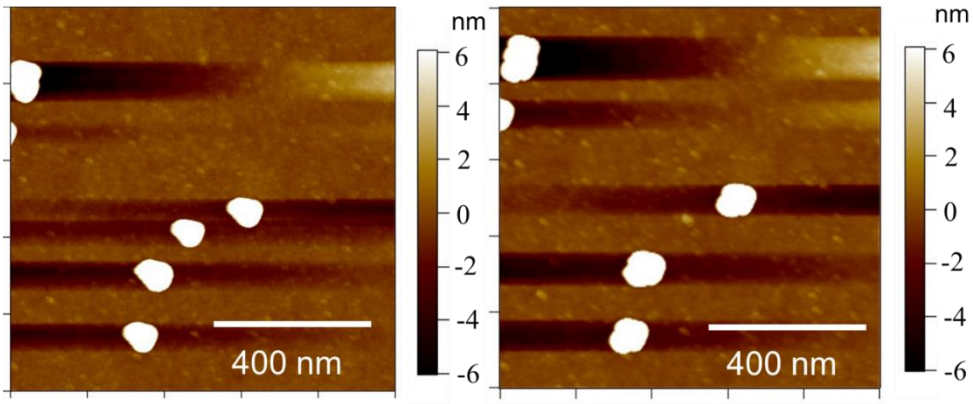

Figure 55 (a) AFM scan topography before au particle pickup (b) AFM scan topography of same area after au particle pickup.

To verify the au nano particle is attached onto the end of the tip, AFM topography at the same area is scanned and shown as Figure 55. Before the AFM tip picked up the au particle, the sphere nano particle topography appears triangle. The reason is that the nano particle topography is the nano sphere convolve with the tip end which has flatten area that is triangle. After the nano particle attached to the end of the tip, the scan topography has a particle missing compare to before pick up the particle. The shape of the particle change to sphere. Scanning electron microscopy (SEM) image of nano particle attached to the end of the tip is shown in Figure 56.

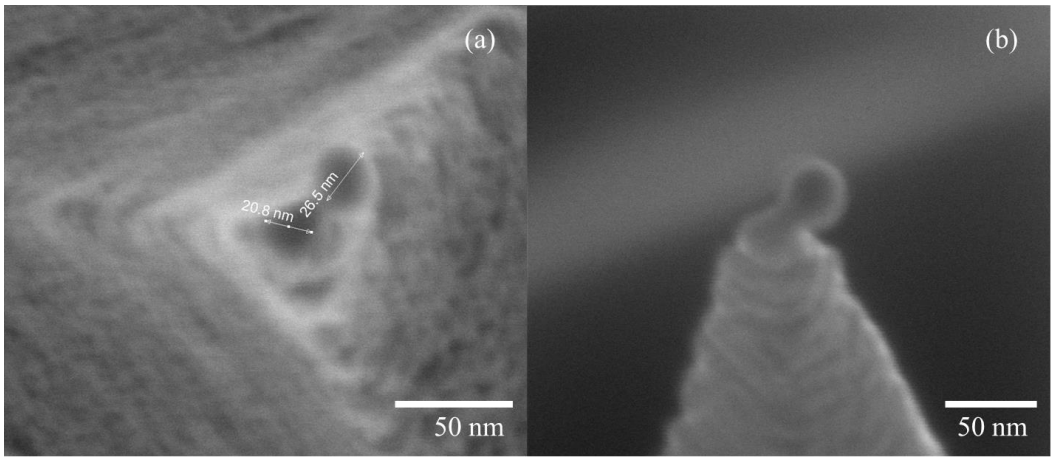

Figure 56 SEM image of nano particle attached to the end of the tip (a) top view (b) side view

The tip that was attached with 30 nm au particle was used to scan the tightly focal field distribution using experimental setup as Figure 16 with wavelength 510nm, input power 25uW, Spatial distributions of normalized optical induced force map of the focal spot is shown in Figure 57.

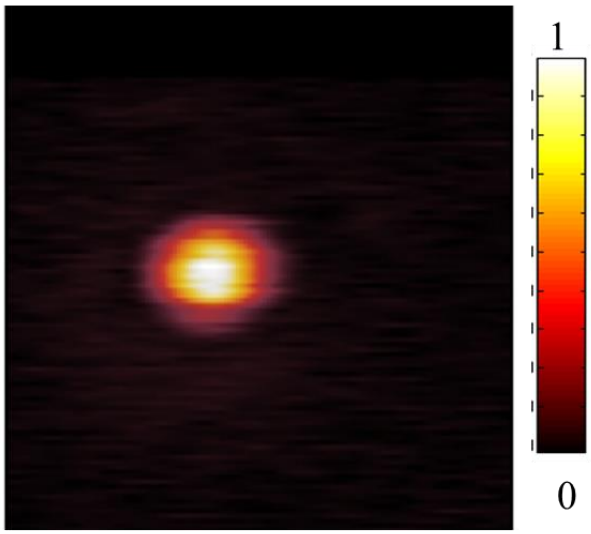

Figure 57 Spatial distributions of normalized optical induced force of tightly focused beam at 510nm with radial polarization

As shown in Figure 57, the normalized optical induced force has signal to noise ratio of 42, which means the particle at the end of the tip enhanced the local electrical field.

Same fabrication process can attach an Au nano rod to the tip end. SEM image of nano rod particle attached to the end of the tip is shown in Figure 58.

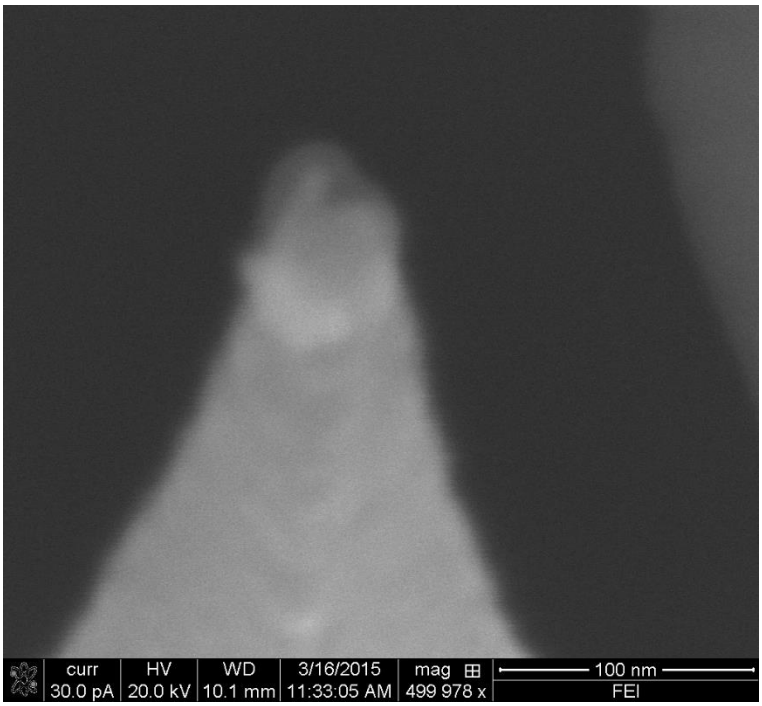

Figure 58 SEM image of Au nano rod attached to the end of the tip

The tip that was attached with 30 nm au particle and the tip that was attached with Au nano rod short axis 40nm, long axis 60nm were used to scan the tightly focal field distribution using experimental setup as Figure 16 with wavelength 510nm, input power 25uW, Spatial distributions of normalized optical induced force map of the focal spot is shown in Figure 59.

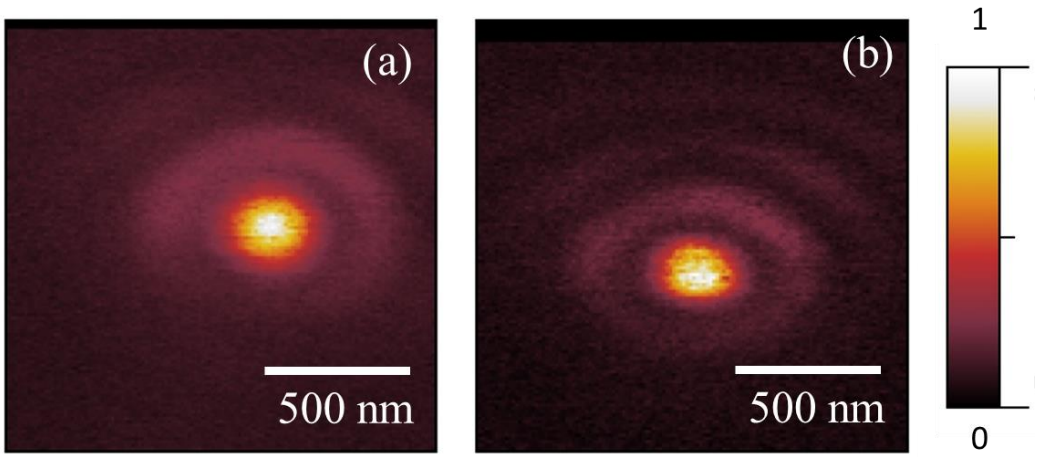

Figure 59 Spatial distributions of normalized optical induced force of tightly focused beam at 510nm with radial polarization, (a) with 30 nm au sphere attached at the end of the tip(b)with Au nano rod short axis 40nm, long axis 60nm attached at the end of the tip

As shown in Figure 59, the optical induced force map Figure 59(b) obtained by the nano rod attached to the end of the tip does not have a significant change of the optical induced force map Figure 59(a)obtained by the nano sphere attached to the end of the tip. The reason is the au rod attached to the end of the tip has an angle as show in the Figure 58 SEM.

4.4 Si nano particle attached tip

Attaching nano particle with other material other than Au will broaden the application of this attaching mechanism. There are several steps to attach the Si particle to the silicon tip.

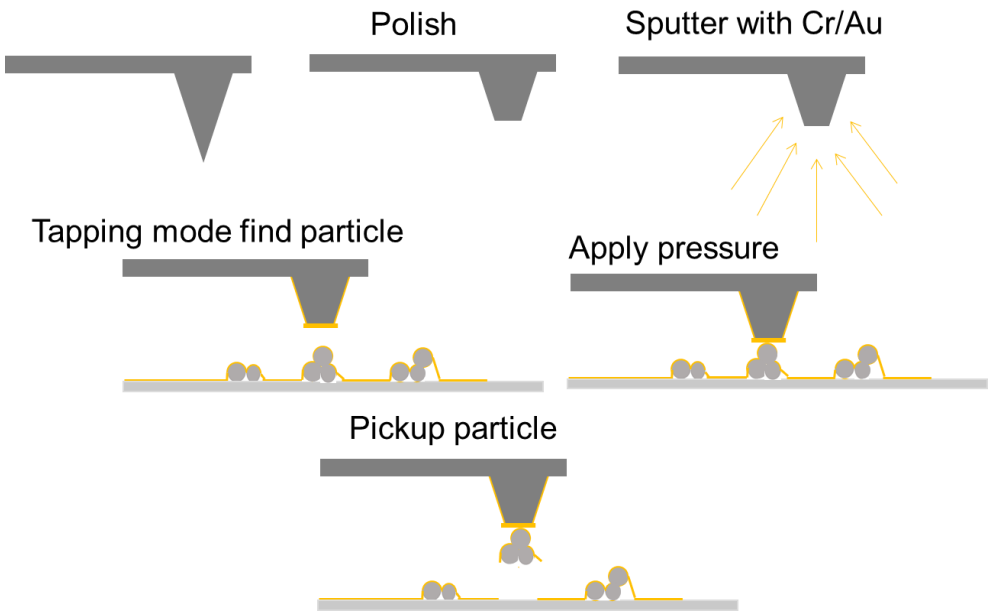

Figure 60 Fabrication steps for attach Si particle to the tip

As shown in Figure 60, first, we use the contact mode AFM to apply pressure to AFM tips toward the clean glass cover slip to make the flat area on the AFM tips. This method is control method since the pressure is precise controlled by the AFM feedback system, which control the flat size of the end of the tip. Since it is only contact engage without any scanning, it is less contaminate the tip compared to grinding the tip on the substrate. Then we disperse of Silicon nano particle on substrate coated with 10nm of au. Third, the flattened tip is put into the chamber and have 10 nm thickness au and 2nm Cr coated on the tip. The flattened tip scans over silicon particle on glass using tapping mode to locate the particle position. Then, we change the mode to contact mode to apply pressure to the particle. Scanning electron microscopy (SEM) image of nano particle attached to the end of the tip is shown in.

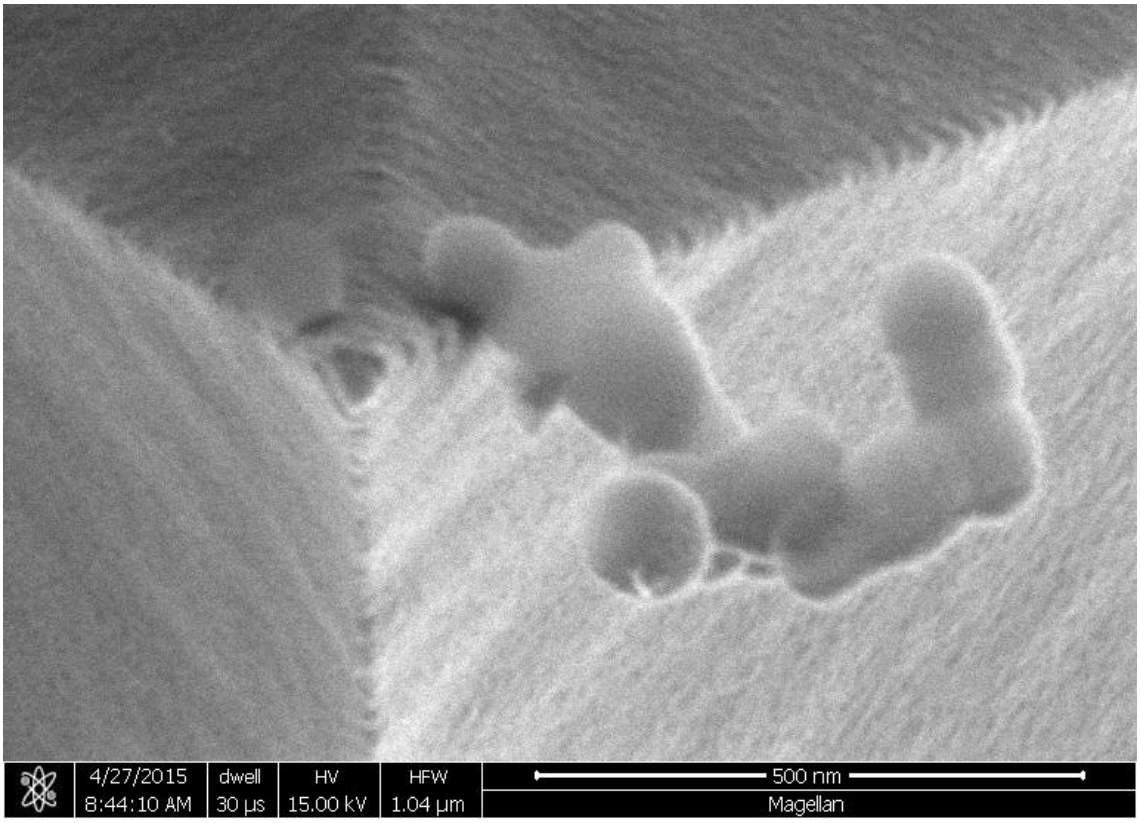

Figure 61 SEM image of nano particle attached to the end of the tip (a) top view (b) side view

We cannot attach single silicon to the end of the tip is because it is difficult to make a mono disperse Si nano particle on substrate. That is also the reason that it is not attach at the very end of the tip since the blunt tip is not applying the pressure at the correct position.

4.5 Conclusion

In this chapter, we show the tip fabrication process which used to measure the optical induced force. With the coating method we used, the tips gives high axial electric field enhancement. We also show a new fabrication method to have stable optical properties. We used gold material property, without any chemical reaction, reliably attach the particle to

the end of the tip. This method can applied to any size or shape of the nano particle. More research need to be done to make sure the particle is attached at the center of the flat surface of the tip. The particle is attached to the center of the tip will give more signal enhancement control and less tip convolve effect while scanning. This method can also applied to attach other material particle such as Si particle. The AFM tip with au particle will have a widely application.

Chapter 5 Conclusion and future work

5.1 Conclusion

In conclusion, we experimentally demonstrated the application of Atomic Force Microscopy (AFM) based Photo Induced Force Microscopy (PIFM) to map optical near-fields include axial axis (along tip axis) optical induced force and lateral (perpendicular to tip axis). The spatial resolution is limited only by the AFM probe geometry.

We mapped the spatial electric field distributions of tightly focused laser beams with linear, radial and azimuthal polarizations by measuring the optical force between a gold coated AFM probe and its image dipole on a glass substrate.

We derived a dipole-dipole theory to model the image force and showed that the experimentally measured data agreed well with our theoretical predictions.

We propose that PIFM can be used to characterize optical properties of Nano probes. We mapped the nanoscale optical interaction force between a gold coated AFM probe and a spherical gold nanoparticle of radius 15 nm.

We demonstrated the detection of lateral optical forces using the PIFM technique. We used the torsional eigen modes of a cantilever to measure the lateral optical force distribution between a gold coated AFM probe and a nano-aperture of 300 nm diameter in a gold film of thickness 90 nm.

We have optimized the resonance frequency of the torsional eigen-mode of the AFM cantilever by engineering the cantilever shape using a focused ion beam. The measured lateral optical force distribution agreed well with our simulations.

We use the AFM tip as a multi-channel nanoscale force detector with each detection channel corresponding to a different eigen-mode of the cantilever, propose a scheme to simultaneous detection of lateral and longitudinal optical forces.

We show the tip fabrication process which used to measure the optical induced force. With the coating method we used, the tips gives high axial electric field enhancement.

We also show a new fabrication method to have stable optical properties. We used gold material property, without any chemical reaction, reliably attach the particle to the end of the tip. This method can applied to any size or shape of the nano particle. This method can also applied to attach other material particle such as Si particle. The AFM tip with au particle will have a widely application.

5.2 Future work

5.2.1 Single molecule detection

Since PIFM has shown the ability to measure the absorption peak with 5nm spatial resolution. By improving the signal to noise ratio, the system should be able to detect single molecule absorption or Raman force. Since single molecule fluorescence has been detected before using NSOM [70,71], we can use the fluorescence signal as indicator for the molecule status. To detect the fluorescence, we modify our setup, add detection optics on the back reflection path shown as in Figure 62.

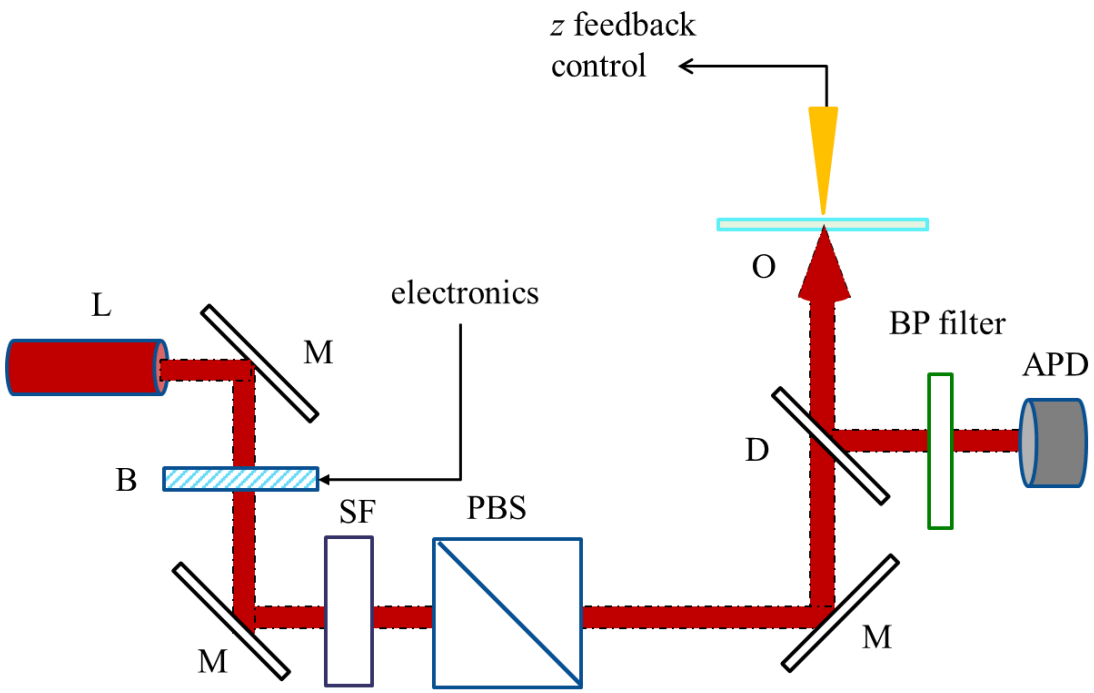

Figure 62 Schematic for detect single molecule florescence

A Bragg cell modulator was used to modulate the desired wavelength laser which generate the optical field under measurement at the modulation frequency $f_{m.}$ A spatial filter is to make the beam spatially central Gaussian mode. The laser focused on the sample by using an oil immersion objective (PlanApo 100x) with *NA* = 1.45 on an inverted microscope (Olympus IX71) in transmission mode. The back reflected light is filter by the proper dichroic and bandpass filter, fluorescence is detected by the APD.

We use Bodipy-TMR (Thermo fisherBODIPY® TMR-X NHS Ester) as sample dye, to make mono disperse molecule, Bodipy-TMR dissolved in methanol with concentration of 0.8nM, has been dropcast on the PMMA film or buried in the PMMA film. With Bodipy-TMR we use the excitation at 542 nm. The florescence has been achieved shown in Figure 63.

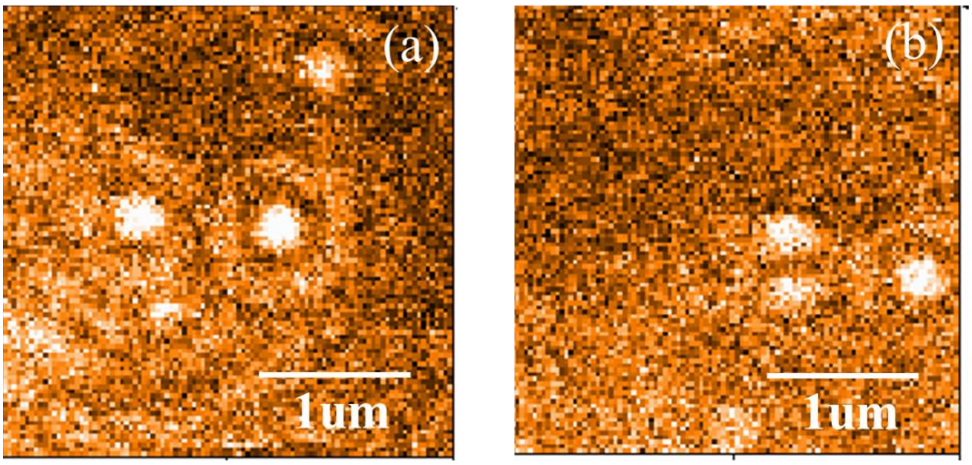

Figure 63 Different area of the single molecule florescence

As describe in previous chapter, optical induced force has d^{-4} dependence with tip sample distance, to control the tip sample distance, PMMA film[72] with 2nm thickness has been made. We use molecule weight of 15000, dissolve in toluene with concentration 0.1% (weight percent), spin coat the solution on glass with 4000 rpm, 2 nm PMMA film has been made. AF M scan is shown in Figure 64.

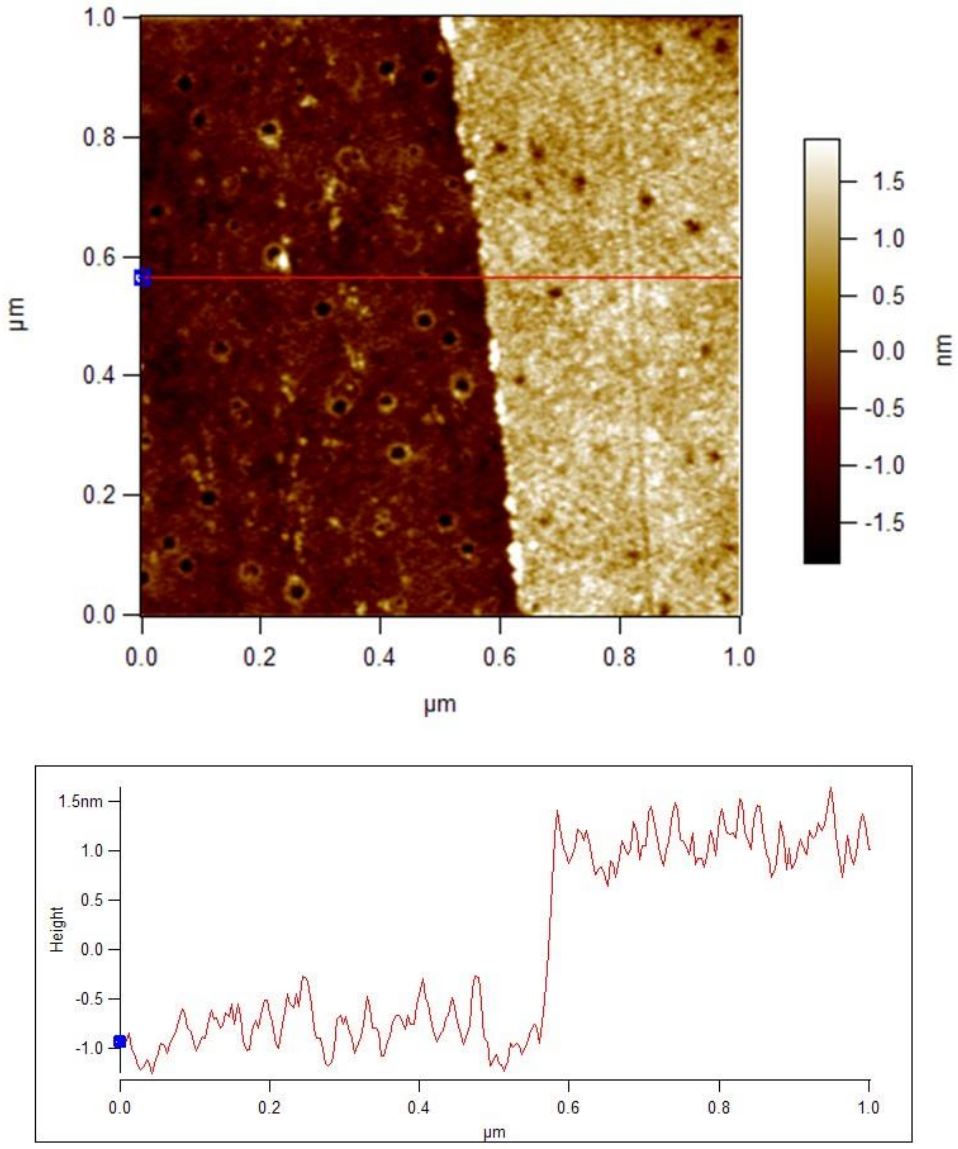

Figure 64 AFM scan of 2 nm PMMA

Using the experimental setup and the sample we can measure florescence at the same time measure optical induced force from the absorption of the molecule.

5.2.2 Optical induced magnetic force

As describe in previous chapter, we have a measure the tightly focused focal spot of azimuthally polarized light. At the center of the focal spot, there are optical magnetic field

enhancement. With the method that using the gold-gold can form metallic bonds, we ca attach silicon nano partical to the end of the tip which have a magnetic resonance at visible wavelength. We can use the same schematic that we measure the optical induced electrical dipole force to measure the optical induced magnetic dipole force.

In conclusion, PIFM allows for background free, thermal noise limited mechanical imaging of optical phenomenon over a wide wavelength range from visible to RF with detection sensitivity limited only by AFM performance. With low noise, high spatial resolution, PIFM will have widely application in chemistry, material science and biology.

APPENDIX Matlab code for calculation focal distribution of the tightly focus beam

Glass information function

```
%data file for focal fields
%refractive index of BK7 glass used in cover slip
n_objective=1.513;
%refractive index of air
n_air=1;
%refractive index of gold
% n_gold=0.18582+1i*3.1118;
n_gold=n_air;
% focal length of objective in meters
f=3.5e-3;
% NA - numerical aperture of objective
NA =1.45; %oil immersion lens
%NA angle in glass
theta_NA_objective = asin(NA/n_objective);
% critical angle for total internal reflection from objective to air
theta_critical_angle_objective = asin(n_air/n_objective);
% wavelength in meters
lamda=660e-9;
% wave number in free space
```

```
k=2*pi/lamda; %units of inverse micrometers
%k in medium BK7
k_objective=k*n_objective;
%k in air
k_air=k*n_air;
```

Linear focus calculation

```
clear all
focal_field_glass_data
Nx=201;
Ny=201;
Nz=1;
loopx=1;
loopy=1;
x_val = linspace(-1e-6,1e-6, Nx);
y_val = linspace(-1e-6,1e-6, Ny);
z_val= [0];
thetamin=0;
thetamax=theta_NA_objective;
for loopz=1:Nz
   z=z_val(Nz);
for loopx=1:Nx
   x=x_val(loopx);
```

```
   for loopy=1:Ny
      y=y_val(loopy);
      r_p=sqrt(x.^2+y.^2+z.^2);
      if r_p==0, theta_p=0;
      else theta_p=acos(z/r_p);
      end
      if x==0, phi_p=pi/2;
      else phi_p=atan(y/x);
      end
Ez1(loopx,loopy,loopz)=compute_Nz_bessel_single_point(r_p,theta_p,phi_p,thetamin,theta
max);
Ex1(loopx,loopy,loopz)=compute_Nx_bessel_single_point(r_p,theta_p,phi_p,thetamin,theta
max);
Ey1(loopx,loopy,loopz)=compute_Ny_bessel_single_point(r_p,theta_p,phi_p,thetamin,theta
max);
   end
end
end
function [value]=compute_Nx_bessel_single_point(r_p,theta_p,phi_p,thetamin,thetamax)
focal_field_glass_data
l_0=exp(-1i*k_objective*f);
K=k_objective.*f.*l_0/2;
```

```
I_0=quadgk(@(theta)compute_Ex_bessel_single_pointI_0(theta,r_p,theta_p,phi_p),thetamin,
thetamax,'Waypoints',theta_critical_angle_objective,'MaxIntervalCount',100000);
I_2=quadgk(@(theta)compute_Ex_bessel_single_pointI_2(theta,r_p,theta_p,phi_p),thetamin,
thetamax,'Waypoints',theta_critical_angle_objective,'MaxIntervalCount',100000);
E_Nx=1i.*K.*I_0;
value=E_Nx;
function [value]=compute_Ny_bessel_single_point(r_p,theta_p,phi_p,thetamin,thetamax)
focal_field_glass_data
l_0=exp(-1i*k_objective*f);
K=k_objective.*f.*l_0/2;
I_2=quadgk(@(theta)compute_Ex_bessel_single_pointI_2(theta,r_p,theta_p,phi_p),thetamin,
thetamax,'MaxIntervalCount',100000);
E_Ny=-2.*1i.*K.*I_2.*sin(2*phi_p);
value=E_Ny;
function [value]=compute_Nz_bessel_single_point(r_p,theta_p,phi_p,thetamin,thetamax)
focal_field_glass_data
l_0=exp(-1i*k_objective*f);
K=k_objective.*f.*l_0/2;
I_1=quadgk(@(theta)compute_Ex_bessel_single_pointI_1(theta,r_p,theta_p,phi_p),thetamin,
thetamax,'MaxIntervalCount',100000);
E_Nz=-2.*K.*I_1.*cos(phi_p);
value=E_Nz;
```

```
function [Value]=compute_Ex_bessel_single_pointI_0(theta,r_p,theta_p,phi_p)
focal_field_glass_data
kz_objective=k_objective.*cos(theta);
kz_air = k_air.*sqrt(1-((k_objective./k_air).^2.*sin(theta).^2));
costheta2=sqrt(1-((k_objective./k_air).^2.*sin(theta).^2));
t_s = 2.*n_objective.*cos(theta)./(n_air.*costheta2+n_objective.*cos(theta));
t_p = 2.*n_objective.*cos(theta)./(n_air.*cos(theta)+n_objective.*costheta2);
E1=sqrt(cos(theta)).*sin(theta).*exp(1i.*(kz_objective-kz_air).*z_focus);
E2=(t_s+t_p.*costheta2);
E3=besselj(0,k_objective.*sin(theta).*r_p.*sin(theta_p));
E4=exp(1i.*k_air.*r_p.*cos(theta_p).*costheta2);
Value=E1.*E2.*E3.*E4;
function [Value]=compute_Ex_bessel_single_pointI_1(theta,r_p,theta_p,phi_p)
focal_field_glass_data
kz_objective=k_objective.*cos(theta);
kz_air = k_air.*sqrt(1-((k_objective./k_air).^2.*sin(theta).^2));
costheta2=sqrt(1-((k_objective./k_air).^2.*sin(theta).^2));
t_s = 2.*n_objective.*cos(theta)./(n_air.*costheta2+n_objective.*cos(theta));
t_p = 2.*n_objective.*cos(theta)./(n_air.*cos(theta)+n_objective.*costheta2);
E1=sqrt(cos(theta)).*sin(theta).*exp(1i.*(kz_objective-kz_air).*z_focus);
E2=t_p.*sqrt(1-costheta2.^2);
E3=besselj(1,k_objective.*sin(theta).*r_p.*sin(theta_p));
```

```
E4=exp(i.*k_air.*r_p.*cos(theta_p).*costheta2);

Value=E1.*E2.*E3.*E4;

function [Value]=compute_Ex_bessel_single_pointI_2(theta,r_p,theta_p,phi_p)

focal_field_glass_data

kz_objective=k_objective.*cos(theta);

kz_air = k_air.*sqrt(1-((k_objective./k_air).^2.*sin(theta).^2));

costheta2=sqrt(1-((k_objective./k_air).^2.*sin(theta).^2));

t_s = 2.*n_objective.*cos(theta)./(n_air.*costheta2+n_objective.*cos(theta));

t_p = 2.*n_objective.*cos(theta)./(n_air.*cos(theta)+n_objective.*costheta2);

E1=sqrt(cos(theta)).*sin(theta).*exp(1i.*(kz_objective-kz_air).*z_focus);

E1=sqrt(cos(theta)).*sin(theta).*exp(1i.*(kz_objective-kz_air).*z_focus);

E2=t_s-t_p.*costheta2;

E3=besselj(2,k_objective.*sin(theta).*r_p.*sin(theta_p));

E4=exp(1i.*k_air.*r_p.*cos(theta_p).*costheta2);

Value=E1.*E2.*E3.*E4;
```

azumothal_focus_calculation

```
clear all

focal_field_glass_data

z= 0.1e-9;

Nx=501;

Ny=501;

loopx=1;
```

```
loopy=1;
x_val = linspace(-1e-6,1e-6, Nx);
y_val = linspace(-1e-6,1e-6, Ny);
thetamin=0;
thetamax=theta_NA_objective;
for loopx=1:Nx
   x=x_val(loopx);
   for loopy=1:Ny
      y=y_val(loopy);
     r_p=sqrt(x.^2+y.^2);
     rt(loopx,loopy)=r_p;
Ephi(loopx,loopy)=compute_azumothal_Np_bessel_single_point(r_p,z,thetamin,thetamax);
    end
end
 norEphi=abs(Ephi).^2/max(max(abs(Ephi).^2));
function [value]=compute_azumothal_Np_bessel_single_point(r_p,z,thetamin,thetamax)
focal_field_glass_data
I_1=quadgk(@(theta)compute_azumothal_Ep_bessel_single_pointI_1(theta,r_p,z),thetamin,t
hetamax,'MaxIntervalCount',100000);
E_Np=I_1;
value=E_Np;
function [Value]=compute_azumothal_Ep_bessel_single_pointI_1(theta,r_p,z)
```

```
focal_field_glass_data

beta=1;

c=NA/n_objective;

Al=exp(-(beta.*sin(theta)./c).^2).*besselj(1,(2.*beta.*sin(theta)./c));

E1=sqrt(cos(theta)).*sin(theta).*exp(1i.*k.*z.*cos(theta));

E2=besselj(1,k.*r_p.*sin(theta));

Value=Al.*E1.*E2;
```

radial_focus_calculation

```
clear all

focal_field_glass_data

z= 0;

Nx=501;

Ny=501;

loopx=1;

loopy=1;

x_val = linspace(-1e-6,1e-6, Nx);

y_val = linspace(-1e-6,1e-6, Ny);

p_val= linspace(0,1e-6, Ny);

thetamin=0;

thetamax=theta_NA_objective;
```

```
for loopx=1:Nx
   x=x_val(loopx);
   for loopy=1:Ny
      y=y_val(loopy);
     r_p=sqrt(x.^2+y.^2);
     rt(loopx,loopy)=r_p;
     Ep(loopx,loopy)=compute_radial_Np_bessel_single_point(r_p,z,thetamin,thetamax);
     Ez(loopx,loopy)=compute_radial_Nz_bessel_single_point(r_p,z,thetamin,thetamax);
    end
 end
  norEp=abs(Ep).^2/max(max(abs(Ep).^2));
  norEz=abs(Ez).^2/max(max(abs(Ez).^2));
function [value]=compute_radial_Nz_bessel_single_point(r_p,z,thetamin,thetamax)
focal_field_glass_data
I_1=quadgk(@(theta)compute_radial_Ex_bessel_single_pointI_1(theta,r_p,z),thetamin,theta
max,'MaxIntervalCount',100000);
E_Nz=2.*i.*I_1;
value=E_Nz;
function [Value]=compute_radial_Ex_bessel_single_pointI_1(theta,r_p,z)
focal_field_glass_data
beta=1;
c=NA/n_objective;
```

```
Al=exp(-(beta.*sin(theta)./c).^2).*besselj(1,(2.*beta.*sin(theta)./c));
E1=sqrt(cos(theta)).*(sin(theta).^2).*exp(1i.*k.*z.*cos(theta));
E2=besselj(0,k.*r_p.*sin(theta));
Value=Al.*E1.*E2;
function [value]=compute_radial_Np_bessel_single_point(r_p,z,thetamin,thetamax)
focal_field_glass_data
I_1=quadgk(@(theta)compute_radial_Ep_bessel_single_pointI_1(theta,r_p,z),thetamin,theta
max,'MaxIntervalCount',100000);
E_Np=I_1;
value=E_Np;
function [Value]=compute_radial_Ep_bessel_single_pointI_1(theta,r_p,z)
focal_field_glass_data
beta=1;
c=NA/n_objective;
Al=exp(-(beta.*sin(theta)./c).^2).*besselj(1,(2.*beta.*sin(theta)./c));
E1=sqrt(cos(theta)).*sin(2.*theta).*exp(1i.*k.*z.*cos(theta));
E2=besselj(1,k.*r_p.*sin(theta));
Value=Al.*E1.*E2;
```

Reference

1. Betzig, E. *et al.* Imaging Intracellular Fluorescent Proteins at Nanometer Resolution. *Science* **313,** 1642–1645 (2006).
2. Dyba, M. & Hell, S. W. Focal Spots of Size λ / 23 Open Up Far-Field Florescence Microscopy at 33 nm Axial Resolution. *Phys. Rev. Lett.* **88,** (2002).
3. Martin, Y., Williams, C. C. & Wickramasinghe, H. K. Atomic force microscope–force mapping and profiling on a sub 100-Å scale. *J. Appl. Phys.* **61,** 4723–4729 (1987).
4. Gross, L. *et al.* Bond-order discrimination by atomic force microscopy. *Science* **337,** 1326–1329 (2012).
5. Martin, Y. & Wickramasinghe, H. Magnetic Imaging by Force Microscopy with 1000-a Resolution. *Appl. Phys. Lett.* **50,** 1455–1457 (1987).
6. Nonnenmacher, M., Oboyle, M. & Wickramasinghe, H. Kelvin Probe Force Microscopy. *Appl. Phys. Lett.* **58,** 2921–2923 (1991).
7. Novotny, L. & Hecht, B. *Principles of Nano-Optics*. (Cambridge University Press, 2006).
8. Hecht, B. *et al.* Scanning near-field optical microscopy with aperture probes: Fundamentals and applications. *J. Chem. Phys.* **112,** 7761 (2000).
9. Schnell, M. *et al.* Controlling the near-field oscillations of loaded plasmonic nanoantennas. *Nat. Photonics* **3,** 287–291 (2009).
10. Veerman, J. A., Garcia-Parajo, M. F., Kuipers, L. & Van Hulst, N. F. Single molecule mapping of the optical field distribution of probes for near-field microscopy. *J. Microsc.* **194,** 477–482 (1999).

11. Bauer, T., Orlov, S., Peschel, U., Banzer, P. & Leuchs, G. Nanointerferometric amplitude and phase reconstruction of tightly focused vector beams. *Nat. Photonics* **8,** 23–27 (2014).

12. Fleischer, M. *et al.* Three-dimensional optical antennas: Nanocones in an apertureless scanning near-field microscope. *Appl. Phys. Lett.* **93,** 111114 (2008).

13. Feber, B. le, Rotenberg, N., Beggs, D. M. & Kuipers, L. Simultaneous measurement of nanoscale electric and magnetic optical fields. *Nat. Photonics* **8,** 43–46 (2014).

14. Kihm, H. W. *et al.* Bethe-hole polarization analyser for the magnetic vector of light. *Nat. Commun.* **2,** 451 (2011).

15. Burresi, M. *et al.* Probing the Magnetic Field of Light at Optical Frequencies. *Science* **326,** 550–553 (2009).

16. Esslinger, M. & Vogelgesang, R. Reciprocity Theory of Apertureless Scanning Near-Field Optical Microscopy with Point-Dipole Probes. *ACS Nano* **6,** 8173–8182 (2012).

17. Hillenbrand, R. & Keilmann, F. Optical oscillation modes of plasmon particles observed in direct space by phase-contrast near-field microscopy. *Appl. Phys. B* **73,** 239–243 (2014).

18. García-Etxarri, A., Romero, I., García de Abajo, F. J., Hillenbrand, R. & Aizpurua, J. Influence of the tip in near-field imaging of nanoparticle plasmonic modes: Weak and strong coupling regimes. *Phys. Rev. B* **79,** 125439 (2009).

19. Deutsch, B., Hillenbrand, R. & Novotny, L. Visualizing the Optical Interaction Tensor of a Gold Nanoparticle Pair. *Nano Lett.* **10,** 652–656 (2010).

20. Lu, F., Jin, M. & Belkin, M. A. Tip-enhanced infrared nanospectroscopy via molecular expansion force detection. *Nat. Photonics* **8,** 307–312 (2014).

21. Dazzi, A., Prazeres, R., Glotin, F. & Ortega, J. M. Local infrared microspectroscopy with subwavelength spatial resolution with an atomic force microscope tip used as a photothermal sensor. *Opt. Lett.* **30,** 2388 (2005).

22. Rajapaksa, I., Uenal, K. & Wickramasinghe, H. K. Image force microscopy of molecular resonance: A microscope principle. *Appl. Phys. Lett.* **97,** 73121 (2010).

23. Rajapaksa, I. & Kumar Wickramasinghe, H. Raman spectroscopy and microscopy based on mechanical force detection. *Appl. Phys. Lett.* **99,** 161103-161103–3 (2011).

24. Kohlgraf-Owens, D. C., Greusard, L., Sukhov, S., Wilde, Y. D. & Dogariu, A. Multi-frequency near-field scanning optical microscopy. *Nanotechnology* **25,** 35203 (2014).

25. Kohoutek, J. *et al.* Opto-Mechanical Force Mapping of Deep Subwavelength Plasmonic Modes. *Nano Lett.* **11,** 3378–3382 (2011).

26. Jahng, J. *et al.* Ultrafast pump-probe force microscopy with nanoscale resolution. *Appl. Phys. Lett.* **106,** 83113 (2015).

27. Nowak, D. *et al.* Nanoscale chemical imaging by photoinduced force microscopy. *Sci. Adv.* **2,** e1501571 (2016).

28. Tamma, V. A., Huang, F., Nowak, D. & Wickramasinghe, H. K. Stimulated Raman spectroscopy and nanoscopy of molecules using near field photon induced forces without resonant electronic enhancement gain. *Appl. Phys. Lett.* **108,** 233107 (2016).

29. Jahng, J. *et al.* Linear and Nonlinear Optical Spectroscopy at the Nanoscale with Photoinduced Force Microscopy. *Acc. Chem. Res.* **48,** 2671–2679 (2015).

30. Jahng, J. *et al.* Visualizing surface plasmon polaritons by their gradient force. *Opt. Lett.* **40,** 5058 (2015).

31. Garcia, R. & Herruzo, E. T. The emergence of multifrequency force microscopy. *Nat. Nanotechnol.* **7,** 217–226 (2012).

32. Rabe, U., Janser, K. & Arnold, W. Vibrations of free and surface-coupled atomic force microscope cantilevers: Theory and experiment. *Rev. Sci. Instrum.* **67,** 3281–3293 (1996).

33. Novotny, L. & Hecht, B. *Principles of Nano-Optics*. (Cambridge University Press, 2012).

34. Youngworth, K. & Brown, T. Focusing of high numerical aperture cylindrical-vector beams. *Opt. Express* **7,** 77–87 (2000).

35. Fleischer, M. *et al.* Three-dimensional optical antennas: Nanocones in an apertureless scanning near-field microscope. *Appl. Phys. Lett.* **93,** 111114 (2008).

36. Bauer, T., Orlov, S., Peschel, U., Banzer, P. & Leuchs, G. Nanointerferometric amplitude and phase reconstruction of tightly focused vector beams. *Nat. Photonics* **8,** 23–27 (2013).

37. Huang, F., Ananth Tamma, V., Mardy, Z., Burdett, J. & Kumar Wickramasinghe, H. Imaging Nanoscale Electromagnetic Near-Field Distributions Using Optical Forces. *Sci. Rep.* **5,** 10610 (2015).

38. *Absorption and Scattering of Light by Small Particles*. (Wiley-VCH Verlag GmbH, 1998).

39. Novotny, L. & Hecht, B. *Principles of Nano-Optics*. (Cambridge University Press, 2006).

40. Youngworth, K. S. & Brown, T. G. Focusing of high numerical aperture cylindrical-vector beams. *Opt. Express* **7,** 77 (2000).

41. Takata, Y., Haneda, H., Mitsuhashi, T. & Wada, Y. Evaluation of thermal diffusivity for thin gold films using femtosecond laser excitation technique. *Appl. Surf. Sci.* **189,** 227–233 (2002).

42. Aspnes, D. E. Dielectric functions and optical parameters of Si, Ge, GaP, GaAs, GaSb, InP, InAs, and InSb from 1.5 to 6.0 eV. *Phys. Rev. B* **27,** 985–1009 (1983).

43. García-Etxarri, A. Influence of the tip in near-field imaging of nanoparticle plasmonic modes: Weak and strong coupling regimes. *Phys. Rev. B* **79,** (2009).

44. Veysi, M., Guclu, C. & Capolino, F. Vortex beams with strong longitudinally polarized magnetic field and their generation by using metasurfaces. *J. Opt. Soc. Am. B* **32,** 345 (2015).

45. Stalder, M. & Schadt, M. Linearly polarized light with axial symmetry generated by liquid-crystal polarization converters. *Opt. Lett.* **21,** 1948 (1996).

46. Tamma, V. A., Lee, J.-H., Wu, Q. & Park, W. Visible frequency magnetic activity in silver nanocluster metamaterial. *Appl. Opt.* **49,** A11-17 (2010).

47. Mühlig, S. *et al.* Optical properties of a fabricated self-assembled bottom-up bulk metamaterial. *Opt. Express* **19,** 9607–9616 (2011).

48. Guclu, C., Tamma, V. A., Wickramasinghe, H. K. & Capolino, F. Photoinduced magnetic force between nanostructures. *Phys. Rev. B* **92,** 235111 (2015).

49. Ashkin, A., Dziedzic, J. M., Bjorkholm, J. E. & Chu, S. Observation of a single-beam gradient force optical trap for dielectric particles. *Opt. Lett.* **11,** 288 (1986).

50. Ashkin, A. & Dziedzic, J. M. Optical trapping and manipulation of viruses and bacteria. *Science* **235,** 1517–1520 (1987).

51. Ashkin, A. Optical trapping and manipulation of neutral particles using lasers. *Proc. Natl. Acad. Sci.* **94,** 4853–4860 (1997).

52. Felgner, H., Müller, O. & Schliwa, M. Calibration of light forces in optical tweezers. *Appl. Opt.* **34,** 977–982 (1995).

53. *Handbook of Micro/Nano Tribology, Second Edition*. (CRC Press, 1998).

54. Landherr, L. J. T., Cohen, C., Agarwal, P. & Archer, L. A. Interfacial Friction and Adhesion of Polymer Brushes. *Langmuir* **27,** 9387–9395 (2011).

55. Frisbie, C. D., Rozsnyai, L. F., Noy, A., Wrighton, M. S. & Lieber, C. M. Functional Group Imaging by Chemical Force Microscopy. *Science* **265,** 2071–2074 (1994).

56. Song, J., Wang, X., Riedo, E. & Wang, Z. L. Elastic Property of Vertically Aligned Nanowires. *Nano Lett.* **5,** 1954–1958 (2005).

57. Kageshima, M., Ogiso, H., Nakano, S., Lantz, M. A. & Tokumoto, H. Atomic Force Microscopy Cantilevers for Sensitive Lateral Force Detection. *Jpn. J. Appl. Phys.* **38,** 3958 (1999).

58. Rabe, U., Turner, J. & Arnold, W. Analysis of the high-frequency response of atomic force microscope cantilevers. *Appl. Phys. A* **66,** S277–S282

59. Rugar, D. *et al.* Magnetic force microscopy: General principles and application to longitudinal recording media. *J. Appl. Phys.* **68,** 1169 (1990).

60. Kerker, M., Wang, D.-S. & Chew, H. Surface enhanced Raman scattering (SERS) by molecules adsorbed at spherical particles. *Appl. Opt.* **19,** 3373 (1980).

61. Ren, B., Picardi, G. & Pettinger, B. Preparation of gold tips suitable for tip-enhanced Raman spectroscopy and light emission by electrochemical etching. *Rev. Sci. Instrum.* **75,** 837–841 (2004).

62. Bailo, E. & Deckert, V. Tip-Enhanced Raman Spectroscopy of Single RNA Strands: Towards a Novel Direct-Sequencing Method. *Angew. Chem. Int. Ed.* **47,** 1658–1661 (2008).

63. Taguchi, A. *et al.* Controlling the plasmon resonance wavelength in metal-coated probe using refractive index modification. *Opt. Express* **17,** 6509–6518 (2009).

64. Hayazawa, N., Yano, T. & Kawata, S. Highly reproducible tip-enhanced Raman scattering using an oxidized and metallized silicon cantilever tip as a tool for everyone. *J. Raman Spectrosc.* **43,** 1177–1182 (2012).

65. Okamoto, T. & Yamaguchi, I. Photocatalytic deposition of a gold nanoparticle onto the top of a SiN cantilever tip. *J. Microsc.* **202,** 100–103 (2001).

66. Kalkbrenner, T., Ramstein, M., Mlynek, J. & Sandoghdar, V. A single gold particle as a probe for apertureless scanning near-field optical microscopy. *J. Microsc.* **202,** 72–76 (2001).

67. Leiterer, C. *et al.* Dielectrophoretic positioning of single nanoparticles on atomic force microscope tips for tip-enhanced Raman spectroscopy. *ELECTROPHORESIS* **36,** 1142–1148 (2015).

68. Vakarelski, I. U. & Higashitani, K. Single-Nanoparticle-Terminated Tips for Scanning Probe Microscopy. *Langmuir* **22,** 2931–2934 (2006).

69. Jang, S.-Y., Reddy, P., Majumdar, A. & Segalman, R. A. Interpretation of Stochastic Events in Single Molecule Conductance Measurements. *Nano Lett.* **6,** 2362–2367 (2006).

70. Betzig, E. Single molecules observed by near-field scanning optical microscopy. *Science* **262,** 1422–1425 (1993).

71. Anger, P., Bharadwaj, P. & Novotny, L. Enhancement and Quenching of Single-Molecule Fluorescence. *Phys. Rev. Lett.* **96,** 113002 (2006).

72. Hall, D. B., Underhill, P. & Torkelson, J. M. Spin coating of thin and ultrathin polymer films. *Polym. Eng. Sci.* **38,** 2039–2045 (1998).